JAERI-Research
2000-015

JP0050356

STUDY ON IMPURITY RADIATION AND TRANSPORT OF JT-60U PLASMAS

March 2000

Tatsuo ISHIJIMA

日本原子力研究所
Japan Atomic Energy Research Institute

本レポートは、日本原子力研究所が不定期に公刊している研究報告書です。

入手の問合わせは、日本原子力研究所研究情報部研究情報課（〒319-1195　茨城県那珂郡東海村）あて、お申し越し下さい。なお、このほかに財団法人原子力弘済会資料センター（〒319-1195　茨城県那珂郡東海村日本原子力研究所内）で複写による実費頒布を行っております。

This report is issued irregularly.

Inquiries about availability of the reports should be addressed to Research Information Division, Department of Intellectual Resources, Japan Atomic Energy Research Institute, Tokai-mura, Naka-gun, Ibaraki-ken 〒319-1195, Japan.

© Japan Atomic Energy Research Institute, 2000

編集兼発行　日本原子力研究所

Study on Impurity Radiation and Transport of JT-60U Plasmas

Tatsuo ISHIJIMA※

Department of Fusion Plasma Research
Naka Fusion Research Establishment
Japan Atomic Energy Research Institute
Naka-machi, Naka-gun, Ibaraki-ken

(Received February 3,2000)

This thesis describes an investigation on impurity transport in the JT-60U tokamak plasma both in the core and the divertor plasmas to provide a better understanding of plasma physics. This work has been performed under the collaborative graduate school between University of Tsukuba and Naka Fusion Research Establishment of Japan Atomic Energy Research Institute.

A radiative divertor experiment with neon gas puff was carried out with an aim of investigating impurity behaviors in the divertor, after the open divertor was modified to the pumped W-shaped divertor. To evaluate neon radiation, analysis was made for lines from neon ions measured with a VUV spectrometer in the divertor plasma. As a result, lines from Ne IV-Ne VIII were identified. By combining the measurement with an absolutely calibrated multi-channel interference filter spectrometer and that with the VUV spectrometer, the radiation loss through neon line emission was estimated in the divertor plasma. In the case of pumping off, the detached plasma evolved into a MARFE. It was observed that the line intensities of highly ionized neon (Ne VII, Ne VIII) increased simultaneously with the formation of the MARFE and furthermore increased after the MARFE formation. It is considered that after the divertor plasma was detached, the plasma flow velocity and the friction force were weaker in the case of pumping off than in the case of pumping on and more impurities moved toward the X-point region. This observation implies reduction of impurity back flow from the divertor to the upstream by

---

※ Collaborative Graduate School (University of Tsukuba)

the friction force. This thesis indicates that the plasma flow in the SOL (Scrape-Off Layer) is important to confine the impurity in the divertor region and prevent the MARFE for the first time.

In reversed shear discharges with ITB (internal transport barrier), electron density, temperature and radiation power strongly increased inside the ITB. The core radiation was analyzed by bolometry, VUV spectrometer and CXRS (charge exchange recombination spectroscopy). The core radiation was evaluated with the spectroscopic method in the reversed shear regime. 97% of the main plasma radiation was bremsstrahlung and this estimation agreed with the bolometric measurement within 10%. During high performance discharges with reversed shear, the radiation profile strongly peaked inside the ITB radius. The increment of carbon density is explained by neoclassical transport of banana-banana collision regime. However, n_c/n_e is flat inside ITB during the electron density increase implying that the discharge has not reached a steady state. If the impurity keeps accumulating at the center as predicted by neoclassical transport theory, the carbon accumulation may pose a problem to the core plasma performance.

Keywords: JT-60U Tokamak, Divertor, Detachment, MARFE, Radiation, Impurity Behavior, Thermal Force, Friction Force, Neo-classical Transport, Particle Flux

JT-60Uプラズマにおける不純物放射及び輸送に関する研究

日本原子力研究所那珂研究所炉心プラズマ研究部
石島達夫※

（２０００年２月３日受理）

本論文はJT-60Uトカマクでの主プラズマ、ダイバータプラズマにおける不純物の輸送及びその放射損失についての研究を記したものであり、プラズマ物理のより深い理解を与えるものである。本研究は、筑波大学と日本原子力研究所間の連携大学院制度に基づき、日本原子力研究所・那珂研究所で行われた。

開ダイバータから排気付きW型ダイバータへ改造がなされた後、ネオンガス注入による放射ダイバータ実験をダイバータにおける不純物輸送を調べる目的で行った。ネオン放射損失を評価するためにダイバータプラズマにおいて真空紫外分光器でネオンイオンからのスペクトル線を解析した。その結果ネオンの三価－七価のイオンを同定した。絶対感度較正を行っている多チャンネル干渉フィルター分光と、真空紫外分光を組み合わせることで、ダイバータプラズマにおけるネオンラインスペクトルからの放射損失量を見積もった。排気無しの場合には、ディタッチプラズマはMARFEへと発展した。高価数のネオン（六価、七価）発光強度がMARFE発生に伴い増加し、MARFE発生後にさらに増加した。このことは、ダイバータプラズマがディタッチした後、プラズマ流速及び摩擦力が、排気無しの場合では排気有りの場合に比べて弱くなり、より多くの不純物がX点領域に向かって移動していることによるものと考えられる。この観測は、ダイバータから上流にかけての摩擦力による不純物の逆流の減少を示唆している。本論文では、境界プラズマ層（スクレイプ・オフ層）におけるプラズマ流の存在がダイバータ領域における不純物を閉じ込め、MARFEを回避する上で重要であることを初めて明らかにした。

内部輸送障壁を伴う負磁気シア放電では、電子密度、電子温度、放射損失が内部輸送障壁内側で急激に増大する。主プラズマでの放射損失はボロメータ、真空紫外分光器、荷電交換再結合分光によって解析した。負磁気シア放電における主プラズマでの放射損失を分光学的な手法を用いて見積もった。内部輸送障壁内部における放射損失の９７％は制動放射であり、放射損失パワーは、ボ

那珂研究所：〒311-0193　茨城県那珂郡那珂町向山801-1
※　連携大学院生（筑波大学）

ロメータによる計測値と１０％以内の誤差で一致した。負磁気シア高性能放電の間、内部輸送障壁の内側で放射損失の分布は強くピークする。炭素密度の増大量はバナナーバナナ衝突での新古典拡散で説明される。しかし炭素密度／電子密度で表される比は、内部輸送障壁の内側で電子密度が上昇し続ける間、一定であり、このことは、放電が定常状態に到達していないことを示唆している。もし新古典拡散で予測されるように中心で不純物が蓄積するならば、炭素の蓄積は主プラズマの性能にとって問題となる可能性がある。

CONTENTS

目次

1. Introduction

Nuclear fusion is considered as one of alternative future new energy resources. The most likely reaction to be used in a fusion power plant involves two isotopes of hydrogen, deuterium and tritium. Deuterium can be found in ordinary water while tritium cannot be found in nature. Tritium may however be produced from lithium in conjunction with the fusion process. The fuel would thus be seawater and lithium with a supply that would last for millions of years.

The hot plasma for nuclear fusion must be contained and prevented from contact with any solid surfaces. An approach to this problem is to control the plasma using a magnetic field. Different concepts exist for the realization of the magnetic container (ex. tandem mirror, helical device). In particular, performance improvement in every aspect has been achieved in tokamak devices[1]. The break-even plasma condition has been achieved in JET in DT operation (Joint European Tokamak at the Culham Laboratories in the UK)[2] and equivalent break-down has been achieved JT-60U (Japan Tokamak at Naka Fusion Research Establishment of JAERI) in DD operation[3]. The deuterium-tritium mixture discharges have been performed in TFTR (Tokamak Fusion Test Reactor at the Princeton Plasma Physics Laboratory in United States)[4] and JET[5]. As the next step to achieve ignition in tokamak fusion research, International Thermonuclear Experimental Reactor(ITER) project is being designed under international collaboration.

It is essential for the nuclear fusion reactor to keep good core confinement. To achieve good confinement, the impurity levels in the plasma should be as low as possible. Therefore it is necessary to understand the impurity behavior in the whole plasma region. This thesis describes a study on impurity behavior in the core and divertor plasma.

In the divertor region impurity plays an important role. It is necessary to reduce the divertor plate heat flux by enhancing the impurity radiation, since the power from the core concentrates at the divertor plate. Radiative cooling and formation of dense and cold divertor require full utilization of atomic processes and plasma dynamics including impurities.

As the divertor plasma scenario the partial detached divertor is a promising scheme. Nevertheless there are few studies about the impurity behavior on the condition of detached divertor and MARFE. The MARFE occurs in a condition close to that of detached divertor. This thesis indicates that the plasma flow in the SOL (Scrape-Off Layer) is important to confine the impurity in the divertor region to prevent the MARFE for the first time.

On the other hand, impurity levels should be high in the divertor region, but low in the core plasma as much as possible to keep good confinement. Studies on impurity behavior of core plasma were performed, particularly inside ITB(Internal Transport Barrier), by the TFTR group(Tritium, Helium, Carbon)[1], H.Takenega in JT-60U(Neon, Helium, Carbon)[2] in reversed shear discharges, and the JET group(Nickel, Carbon)[3] in optimized shear plasmas. The TFTR group investigated the impurity behavior both in reversed shear and enhanced reversed shear(ERS) regime with CXRS (Charge Exchange Recombination Spectroscopy) measurement. The TFTR results show that the diffusion coefficients of these three impurities were consistent with the neoclassical transport and the carbon density was more peaked in the ERS than in the RS. The JET group studied the transport of impurity in the optimized shear plasma. It was shown that Ni was retained outside the ITB in the strong ITB case, and an additional inward pinch was required around ITB in the case of carbon. H. Takenaga investigated the particle transport about Ne and He with gas-puffing modulation experiments, and about C with the time evolution of density profile in reversed shear. The particle diffusivity was almost the same for these three ions(Ne, He, C) and the inward pinch velocity was larger for ions having higher charge state.

However, there has been no detailed bolometric or spectroscopic assessment of radiation from the core plasma in the good confinement regime. This thesis work is the first comprehensive analysis about carbon impurity transport and power balance in the core plasma including radiation, spectroscopy, bremsstrahlung, and neutron emission in reversed shear plasma close to the break-even condition both experimentally and theoretically. This thesis indicates that the carbon accumulation inside the ITB may pose a problem to the core plasma performance in a reversed shear plasma.

Following is the plan of this thesis paper. A review of physical phenomena in the tokamak device plasma, which are indispensable for understanding the study in this thesis, is provided in sections 3 and 4. The results of this thesis work are described in sections 5 and 6. The impurity behavior in the divertor region with neon gas puff is described in section 5. In section 6, a detailed analysis of the radiation from core plasma is described. Finally, a summary of the study performed in this thesis is presented in section 7.

2. Device and Diagnostics

2.1 JT-60U and Tokamak

2.1.1 Fundamental Principle

The tokamak is a toroidal plasma confinement system, the plasma being confined by a magnetic field[1]. The word 'tokamak' is derived from the Russian word acronym for "toroidalnaya kamera ee magnitnaya katushka". The geometry and coordinate system are shown in figure 2-1 and an example tokamak of a machine is shown in figure 2-2. The tokamak consists of toroidal vacuum vessel and several magnetic coils. The toroidal magnetic field B_ϕ is produced by the toroidal coils. The poloidal magnetic field B_θ is produced by a plasma current Ip which is driven by a toroidal electric field E_ϕ induced by transformer action with the plasma acting as a single turn secondary.

The major radius R_0 is the distance from the toroidal axis. The two minor radii a and b are the horizontal and vertical distances from the magnetic axis to the edge of the plasma. The ratio R_0/a, characterizing the fatness of the torus, is the toroidal aspect ratio. The ratio b/a is the elongation of the plasma cross section.

There are advantages for confinement and achievable pressure with plasmas which are vertically elongated. The plasma shape, elongation, and the position of the plasma is controlled by the additional poloidal field coils. The spatial variation of the toroidal magnetic field strength is approximately given by:

$$B_\phi = \frac{B_0 R_0}{R} \qquad (2.1),$$

where B_0 is the magnetic field strength at the center of the plasma. In a uniform magnetic field, the changed particle has a helical orbit composed of the circular motion and a const velocity in the direction of the magnetic field. The cicular orbit has a radius ρ_r defined as

$$\rho_r = \frac{mv_\perp}{Z|e|B} \qquad (2.2),$$

where m is the mass, e is the electric charge, $v_\perp$ is the perpendicular velocity to the magnetic field, Z is the charge number.

The principal for plasma confinement is to use the strong toroidal field and confine the charged particle along the magnetic field line. However, this toroidal field is not sufficient to confine a plasma. When there is the gradient of magnetic field, the ρ_r has a different curvature on the part of its orbit in plasma. This leads to a drift perpendicular to both the magnetic field and its gradient. This drift is called a ∇B drift. Moreover, when a particle's guiding center follows a curved magnetic field line, it undergoes a drift perpendicular to the plane in which the curvature lies. This drift is called curvature drift. In the case there is the toroidal field alone, curvature drift is in the same direction as the ∇B drift. A velocity caused by both the ∇B drift and the curvature drift is given by:

$$v_{dr} = -\frac{m}{qB_0R_0}\left(v_{//}^2 + \frac{v_\perp^2}{2}\right)e_z \qquad (2.3),$$

where $v_{//}$ is the parallel velocity along the magnetic field line and e_z is the unit vector in the direction of the vertical axis. The ion moves toward the upper side of the torus and electron moves the lower side if the field B is counter clockwise as seen from the top. This leads to a charge separation and makes electric field, E. The $E \times B/B^2$ drift by the charge separation throws out the plasma outward of the major radius. When there is a plasma current in toroidal direction, magnetic field line makes a nested tori and the separated charges are shorted. Therefore, the tokamak requires the toroidal plasma currents. When there is the plasma current in toroidal direction, the force which expands the plasma current works the plasma. This is because the inside magnitude of the magnetic-flux density is larger than outside one. This outward force is called hoop force. This force is balanced by applying a vertical magnetic field which interacts with the toroidal current to give an inward force. The position control coil which causes a vertical magnetic field is installed to cancel the hoop force(Fig. 2-2).

The pitch of the helical field line in the tokamak may be characterized by the safety factor q_s. For a large aspect ratio plasma with a circular cross-section, the safety factor is written as

$$q_s(r) = \frac{r}{R_0} \frac{B_\phi}{B_\theta(r)} \qquad (2.4)$$

where r is the minor radius of the flux surface. The safety factor presents the number of complete toroidal turns of a field line before completing a single poloidal turn. It is a very important factor in determining overall stability of the plasma. Consider the equilibrium configuration around a surface, having $q_s = m/n$ where m and n is the poloidal and toroidal mode numbers. The magnetic field lines on this surface define a helix. At these surfaces the magnetic field lines break and reconnect to form magnetic islands. A perturbation resonant with this surface has the form $\exp i(m\theta - n\phi)$. In the case of a low-q_s discharge, these instabilities frequently lead to a disruption. Consequently, the q_s profile emerges as a critical factor in determining the overall stability of tokamak plasmas. Other important factors in magneto-hydrodynamic (MHD) stability include the ratio of plasma pressure to magnetic field pressure, β.

2.1.2 JT-60U Tokamak Configuration

Most present tokamaks have the divertor configuration, which is beneficial to isolate the core plasma from plasma-wall interaction as illustrated in figure 2-3. The divertor configuration is available to separate the main plasma from the first wall. In the divertor configuration, plasma is simply divided into four regions; confined region, scrape-off layer(SOL) region, private region, and divertor region. The boundary between the confined and the SOL region is referred to as the last closed flux surface (LCFS) or the separatrix (which also includes the boundary between the private and the divertor).

The divertor configuration is produced by the additional divertor coil in the toroidal direction. Divertor coil current flows in the same direction as the plasma current. The poloidal magnetic field B_θ has a null at the x-point. The shape of LCFS is also controlled by the external coil. The plasma particle and heat exhausted from the confined region are conducted to the divertor target along the SOL magnetic field line. The advantage of the divertor configuration is to reduce the neutral particles and impurities generated by plasma-wall interaction entering the main plasma. However, the small area in the divertor target is compelled to receive large heat flux. In a fusion reactor, the design of the divertor will be very important to control the power reaching the target surface.

The measured data in JT-60U are obtained as a function of different coordinates for each diagnostic system because the geometrical restriction on the viewing chords differ from one port to the other. Furthermore, the geometrical shape of poloidal section in JT-60U experiment has a wide range from an expanded plasma for RF heating experiment to a small volume plasma close to inner vessel. So relative measured points from the plasma center vary if the same diagnostic system are used. To map the data in the same relative position we introduce the parameter ρ, which is the volume-averaged minor radius defined as

$$\rho = \sqrt{\frac{V}{2\pi^2 R}} \quad \text{(m)} \qquad (2.5)$$

where V is the plasma volume surrounded by the closed flux surface, R is the plasma major radius of the separatrix.

2.1.3 Plasma characteristics of JT-60U

JT-60U [9,10] is a large tokamak type experimental device which began its operation from April 1985. The original JT-60 had a closed divertor chamber situated on the large major radius side of the plasma. But this configuration and lack of deuterium operation capability did not allow a high quality H-mode operation. To permit the H-mode operation and improve the plasma performance, JT-60 was modified to JT-60U which is capable of deuterium operation and high plasma current up to 6MA with an x-point at the bottom of the vacuum vessel between November 1988 and May 1991.

Most of the present tokamak-type devices, the plasma have divertor configuration, in which heat flux hits the first wall in a narrow region. In future tokamak fusion devices like ITER[11], the divertor has to intercept enormous heat flux, around 20-30 $MW \cdot m^{-2}$ at the peak, which is very high compared with an acceptable value for materials. Thus, an operation scenario is required for ITER to enable heat reduction by impurity radiation in the divertor and particle reduction by detachment from the target. The divertor of JT-60U was modified from an open divertor to a W-shaped divertor with pumps from February to May 1997 [12], to investigate the effects of the divertor geometry to contribute to the design of ITER.

An overall schematic view of the JT-60U is shown in figure 2-4. JT-60U has 18 toroidal field coils. The operational parameters of JT-60U before and after the W-shaped divertor modification are summarized in Table 2-a. The poloidal cross-sections before and after the W-shaped divertor modification are shown in figure 2-5(a) and (b). JT-60U is capable of hydrogen, deuterium, and helium gas operation. The first wall is completely lined with graphite, especially in the divertor target lined with carbon fiber composite (CFC) tiles. Therefore, the dominant impurity in the plasma is carbon.

2.1.4 progress in JT-60U

JT-60U has achieved high-performance plasmas in various operational modes such as H-mode, high-β_p H-mode, reversed shear(RS) mode and so forth, and contributed in many aspects of ITER physics R&D. Reversed shear operation is characterized by a region where the magnetic shear, s=(r/q)dq/dr, is negative in the core region. In 1998, high fusion performance has been obtained in low q_s, high I_p reversed shear discharges with Internal Transport Barrier(ITB) on JT-60U. ITB works as electron and ion thermal barrier and makes gradient of temperature and density very steep. Figure 2-6 shows a time evolution of ion temperature, ITB region and pressure profile in JT-60U. The ITB observed in JT-60U has an outstanding feature that electron and ion thermal diffusivities are simultaneously reduced with a steep temperature gradient around a thin ITB layer[13]. The record value of equivalent fusion multiplication factor, $Q_{DT}^{eq}=1.25$, has been achieved in a deuterium discharge with $B_t=4.4$ T, $I_p=2.6$ MA and $q_{95}=3.2$ in JT-60U. The neutron emission rate was 3.6×10^{16} s^{-1} with neutral beam power of 12 MW [14]. These fusion performance are shown in Lawson diagram(Fig.2-7).

The divertor modification has enabled the sustainment of good confinement for 9 s with high power neutral beam heating (20-25 MW) without any increase of impurity and particle recycling. The total energy input reached 203 MJ. The D-T equivalent fusion gain Q_{DT}^{eq} ~0.1 was sustained for 9 s and Q_{DT}^{eq} ~0.16 for 4.5 s in high-β_p ELMy H-mode discharges (ELM: Edge Localized Mode [1]), in which H-factor(= $\tau_E/\tau_E^{\mathrm{ITER89PL}}$)~2.2, β_N~1.9 and β_p ~1.6 were sustained with 60-70% of non-inductive driven current[15].

The remarkable progress in the reversed shear operation was demonstrated by its long time sustainment with ELMy H-mode edge. By using power step-down technique, the β-collapses were avoided and a favorable performance with H-factor=1.8-2.5 and β_N=1.5-1.8 was sustained for 1.5 s[16].

2.1.5 Additional Heating System

The ohmic heating is induced by the resistance to the toroidal current caused by electron-ion collisions. The plasma is heated up to temperature of a few keV. The ohmic heating power degrades as the temperature increase with a $T_e^{-3/2}$ dependence of the plasma resisitivity. To achieve > 10 keV, additional heating such as neutral beam injection and radio-frequency heating are used. In the former, to penetrate through the tokamak's magnetic field, high energy neutral atoms are injected into the plasma. In the latter, high power electromagnetic waves are injected into the plasma and heat the plasma by resonant interactions.

2.1.5(1) Neutral Beam System

The neutral beam injection(NBI) of JT-60U is composed of two systems, one is a positive-ion based NBI and the other is a negative-ion based NBI. The NBI for the JT-60 started its operation in 1986 with hydrogen beam. All the original neutral beam lines were perpendicular injection. In 1990-1991 four beamlines out of 14 were modified from perpendicular to tangential injection. At the same time, modification was made to enable deuterium beam operation.

The heating power of positive-ion based NBI system is up to 40MW at 90 keV with deuterium. The duration of beam injection is up to 10 s.

The negative-ion based NBI system (N-NBI), which is aiming at 10 MW at 500 keV, is composed of one beam-line with two ion sources and a set of high voltage power supply. N-NBI system can also be used for driving current.

2.1.5(2) Radio-Frequency Heating System

In radio-frequency heating, high power electromagnetic waves are injected into the plasma and heat the plasma by resonant interactions. Two main schemes are currently exploited in JT-60U: one is ion cyclotron resonance heating (ICRH in which the frequency is chosen to resonate at the cyclotron frequency or its harmonics, 110-130 MHz, $2\,\Omega_{CH} = 116$ MHz at Bt=3.8T) and the other is lower-hybrid heating (LHRF at 1.74-2.23 GHz). Lower-hybrid waves undergo Landau damping by electrons or ions. The design pulse length of these systems is 10s, the heating capability is 6 MW of ICRF and 7 MW of LHCD. Radio-frequency heating has the advantage of flexible control of the heating profile, since the cyclotron absorption occurs locally. Radio-frequency waves can be also used for driving current.

Electron Cyclotron Heating(ECH) systems were installed in 1999. The specifications are: The frequency is 110GHz, the maximum input power of 1MW and its maximum duration time is 5sec. The absorption width of the wave is 0.1 m.

2.1.6 Divertor of JT-60U

To investigate the effect of divertor geometry and pumping on the divertor performance in JT-60U, the previous open divertor was modified to a W-shaped divertor with pumps[17]. This W-shaped divertor follows the design adopted by ITER.

The W-shaped divertor is characterized by the inclined divertor plates, the dome, and the baffle plates as shown in figure 2-5(b). The inner and outer divertor plates are inclined at angles of 70 and 60 degrees in order to increase the neutral density at the strike point. The domes cover the private region, separating the inner and outer divertors in order to improve the pumping efficiency from the inner private region and to impede free upstream motion of gas. The inclined divertor and the private dome are effective to condense neutral particles near the separatrix hit points and minimize leakage of neutral particles from the divertor to the main plasma.

As a pumping scheme of W-shaped divertor, inner leg pumping (pumping from the inner divertor) was adopted for the first stage experiment. This scheme has never been implemented in other tokamaks. The pumping aperture of 3 cm in width is arranged between the inner divertor plates and the inner wing of the dome continuously in the toroidal direction. Three pumping ports are connected to the duct under the baffle. Three cryo-pumps with a pumping speed of 1000 $m^3 \cdot s^{-1}$ each are used for divertor pumping. The measured net pumping speed at the pumping slot is 13 $m^3 \cdot s^{-1}$ in the molecular flow regime. The pumping probability is about 0.6-2 % for the particle flux to the divertor in discharges with ion ∇B drift toward the x-point. Gas fueling valves are installed at the top of the vacuum vessel for main gas puff (three ports) and in the divertor region for divertor gas puff (two ports). This W-shaped divertor provides an important database for designing a next step tokamak like ITER.

2.2 Diagnostics in JT-60U

In order to understand the physical processes in the plasma, the JT-60U tokamak is equipped with diagnostic systems which are available for comprehensive survey. These measurements can be used to determine the general plasma parameters, assess the fusion performance and study specific plasma phenomena. The parameters most commonly monitored are the plasma energy, neutron emission rate, power input and output, temperature and density profiles of electrons and ions, magnetic field configuration and current profile, radiation, impurity emission intensity, divertor and edge plasma parameters. Diagnostic tools equipped in JT-60U are summarized in table 2-b.

2.2.1 Measurements of impurities

2.2.1.1 Bolometer

A measurement of the total radiation emitted from the plasma is important for the evaluation of the energy balance. Generally, these measurements have been made with a wide variety of different sensors including thermistors, thermopiles, pyroelectric detectors, and thin film bolometers. The sensors are often arranged in pinhole camera configurations so that the whole plasma cross-section is covered. As the observed signals are integrals over a line-of-sight, the total radiated power from the plasma may be obtained by integrating over the viewing angle of a single camera.

In JT-60U the radiation loss power is measured with a 32-channel bolometer array, viewing from two top diagnostic ports, one midplane port and two side ports(Fig.2-8). The bolometer consists of a polyimid film plated with a gold film. From 1995 to improve spatial resolution of the divertor measurement, additional bolometer sensors with a smaller size, are arranged. Its spatial resolution is increased by a factor of

2, or radial resolution from about 6cm to 3cm typically at divertor tiles. The divertor radiation loss is calculated by the residual after subtracting the contribution of the main radiation loss from the total radiation loss, assuming up-down symmetry of the main plasma radiation. Two midplane arrays with 16 chords are arranged to measure the upper and lower half of the main plasma and the divertor. These midplane arrays are tilted about 10 degrees in toroidal direction to reduce the effects of charge exchange neutrals, caused by orbit excursion of ripple trapped ions [18].

The divertor was modified from an open configuration to a W shape with a dome and baffle plates to shield neutral particles back flow in 1997. More closed structure of the divertor chamber has made access from diagnostic ports impossible. However, observation from many different view angles is significantly important to understand divertor radiation with temporal-spatial variation. Four channels of PTS bolometer[19-22] were installed inside the divertor chamber. Details of viewing chords for PTS bolometer are shown in Fig.2-9. View of a PTS bolometer head is shown in Fig.2-10. Two heads contain 4 detectors each, measuring the profiles along the inner and outer divertor channels, respectively. The central head is looking upward aiming at the separatrix cross x-point above the dome top. The entrance slit of the camera is located 4cm behind a graphite tile surface and each channel is separated by plates to avoid cross talk. Another head is installed to monitor x-point region horizontally.

2.2.1.2 VUV spectrometer (Main Plasma)

The VUV spectrometer for the main plasma covers a wavelength range of 0.5 nm - 40 nm with a wavelength resolution of $\lambda/\Delta\lambda > 50$ (at 5 nm) , and its time resolution 20 ms [23]. Viewing chord of VUV spectrometer(Main Plasma) is shown in Fig. 2-11.

2.2.1.3 VUV spectrometer (Divertor Plasma)

The VUV spectrometer for the divertor plasma covers a wavelength range of 25 nm - 130 nm with a wavelength resolution of $\lambda / \Delta \lambda >$ 400 (at 100 nm), and a time resolution of 20 ms [24]. The divertor VUV spectrometer measures a part of sightlines of 60-channel interference filter spectrometer(from 16ch to 28ch) in the divertor region through the main plasma. Viewing chord of VUV spectrometer(Divertor Plasma) is shown in Fig. 2-11.

2.2.1.4 Normal incidence VUV spectrometer (Divertor Plasma)

A normal incidence VUV spectrometer is installed with its viewing chord across the inboard divertor channel. The normal incidence VUV spectrometer covers the wavelength range of 100-235 nm, its time resolution is 20 ms/spectrum, the reciprocal line dispersion is 4.54 nm/mm at 610 nm and the spatial resolution about 10 mm(one chord)[25]. This spectrometer measures the 4th order for CIV 155.08 nm at 620 nm ($2s^2S$-$2p^2P^0$) . Viewing chord of Normal incidence VUV spectrometer is shown in Fig. 2-12.

2.2.1.5 CXRS(Charge Exchange Recombination Spectroscopy)

The basic technique consists of measuring spectral profiles and shifts of emission lines which are excited by charge exchange recombination reactions. The first walls of JT-60U are covered with carbon tiles. Therefore, the dominant impurity is carbon. The fully ionized carbon ion and fast neutral atoms (typically H^0 or D^0) from either a diagnostic neutral beam or a heating neutral beam are used. The recombination process

$$H^0 + C^{6+} \rightarrow H^+ + C^{5+*} \qquad (2.6)$$

leaves the resulting ion in an excited sate which subsequently decays through photon emission. Due to the charge transfer between neutral atom from the neutral beam and fully stripped carbon ion, light (529.2 nm at n=8-7 transition) is emitted from the volume along the neutral beam.

The measured spectral profiles and shifts of emission lines from carbon ions are used to evaluate the ion temperature, toroidal and poloidal rotation velocity and the absolute carbon density. The determination of the density of a fully stripped impurity via CXRS requires knowledge of the total excitation rate for the line measured[26-28]. When a spectrometer sightline crosses a neutral beam, the intensity for a transition at wave length λ due to prompt charge exchange recombination events is given by

$$B_\lambda^{cx} = \frac{1}{4\pi}\sum_{j=1}^{M} < \sigma v >_j^\lambda \int N_z N_j dl \qquad (2.7)$$

where $< \sigma v >_j^\lambda$ is the rate coefficient for excitation of wave length λ by the *j*th beam velocity component, N_z is the impurity ion density, and N_j is the beam particle component at velocity $v_j = v_1 / \sqrt{j}$. The beam particle column densities are readily calculated via a beam attenuation code by using the stopping cross sections, given specific plasma density, temperature and Z_{eff}[29].

The observation points are located along a beam-line of one of the upper perpendicular neutral beams. The observation points of CXRS are shown in Fig. 2-13. Its spatial resolution is 5 cm poloidally and its time resolution is 16.7 ms[30].

2.2.1.6 Bremsstrahlung

For determination of Z_{eff}, we measure intensities of visible bremsstrahlung tangentially (Fig. 2-13). The spatial resolution is 20 cm, the measured wavelength is 523.1±0.5 (nm), and the time resolution is 100 ms [31]. Bremsstrahlung radiation is emitted in the visible region due to electron-ion collisions. Its intensity at wavelength λ ($\gg hc/T_e$) is given by

$$\frac{dN}{d\lambda}=3\times10^{-21}\frac{\bar{g}n_e^2Z_{eff}}{\lambda\sqrt{T_e}} \quad m^{-3}s^{-1}nm^{-1} \qquad (T_e \text{ in keV}) \ (2.8)$$

where $\bar{g}$ is the temperature averaged Gaunt factor and λ is in nm. Line of sight integrals of this intensity must be measured over the full plasma cross-section for a determination of the Z_{eff} profile. The contribution of the bremsstrahlung emission from the SOL mantle plasma is excluded using a channel viewing outer separatrix region. In addition, the plasma temperature and line of sight integrals of density must be known.

2.2.1.7 60-channel visible spectrometer by interference filter

A 60-channel interference filter spectrometer[31] measures spatial intensity profiles of visible lines in the divertor region with a spatial resolution of about 1.1 cm. The light is collected by lenses and transmitted by optical fibers from the torus hall to a diagnostic room. The light from the optical fibers is split into four components that pass four interference filters. Four 512-channel image-intensified photodiode arrays observe the image of the optical fibers. The spatial profiles of four wavelengths are measured simultaneously. In this paper, D I (n=2-3,656.1nm), Ne I (640.2nm), C IV ($3s^2S$-$3p^2P$,580.1nm) and C II ($3s^2S$-$3p^2P$,657.8nm) intensities are measured. The sensitivity of the spectrometer is absolutely calibrated [32]. Its time resolution is 100 ms and its wavelength band is ~1nm.

2.2.2 Other diagnostics

2.2.2.1 Neutral Pressure Gauges (Fast response ionization gauges)

In order to investigate the divertor neutral pressure and to estimate the characteristics of divertor pumping, fast response ionization gauges are installed at the divertor structure in JT-60U (Fig. 2-12). Since the gauges are installed in the strong magnetic field, the sensitivity has to be calibrated in situ under the same magnetic field as in experiments.

Seven gauges are settled at the divertor region in order to collect the neutral flux onto the inside baffle, the inside divertors, the dome top, the outside divertor, and the outside baffle. Additionally three and one gauges are at the pumping ducts, and at the outer midplane, to collect the flux under the outer baffle, and at the surroundings of main plasma, respectively. The time response of the gauge is about 3-4ms [33].

2.2.2.2 Target Langmuir Probes

In its simplest form the Langmuir probe consists of a single electrode which can be inserted into the plasma. A voltage is applied to the probe with respect to the vessel and the current is measured. From the current-voltage (I-V) characteristic of such a probe the electron temperature T_e and density n_e can be deduced. When the probe is biased sufficiently negatively all electrons are repelled and all that remains is the ion current. This current is independent of voltage and is called the ion saturation current. Saturation of the ion current occurs because all the bias potential appears across the thin sheath and the ion flux is simply determined by the flux of ions crossing the thin sheath edge at the ion sound speed.

The single Langmuir(electrostatic) probe [34] arrays which consist of eighteen identical probes separated by about 2-3 cm poloidally, is mounted on the inboard and outboard divertor plates (Fig.2-12). From the current-voltage characteristics of the probe, the local values of ion saturation current density I_s, electron temperature T_e and floating potential V_f can be deduced directly.

2.2.2.3 Thomson scattering and ECE measurements

The electron density and the electron temperature of ruby Thomson scattering diagnostics are obtained at a few times per shot, while the electron density data of YAG Thomson scattering diagnostics are available every 100ms during the discharge period.

The electron temperature for $\rho < 0.5$ m is obtained with electron cyclotron emission(ECE) measurements, here ρ is defined as eq.(2.6). The time evolution of the electron density for $\rho < 0.5$ m is obtained with a CO_2 laser interferometer along a tangential chord[35].

3. Divertor physics

3.1 Function of divertor

In the case of a limiter plasma, the last closed flux surface(LCFS)(Fig.2-3) is defined by a solid surface and consequently neutral impurity atoms released from the surface can enter directly into the confined plasma. In the divertor configuration, however, impurities released from the target are ionized and may be swept back to the target by the plasma flow before they can reach the LCFS and enter the confined plasma.

Furthermore for fusion reactor one of the most serious concerns is that of controlling the power reaching the solid surfaces. Enormous power entering the scrape-off layer and the heat flux flows along the scrape-off parallel to the magnetic field and reaches the divertor target plate.

Third, in reactor plasmas, helium ash produced from DT fusion reactions dilutes the fuel and prevent the self-ignition from sustaining the controlled burning.

To solve these problems, the divertor has been designed for following objectives,

(I) Minimizing the impurity content of the main plasma by having the plasma surface interactions remote from the confined plasma and designing the divertor particle flow so that any impurities produced at the target cannot enter the confined plasma.

(II) Removing the alpha particle power by impurity radiation and charge exchange to reduce the divertor heat load.

(III) Removing the helium ash resulting from the fusion reactions so that the reacting fuel is not seriously diluted.

3.2 Divertor transport physics

In tokamaks it is desirable that the impurity is confined in the divertor region by the friction force. In the divertor plasma, temperature of divertor plasma decreases near the divertor plate by radiative cooling of impurities to reduce the heat flux to the divertor plate. In this situation, thermal force occurs as a result of ion-impurity and electron-impurity coulomb collision and impurity ions flow to the upstream high temperature region by thermal force. If the thermal force is larger than the friction force, impurities flow into the upstream SOL region, and pollute the core plasma. In this section we discuss how the thermal and friction force work on the impurity ions.

3.2.1 thermal force

First we consider the thermal force working between electron and ion. A simple explanation of thermal force is shown in Fig. 3-1. The horizontal axis shows the upstream direction along the magnetic field line and the vertical axis shows the electron temperature. The ion fluid element receives forces, R_{up} ,R_{down} at the upstream and downstream surface with its magnitude $m_e n_e v_e / \tau_e$, where R_{up} , R_{down} are the thermal force working to ions from upstream and downstream, respectively, and v_e is electron velocity and τ_e is electron-ion collision time. When the plasma is uniform, these forces cancel each other and no force works on the ion. If the electron distribution function is different from one side to the other, the force against ions from electrons having higher energy is smaller than the force from electrons having lower energy, since $\tau_e \propto v_e{}^3/n_e$. As a result, the thermal force on ions, F^{th}_{ion}, toward "electrons having higher energy" occurs and its magnitude is proportional to $\frac{m_e n_e^2}{T_e}$ (3.1).

Next we consider temperature gradient along the magnetic field and obtain the magnitude of thermal force.

The force working on ions is given as

$$\left|F^{th}_{ion}\right| = \left|\Delta\left(\frac{m_e n_e v_e}{\tau_e}\right)\right| = \left|\Delta T_e \cdot \frac{\partial}{\partial T_e}\left(\frac{m_e n_e v_e}{\tau_e}\right)\right| \approx \left|\Delta T_e \cdot \left(-\frac{1}{T_e}\right)\left(\frac{m_e n_e v_e}{\tau_e}\right)\right|$$

$$\cdot\ \cdot\ \cdot\ (3.2)$$

and

$$\Delta T_e \sim \lambda_e\left(\frac{\partial T_e}{\partial x}\right) \qquad (3.3)$$

where λ is the electron collision mean free path. Therefore the force working on ions acts in the direction of high temperature region and its magnitude is derived from (3.2) and (3.3)

$$(3.2)\cdot\cdot\ \approx \left|\frac{\lambda_e}{T_e}\frac{\partial T_e}{\partial x}\frac{m_e n_e v_e}{\tau_e}\right| \approx \left|n_e \frac{\partial T_e}{\partial x}\right| \qquad (3.4)$$

By substituting the electrons with ions in the above argument, we can derive the thermal force from ions to impurity ions. Substitution can be made as follows:

$$m_e \rightarrow M, \tau_{ei} \rightarrow \tau_{iI}\left(= \left(\frac{n_i}{n_z Z^2} \right) \tau_{ii} \right), \lambda = \tau_e v_e \rightarrow \tau_{iI} v_i \quad (3.5).$$

As a result of the collision between ions and impurities, a thermal force occurs, which tends to push impurities to the high temperature region. Its magnitude is given as

$$\left| F^{th}_{impurity} \right| \approx \left| n_z Z^2 \left(\frac{\partial T_i}{\partial x} \right) \right| \qquad (3.6)$$

Here, we suppose the impurity density is small compared with the ion density.

Comparing the magnitude of the thermal force of ion and electron, the electron thermal force coefficient is proportional to $0.71Z^2$, derived by Braginskii[36], and ion thermal force coefficient is proportional to $2.65Z^2$ which is an asymptotic value for heavy impurities given in Chapman[37].

In the classical plasma transport theory along the field line, the effect of parallel density gradient of other species is considered through the parallel electric force[38]. In the attached plasma, where the plasma pressure is approximately constant along the field line, the effect of density gradient itself is not significant.

When the density increases and temperature decreases, e.g. in a detached plasma (Section 3.3), the neutral-ion collision must be considered. Simply speaking, the coulomb collision frequency of ion-impurity ion is proportional to $T_i^{-3/2}$ and elastic collision frequency of ion-neutral is proportional to $T_i^{-1/2}$, so the important of coulomb collision is larger than elastic collision in the low temperature region.

Considering the order of the magnitude of thermal force by ion and neutral on the condition that the mass, velocity and density are the same, we estimate the collision frequency, since the thermal force is proportional to collision frequency ν. In the case of the collision between carbon ion(C^+) and hydrogen ion(H^+), the magnitude of the collision frequency is about $\nu_{imp}=1.4\times10^{-10}n_z$ (Hz) where T_i is 20 eV and n_z is C^+ density. On the other hand, the magnitude of the collision frequency between neutral hydrogen(H) and C^+ is $\nu_n=9.0\times10^{-17}n_n$ (Hz) where T_i is 20 eV and n_n is the neutral hydrogen density. Then ν_{imp}/ν_n is written as

$$\frac{\nu_{imp}}{\nu_n}=1.5\times10^6\frac{n_z}{n_n}.$$

If n_z/n_n is close to 10^{-6} , the order of neutral-impurity ion collision is effective. But carbon density is a few percent of the plasma density in the fusion plasma, so the neutral-ion collision is neglected, being compared with the ion-impurity collision.

With increasing powers and temperatures in the edge:

(1) the frictional force decreases, due to decreasing collisionality with increase in T

(2) the parallel diffusivity increases with T

(3) the parallel temperature-gradient forces (which push the ions away from the target) increase with power.

The ionization location is also important[39]. The roles of force balance and ionization location are discussed in more detail in [40].

In this thesis we deal with the thermal force to high charged ion (e.g. Ne VII, Ne VIII), so we do not consider the thermal force in a low electron temperature region($T_e\sim1$eV) where the pressure balance does not hold along the magnetic field line.

3.3 Detachment / MARFE

Detachment

Generally, the state of detachment is characterized by a strong reduction in plasma temperature adjacent to the divertor plate, coincident with significant decrease in plasma particle and pressure.

The partially detached divertor plasma operation is currently considered to be the primary solution to the engineering problem of the divertor of fusion reactors to accommodate the power exhausted from the core plasma. For the high recycling regime, the plasma flux is related with the temperature such as $\Gamma_{//} \propto 1/T_{div}$. The decrease in plasma temperature in front of the target means the increase of plasma flux to the target. The decrease in the power density convected through the sheath is partially compensated by the increase in recombination and radiation power. If the divertor temperature can be reduced below 1eV, the recombination process works well. The plasma particles would recombine before reaching the target surface. The plasma particle flux onto the target would be reduced and the heat load problem can be solved.

At high plasma density or when the volumetric power losses such as impurity line radiation is large, the plasma temperature decreases. When the plasma temperature in the divertor region is sufficiently low, i.e.< 10eV, the rate of neutral ionization is reduced and becomes smaller than the rate of ion-neutral friction, such as charge-exchange and elastic scattering. In this situation, as the ion momentum is lost through the ion-neutral friction processes, the total plasma pressure along the magnetic field line does not remain constant. The total pressure balance is written with the fractional loss of pressure due to friction f_m as $2n_tT_t=f_mn_uT_u$.

The plasma detachment was analyzed very early in the history of plasma physics. We use here the results for the case of hot ions (T_i=T_e). This results were derived in fully-analytic solutions in one dimension for an isothermal plasma with both isothermal plasma with both ionization and friction processes occurring simultaneously by S.A.Self and N.H.Ewald[41]. The ratio of plasma densities between entrance of recycle region and target plate is given by

$$\frac{n_r}{n_t}=\left(\frac{\alpha+1}{\alpha}\right)^{\frac{\alpha+1}{2}} \qquad (3.6)$$

$$\alpha \equiv \frac{<\sigma v>_i}{<\sigma v>_i+<\sigma v>_m} \qquad (3.7)$$

where $<\sigma v>_i$,$<\sigma v>_m$ are the rate coefficients for ionization and momentum loss. The fractional loss of pressure due to friction f_m is given by

$$f_m=2\left(\frac{\alpha}{\alpha+1}\right)^{\frac{\alpha+1}{2}} \qquad (3.8)$$

and its temperature dependence is shown in figure 3-2. The effect of friction processes on the pressure drop across the recycling region is negligible at >10 eV and becomes important at lower values of temperature.

MARFE

A MARFE is an axisymmetric, strongly radiating belt of short poloidal and radial extent located at the high-field edge of the plasma. "MARFE" is an acronym of "multifaceted axisymmetric radiation from the edge"[42,43]. Study on the MARFE is a matter of importance for tokamak reactor, since the MARFE is a radiation instability which occurs around the main plasma and rapidly cools the core periphery. This radiation instability is caused by the increases in line radiation from impurities with decreasing temperature as shown in figure 3-2. When MARFE occurs, τ_E decreases strongly due to increases in impurity in the core plasma and MARFE sometimes leads to a plasma disruption, which might be related to the density limit. The density limit disruption is due to the contraction of the temperature profiles at the edge of the core plasma which leads to an MHD-unstable configuration[44]. Therefore MARFE should be avoided to achieve good confinement.

In a sense, the MARFE-type state is always present near the target by the close proximity of impurity sources. The MARFE tends to occur as poloidal locations most remote from the cross-field heat source; in a limiter plasma the MARFE tends to form at the inside mid-plane. Whilst in a divertor machine, the MARFE tends to develop in the x-point region; the effective heat conduction coefficient becomes very small near the x-point due to the shallow pitch angle. The strong radiation around the x-point is attributed to the long connection length.

In JT-60U, carbon is the major impurity source. The radiative cooling rate of carbon has a maximum in the temperature range of 10-40 eV, where the radiated power can rise by orders of magnitude. With the MARFE occurrence, the fraction of the divertor radiation loss to the net power increases up to 40-60 % where the carbon impurity C^{3+} radiation is dominant[24]. In the case of the ion ∇B drift toward the x-point, divertor bolometric measurement shows that the radiation profile expands over a wide region near the x-point, particularly at the outside of the x-point. In contrast, in the case of the ion ∇B drift away from the x-point, the radiation region existing around the x-point moves to the high field side along the plasma boundary and finally stays at the upper region of the torus. An example of the formation of the x-point MARFE in the case of the ion ∇B drift toward the x-point is shown in figure 3-3.

The separation of the radiating region away from the target may be explained that the plasma temperature close to the target decreases below the value where appreciable carbon radiation can occur and the plasma density close to the target decreases. In experiment, the MARFE is formed after the occurrence of plasma detachment.

4. Impurity

4.1 Impurity problem

The presence of impurities is one of the most severe problems for a reactor. The impurities are of two types. Firstly there are impurity ions which come from solid surfaces, and secondly there are α-particles, ^{4}He, resulting from the fusion process. The design has to be such as to minimize incoming impurities but clearly the α-particle impurity is intrinsic. The requirement for the 'helium ash' is that it should not have too long a confinement time in the plasma.

Impurities from the wall produce partially stripped ions which then give rise to plasma energy loss through radiation. This is discussed quantitatively in section 4.5. In addition, fuel dilution by impurities pose a problem. Each ion is associated with a number of electrons determined by its ionization state. Since these electrons from impurity will have the same temperature as the plasma has, impurities can be regarded as having displaced fuel ions of deuterium and tritium for a given confined plasma energy. A heavy metallic ion can release tens of electrons in the center of the plasma.

Control of the impurity influx depends upon a satisfactory design of both the magnetic structure and the material surfaces receiving the outflow of plasma energy. At present this is believed to require a magnetic divertor. The aim of divertor is to lead the outgoing particles to a 'target' surface well separated from the plasma, and to restrict the impurity back-flow. A difficult problem associated with the divertor is that of limiting the power density flowing to the target surface. This is necessary to avoid high surface temperatures which can lead to surface melting or catastrophic impurity release by evaporation or other processes.

4.2 Impurity generation mechanism

In tokamaks, application of low Z materials, such as carbon or beryllium, to the first wall has contributed to high plasma performance. In JT-60U, the divertor plate consists of carbon fiber composite (CFC) tiles and the wall of carbon tile. As a result, carbon has become a major impurity [31]. Impurities are generated mainly by the physical sputtering, chemical sputtering and self-sputtering, desorption of adsorbed gases, sublimation, arcing, from the divertor plate and the wall. Impurities can be desorbed by incident ions, neutrals, electrons, and photons. The yields of electron and photon processes are low, particularly in the case of photon. The yield from electrons is typically two or three orders of magnitude lower than that for ions, ions and neutrals having similar yields.

4.2.1 Physical sputtering

An energetic hydorgenic ion/neutral striking a solid surface can, via momentum transfer to an atom of the substrate, dislodge it from the surface (physical sputtering). This process is enhanced by acceleration of ions in the sheath. The physical sputtering yield has a threshold. The physical sputtering yield is dominant in the high energy range(>>100eV). At low energy, that is < 100eV, the hydrogenic physical sputtering yield decreases rapidly. If the impurity particle becomes ionized by entering the plasma, then when it returns to the target due to acceleration of sheath potential, it can do so as an energetic ion also causing sputtering (physical self-sputtering).

4.2.2 Chemical sputtering

Chemical sputtering is due to the reactive nature of carbon. By the chemical reactions, the methane and heavier hydrocarbons can be formed and released into the plasma with thermal energy. Unlike physical sputtering, the chemical sputtering has no threshold and its yield increases with increasing temperature of the target plate as shown in figure 4-1. At low incident energy, the chemical sputtering compensates for the exponential drop-off in the physical sputtering, and so the total yield is approximately energy-independent from extremely low energies to about 1 keV. The chemical sputtering appears to be important for carbon impurity production in high density divertor regimes where the low incident energy is associated with large particle fluxes.

4.3 Impurity transport in divertor plasma

A long chain of processes connects the impurity production point, mainly at the divertor target, to the impurity density at the center of the confined plasma. Impurity production would not, in itself, have any influence on plasma behavior - beneficial or detrimental - were it not for the fact that the impurity particles can be transported within the plasma, far from their point of entry.

Impurities in the edge region are considered to be desirable for proposed ITER divertor solutions[45], since the associated edge impurity radiation disperses the heat flux which would be otherwise highly focused on the divertor plates.

An attractive possibility for power removal is to puff a gas such as neon in order to disperse the power by its radiation. Ideally, one would retain the impurity entirely within the divertor volume, radiating there, and keeping the core clean. Theoretically, e.g., in the high recycling plasma, the ion temperature gradient from the target to the upstream increases and the plasma flow velocity at the upstream decreases, the net force pushes impurity ions to the upstream. Thus the enhanced frictional force which overcomes the thermal force is required to suppress the core impurity contamination. Gas puff into the upstream SOL and pump from the divertor region, "puff and pump", is one of the methods to enhance the plasma flow.

A critical question then is how to achieve good divertor retention. A number of divertor retention studies employing He,Ne,Ar, etc.., have now been carried out on various tokamaks [46-56]. A review on the impurity transport in the divertor was recently presented in [57].

In most of the diagnostics for impurity study, such as spectrometer and bolometer, some information on impurity distribution is missing in experimental data. And also the flow velocity and temperature in the SOL strongly influence impurity transport, but there are few measurements of such plasma parameters so far. To understand the impurity behavior, many simulation codes, e.g. DIVIMP[58], IMPMC[59] and MCI[60], have been developed. In these codes, impurity behavior is simulated with Monte Carlo method which has many advantages for impurity modeling.

4.4 Impurity transport in core plasma

Impurity ions present in the center of the confined plasma dilute and radiatively cool the plasma. As a general feature it was noticed that the impurity accumulation problems could be considered as an undesired effect of a fundamental improvement of both the energy and particle confinement.

A discussion of impurity transport involves consideration of both neoclassical and anomalous processes since experiments show evidence of both effects[61-63]. The distinctive feature of neoclassical impurity particle transport follows from the relation (4-1) between fluxes and momentum exchange.

$$\Gamma = -\int\left(\frac{m}{ZeB}\int v_{//}C\left(f^{(1)}\right)d^3v + n\frac{E_{//}}{B}\right)I\frac{dS}{|\nabla\psi|} \quad (4\text{-}1)$$

The first term gives the collisional diffusion and it is seen that it is related to the exchange of momentum in collisions. Since like-particle collisions cannot create momentum they do not cause diffusion. If collisions between ion and impurity ion vanishes, stationary state occurs. The condition for this is

$$\frac{1}{n_z}\frac{dn_z}{dr} = \frac{Z}{n_i}\frac{dn_i}{dr} + \frac{\alpha}{T}\frac{dT}{dr} \quad (4\text{-}2)$$

where n_z is the density of an impurity species of charge Z, n_i is the plasma ion density and the coefficient α depends on the details of the thermal force. In the absence of the thermal force, eqn(4-2) implies a concentration of impurities towards the magnetic axis according to the relation

$$\frac{n_z(r)}{n_z(0)} = \left(\frac{n_i(r)}{n_i(0)}\right)^Z . \quad (4\text{-}3)$$

This relation has potentially serious implications for radiation losses from impurities.

In JT-60U, to investigate the behavior of the impurity ions in the core plasma, the IMPACT code (IMPurity Analysis Code for Tokamak plasma) has been developed by Hirayama[64,65].

4.5 Impurity radiation from plasmas

Tokamak plasmas almost contain impurity ions in addition to hydrogen and deuterium ions. The impurities originate from the torus wall, the limiter, or from the divertor-plates. Typical impurities are low Z ions of beryllium, carbon and oxygen, and high Z ions of iron and nickel. This distinction in Z is made because at the plasma center the low Z ions are fully ionized whereas the high Z ions are usually not quite fully ionized even in very high temperature tokamak plasmas. Towards the plasma edge all the ions are in low states of ionization. Impurities play an important role in the overall plasma energy balance, since a significant fraction of the input energy is often lost through radiation processes.

Many processes contribute to the radiation in a plasma and if it is magnetized, synchrotron radiation is also emitted. Line radiation arises from excitation by electron impact followed by the radiative decay of the excited state and also from de-excitation following radiative or dielectronic recombination of plasma electrons with ions. Line radiation can represent a major source of energy loss from the plasma and offers an important method of identification of the impurities from the characteristic wavelengths of the radiation.

The power radiated from a given impurity species is proportional to the electron density n_e and to the impurity density n_z, and the radiated power density P may be written as

$$P = n_e n_z L_Z \quad (4\text{-}4)$$

where L_z is the radiative power loss emission rate coefficient and is a function of the electron temperature as shown figure 4-2[66-69]. The L_z curve also depends on a "residence parameter", $n_e \tau_{res}$, where τ_{res} is the impurity residence time in plasma. In the plasma boundary, the proximity of the impurity source is important and impurities do not usually stay in the plasma long enough to come into coronal equilibrium. An impurity ion in the boundary has more electrons than it would have in the coronal equilibrium and therefore highly elevated levels of radiation can be found. The L_z of carbon for different values of residence parameter $n_e \tau_{res}$ is shown in figure 4-3. L_z for low-Z impurities tends to be maximal at low values of electron temperature. For carbon, the maximum radiation occurs at a temperature of around 10 eV.

Continuum radiation arises from electron-ion collisions, which produce bremsstrahlung, and also from recombination. The recombination radiation spectrum is continuous above a threshold energy corresponding to the binding energy of the captured electron. Measurements of the continuous radiation spectrum are chiefly used to determine the plasma electron temperature and effective charge

$$Z_{eff} = \sum n_z Z^2 / \sum n_z Z \quad (4\text{-}5)$$

with the summation running over all the charge states of all ion species.

For low Z impurities such as carbon and oxygen the maximum radiation occurs at a very low temperature, of the order of tens of eV. The ions of these impurities are fully stripped at a temperature of 1 keV and in the hot plasma of a reactor they would only radiate through bremsstrahlung. At the plasma edge radiation losses arise from the incompletely stripped impurities.

For high Z impurities, including the metals of which the tokamak is constructed, the first maximum in radiated power occurs at a somewhat higher temperature. For temperatures above 100 eV the radiation per ion is much greater than for low Z impurities. Even at reactor temperatures these ions are not fully stripped and the radiated power is such that the level of high Z impurities must be very small in a reactor.

In the core region, most low-Z impurities are usually in coronal equilibrium and are fully stripped of their electrons. Therefore, the radiation loss is mainly due to Bremsstrahlung which is the resulting radiation due to the acceleration of an electron during a collision with an ion being caused by the Coulomb force. In the divertor region, low-Z impurities are not fully stripped and significant radiation can occur. The radiation loss occurs through the atomic processes of line radiation from low-Z impurities.

5. Impurity transport in the divertor in neon gas puff experiment

5.1 Introduction

One of the concerns in tokamak operation is concentration of heat flux at the divertor plates. Dense and cold divertor is a promising scheme for reducing the erosion of divertor plates and enhancing radiative cooling, impurity screening and helium exhaust. Radiative cooling and the formation of dense and cold divertor requires full utilization of atomic processes and plasma dynamics. In the study of plasma confinement and control of the heat flux, the radiation loss measurement with bolometer arrays plays an important role to obtain knowledge of energy balance.

Neon gas has been used in radiative divertor experiment as a seed gas to investigate impurity behaviors. Since impurity ions in the main plasma dilute hydrogen ions and cool down the main plasma, it is necessary to confine the impurity ions in the divertor plasma as much as possible using the SOL flow by gas puffing at the main plasma and pumping at the divertor [70-72].

This chapter presents a basic spectroscopic study of neon impurity for investigating impurity behaviors in divertor plasmas in JT-60U on the condition that carbon is the dominant impurity and neon is trace amount. In section 5.2, the experimental procedures are described, the neon line spectra are identified, and the radiation due to neon line emission is estimated. Section 5.3 describes behavior of impurities during detachment/MARFE. A discussion is made in section 5.4 and conclusions are summarized in section 5.5.

5.2 Estimation of neon radiation

Figure 2-11 shows the main diagnostics, its viewing chords and puff position in neon gas puff experiment. An expanded view of divertor region and arrangement of diagnostic measurements is shown figure 2-12. The neon gas puff experiments are performed in NB-heated discharges, with following parameters: $I_p = 1.2$ MA, $B_t = 3.5$ T, $P_{NB} = 25$ MW, $q_{eff} = 6.1$ and the plasma volume is 65-67 m^3. Here, I_p is the plasma current, B_t the toroidal magnetic field, P_{NB} the total neutral beam power and q_{eff} the effective safety factor.

Figure 5-1 shows the time evolution of two discharges with neon gas puff. The solid and dotted line represent discharges with and without pumping, respectively.

Neon gas is puffed at 5 Pa m^3 s^{-1} between 6.5 and 6.9s and at 2 Pa m^3 s^{-1} after 6.9s. From 7.0s deuterium gas puff is injected to increase the radiation loss and restrict the neon in the divertor plasma by SOL flow. The line averaged main electron density ($=\overline{n_e}$) gradually increases from 1.8×10^{19} to 3.0×10^{19} m^{-3} during NBI heating. The main plasma radiation gradually increases during strong NB injection following the $\overline{n_e}$ increment.

Fig. 5-2(a) shows the time evolution of ion saturation currents measured with the divertor Langmuir probe (probe 9). The strike point is situated around the probe 9. Fig. 5-2(b) shows the time evolution of the neutral pressure in the inner divertor region measured with an ion gauge(shown in Fig. 2-12) and Fig. 5-2(c) shows the time evolution of D α intensity measured along the line of sight that ends at the strike point. The ion saturation current starts to decrease steeply about 6.7 s around the strike point and the inner divertor plasma starts to detach about 6.7 s. The D α intensity and the divertor neutral pressure in the inner divertor region increases as the ion saturation current decreases due to the proceeding of the detachment both in the case of pumping on and pumping off.

In the case of pumping off, the MARFE appears about 7.5 sec. After the MARFE forms, the radiation in the main plasma increases about twice (Fig.5-1(d)) and the Ne X intensities measured with VUV spectrometer in the main plasma increases about 1.3 times (Fig.5-1(e)). Also the C VI intensities in the main plasma increase 4 times after the MARFE formation(Fig.5-1(f)). In the divertor region during the MARFE the C IV intensity measured with the multi-channel interference filter spectrometer increases about 5 times (Fig.5-1(i)) and the C II intensities increase about 1.5 times (Fig.5-1(j)). The Ne I intensity increment is, however, 200 ms later than the MARFE occurrence and its increment is about 4 times (Fig.5-1(h)). The divertor radiation in the whole divertor region increases twice before the MARFE(Fig. 5-1(g)). The profile of the radiation during the MARFE is shown in Fig.5-3. Before the MARFE, the radiation peak is located at the inner and outer strike points. During the MARFE, the peak of radiation moves to the X-point and its value increases 3 times (from 1.2 $\times 10^6$ to

3.6 $\times 10^6$ Wm^{-2}).

Figure 5-4 shows the impurity line intensity profiles in the divertor plasma and the shadow region corresponds to the sight line of divertor VUV spectrometer. Before the MARFE, the Ne I spectral profile(Fig.5-4(b)) has a peak within the VUV spectrometer viewing area, which covers the inner separatrix hit point. The inner strike point corresponds to the peak of C II intensity (Fig.5-4(d)) and to the peak of radiation (Fig 5-3). However, the peak of D α (Fig.5-4(a)) and Ne I is situated inside the inner strike point.

Figure 5-5(a)(b) show spectra(λ = 25nm - 130 nm is available) measured with the VUV spectrometer in the divertor plasma, without and with neon gas, respectively.

Lines from Ne IV - Ne VIII are identified and the intensive lines are shown in Table 5-a [73,74]. Neon lines which are difficult to identify or separate are not listed. The identified spectral lines are $2s^x2p^y$-$2s^{x-1}2p^{y+1}$ transition and these line spectra radiate intensively in the divertor region. The time evolution of neon line intensities from Ne IV - Ne VIII is shown in Fig.5-6. All the neon spectra have a maximal value at 7.25s in the case of pumping on. The neon radiation is estimated at this time for the wavelength range of 25 nm - 130 nm. Most of the neon line spectra are included in this wavelength. The branching ratio method is used so as to estimate the absolute sensitivity of VUV spectrometer at C IV(2s3p : 31.2 nm) to compare with the absolute intensity C IV(3s3p : 580.1 nm) measured with the multi-channel interference filter spectrometer. For estimating the neon radiation, it is assumed that the sensitivity of VUV spectrometer is constant in the VUV range. On this assumption, in this region the total radiation from neon is 1.1×10^4 W m^{-2} and the estimated radiation of neon spectral line in the divertor is shown in Table 5-(a). The calculated total neon spectral line radiation in the VUV range in the divertor plasma is about 10% of radiation measured by the bolometer. The rest of radiation is considered to originate from C II - C IV [32].

5.3 Behavior of impurity spectral line after the MARFE occurrence

The divertor plasma detaches similarly both in the case of pumping on and pumping off. However, the MARFE occurs at about 7.5 s without pumping but with pumping it does not. In this experiment the distance between the pumping aperture and the separatrix is 1.4 cm. It implies that the divertor pumping is effective to make the plasma flow to prevent the MARFE by the enhancement of the friction force. Fig. 5-6(a)-(g) show the time evolution of the line spectra measured with the VUV spectrometer from the top of the vessel. In the case of pumping off after the MARFE forms, the Ne VII intensities increase about twice (Fig.5-6(d)) and the Ne VIII intensities increase about four times(Fig.5-6(e)), but the Ne IV-VI (Fig.5-6(a-c)) and the C II, C III intensities decrease (Fig.5-6(f-g)).

In the case of pumping off the divertor measurements show: (i)the C IV(155.08nm) intensity measured with the divertor normal incidence spectrometer from the inner vessel wall decreases after 7.8 s (Fig. 5-6(h)). (ii)The Ne I intensity measured with the interference filter spectrometer increases after 7.8s as shown in Fig. 5-1(h). (iii)The ion saturation current decreases to zero level at 7.8 s. These experimental results (i)-(iii) imply that the downstream temperature is too low for the neon to ionize to the high ionization stage, the neutral neon increases and the ion flux decreases almost to zero in front of the target plate after 7.8 s. Considering the ionization potential of the C IV is 64.5 eV and the Ne IV is 97.1 eV(the ionization potential is shown in table 5-(a)), Ne VII, VIII are ionized in the upstream region. This phenomenon is discussed in the next section.

5.4 Discussion

The estimated neon radiation is ～10% of the total divertor radiation. Such a low power is also supported by comparing the time evolution of radiation and carbon line with that of neon line spectra. That is, neon line spectra have a maximum value at 7.25 s and then decrease (Fig.5-6(a-c)). However, the divertor radiation increases until 7.5 s (Fig.5-1(g)). Furthermore, the radiation and carbon intensities (C II, C IV) have the same peak position (Fig.5-3, Fig.5-4(c)(d)). These observations suggest that most radiation in the divertor plasma comes from carbon (C II - C IV) and deuterium.

As ion saturation current shows, the detachment occurs at about 7.2 s (Fig. 5-2(a)). As Fig.5-6 shows, in the case of pumping off the line intensities of highly ionized impurities(Ne VII, Ne VIII) increase simultaneously with the formation of the MARFE in the divertor plasma. After the MARFE forms, these intensities of highly ionized neon increase further. However, the line intensities of lowly ionized impurities(C II, C III, Ne IV, Ne V, Ne VI) decrease. One might argue that Ne VII and Ne VIII radiate in the main plasma and the highly charged state neon moves (Ne IX, X, XI) to the lower charged state (Ne VII, Ne VIII) due to the decrease of the peripheral temperature of the main plasma by the MARFE. If this supposition is true, Ne VI would increase too because the difference of the ionization potential between Ne VI and Ne VII is small (about 50 eV).

Two explanations are possible for this phenomenon. One is increment of temperature in the divertor plasma and the other is the movement of lowly charged ions to the upstream. The measurement of Langmuir probes shows the contrary: before the detachment T_e~11 eV(6.0s), after the divertor plasma detaches T_e< 6.5 eV(7.2s) at the strike point. As for the power density to the divertor, before the detachment occurs P_{NB} - $P_{rad(main)}$ = 20 MW(6.0s), and after the detachment occurs P_{NB} - $P_{rad(main)}$ = 17 MW(7.2s). The decrease in the power density to the divertor supports the decrease in temperature in the divertor plasma.

The detached divertor evolves into MARFE only in the case without pumping. After the detachment is formed, the flow velocity to the divertor is considered to be reduced and the friction force weakens. So this phenomenon suggests that the lowly ionized ions move to the upstream due to the thermal force which works proportional to ∇T_e and ∇T_i to the direction of the high temperature region and then the detached divertor evolves into MARFE [75]. More impurities in the divertor region move to the upstream in the case of pumping off because the plasma flow velocity and friction forces are weaker than in the case of pumping on. When impurity ions are carried to the upstream by the thermal force, they are ionized to higher ionization stages. This explains why the intensity of highly ionized ions, Ne VII and Ne VIII, are increasing.

A detailed comparison between code and experimental results has not been made. The divertor modeling and the impurity transport simulation during the MARFE are future study.

5.5 Conclusion

The divertor plasma detaches similarly both in the case of pumping on and pumping off. In the case of pumping on, the MARFE does not occur. However, in the case of pumping off, the MARFE occurs after the divertor plasma is detached. It implies that the divertor pumping is effective to make the plasma flow and the friction force strong enough to prevent the MARFE.

The spectral line intensities from highly ionized neon (Ne VII, Ne VIII) increase simultaneously with the formation of the MARFE. After the MARFE forms, the spectral line intensities of Ne VII and Ne VIII increase further. This observation suggests that impurities in the divertor flow back to the upstream because of thermal force, so that in the case of pumping off more impurities flow back and the detached plasma evolves to MARFE.

In the neon gas puff experiment, neon line spectrum identification was made in the divertor plasma between λ = 25 nm - 130 nm covered with VUV spectrometer.

By using the divertor VUV spectrometer combined with the divertor interference filter spectrometer, we estimate the radiation from the neon line emission measured with

VUV spectrometer between $\lambda = 25$ nm - 130 nm. The radiation of the neon line spectra in this region is estimated to be about 10% of the power measured with the bolometer array.

6. Impurity radiation and transport of hot plasma core close to break-even condition in JT-60U reversed shear discharges

6.1 Introduction

The neoclassical transport theory predicts accumulation of higher charge state impurities in the plasma center[76]. This is a serious problem because fuel dilution due to impurity directly affect fusion performance. As the rate of neutron emission is proportional to $n_d{}^2\ f(T_i)$, the fuel dilution strongly decreases nuclear fusion reaction. In addition, accumulation of metallic impurities in the plasma cools the plasma core by radiation loss[77], and sometimes excessive radiation cooling causes a disruption. Impurity possesses such properties undesirable for plasma confinement. Control of the impurity amount and the density profile are therefore very important issues in the optimization of the fusion reactor core [78].

The reversed shear configuration is one of the leading scenarios for tokamak reactors that is characterized by good confinement and a large fraction of well-aligned bootstrap current [79-81]. Enhanced core confinement or formation of an internal transport barrier (ITB) has been observed in reversed shear discharges in many tokamaks [13,82-88]. On the other hand, reversed shear discharges might have a potential difficulty of impurity accumulation because the density is highly peaked and the discharges are free of sawtooth and ELMs. Many devices indicate impurity accumulation in the core region without sawtooth and ELMs [89-91].

In JT-60U, improvement in the fusion performance was intensively attempted in the reversed shear plasma and the record value of equivalent fusion multiplication factor Q_{DT} of 1.25, has been achieved at a plasma current of 2.6MA after the divertor modification in 1998. The improved performance is reported to be mainly attributed to a decrease in Z_{eff} [19,92].

In JT-60U, the particle transport of several impurity ion species(helium, carbon and neon) was investigated in reversed shear discharge at the ITB region [7]. The particle diffusivity was almost the same for all ions, while the inward pinch velocity was larger for ions having higher charge state and the obtained results were qualitatively consistent with neoclassical theory.

This section presents a comprehensive analysis about carbon impurity behavior and power balance in the core plasma including radiation, spectroscopy, bremsstrahlung, and neutron emission in reversed shear plasma close to the break-even condition. In section 6-2, the experimental procedures are described. Section 6-3 deals with investigations of core radiation and its source in the reversed shear discharges. Evaluation of carbon impurity density in a main plasma is discussed with bolometer, spectrometer, neutron emission and CXRS measurement in section 6-4. Section 6-5 describes the discussion about the impurity transport comparison with the neoclassical theory. A summary is presented in section 6-6.

6.2 Experimental procedures in the reversed shear discharge

A typical waveform of a reversed shear discharge is shown in Fig. 6-1. The reversed shear experiments were performed by NB heating of I_p ramp-up discharges for I_p = 1.2 - 2.6 MA, P_{NB} = 10-20 MW and the plasma volume was 51-58 m^3. The plasma major radius was 3.1 to 3.2 m, the plasma triangularity was 0.025, the plasma elongation was 1.9, the plasma minor radius was 0.65 to 0.70 m, the height of the magnetic axis from the mechanical midplane of the vacuum vessel was about 0.2 m. A schematic view of the related diagnostic sightlines of the high performance reversed shear discharge is shown in Fig.2-13. An explanation for diagnostics are described in section 2.2.

The plasma current is ramped up, and stored energy and the averaged electron density increases during the discharge. The ramp-up of plasma current continues after the formation of ITB around 4 s, and the plasma stored energy W, neutron production rate S_n and line averaged density continues to rise. The H-factor just before the disruption(t=6.94s) is 3.21. The enhancement in fusion performance can be attributed to optimized increase in I_p and combination of parallel, perpendicular, co/counter neutral beams during the current ramp-up. Perpendicular NBI power is 8.7 MW and the power of co/counter NBI is 4.3 / 4.4 MW, respectively. Parallel NBI power is 4.0 MW and the power of co / counter NBI is 2.1 / 1.9 MW, respectively. The C VI(1s-2p : 3.7 nm) and O VIII(1s-2p : 1.9 nm) line intensities remain at about the same level up to the end of the plasma discharge.

6.3 Analysis of core radiation in high performance fusion plasmas

The core radiation is analyzed for the highest performance plasmas at 6.94 s shown in Fig.6-1, when the maximum value of plasma current(I_P) and stored energy(W) are obtained. The radiation at the central chord(ch 14) increases till 4.85 s after the input power reaches its maximum(4.3s), then gradually decreases. Figure 6-2 shows more details of bolometer array signal. The radiation at the edge chord(ch2) gradually decreases from 6.3 s as the plasma volume is reduced.

The core radiation is analyzed with the lower bolometer array which views the upper half of the main plasma, assuming up-down symmetry of the main plasma radiation. The core radiation loss is estimated with Wiener-filter Abel inversion method[93], which deals with elongation, triangularity and the shift of the plasma center. The radiation in the SOL region is taken into account.

Figure 6-3(a) shows the line integrated radiation of each bolometer channel with a fitted curve and (b) shows the volumetric radiation at different times. Inverted profiles show that the radiation is being pronounced in the core region.

Charge exchange due to neutral beam injection is considered to affect the power balance in two ways. One is particle loss due to charge exchange. The other is enhancement of radiation due to charge exchange recombination because charge exchange recombination due to neutral beam injection shifts the impurity equilibrium towards lower charge states, which leads to an enhancement in line radiation due to electron impact excitation.

First, we calculate charge exchange loss due to neutral beam injection using orbit following Monte Carlo code (OFMC)[94]. The total charge exchange loss inside ITB (ρ <0.5) is 0.01 MW and is negligible compared with bolometric radiation of inside ITB of 0.68 MW. Second, we estimated the enhancement of radiation due to charge exchange recombination as ~0.003 MW inside ITB (ρ <0.5) and is negligible, too. Therefore, we do not have to consider the effect of charge exchange toward the power balance in the ITB region. Also the OFMC result shows that the measured radiation is under 15 % of absorption power inside ITB (4.9MW) and the radiation loss from the core plasma is small.

The radiation from each impurity species is calculated using the radiative cooling rates indicated by the following equation.

$$P_{rad} = n_e n_z L(z) \qquad (6.1)$$

where n_e is electron density, n_z is impurity density and L(z) is the cooling rate by solving the rate equation in average-ion model[95]; including atomic processes such as collisional ionization, radiative recombination, dielectronic recombination, three-body recombination, bremsstrahlung and collisional excitation.

In this experiment intensity of boron emission signal is very low, so it is considered that the dominant impurities are carbon and oxygen. This density ratio of carbon to oxygen is estimated from the brightness ratio of C VI 1s-2p to O VIII 1s-2p.

The ratio is insensitive to the plasma parameters and it is proportional to the density ratio of carbon to oxygen [96]. The relative sensitivities at wavelengths of between 1.9 nm and 3.7 nm are calibrated using a branching ratio method. The absolute densities of carbon and oxygen are obtained from this density ratio and Z_{eff}. Then we obtain n_c/n_e=4.0% and n_o/n_e=1.9% using Z_{eff}=3.28 derived from bremsstrahlung measurement.

The radiation loss due to metallic ions is evaluated as follows. Fe and Ni lines with 2s-2p transition are measured around 10 nm where their contribution to the radiation is considered to be dominant [28]. In this high performance reversed shear discharges, since the plasma is separated well (~0.7m) from the first wall on the outboard side, not only many lines from Fe and Ni ions around 10 nm are not observed but also line emissions from metallic ions(Fe XXIV 19.2nm, Ni XXV 11.8nm, Fe XXIII 13.3nm) are noise level. Therefore the radiation from metallic ions is considered to be negligible.

The estimated contributions to the radiation loss are shown in Figure 6-4. The last separatrix is situated at ρ=0.987 m in this experiment. The estimated impurity radiation is 0.74 MW, here n_e= 8.4×10^{19} m^{-3},T_e= 8.6 keV. The bolometrically measured core radiation(ρ < 0.5 m) is 0.68 MW which agrees with the radiation estimated spectroscopically within 10%.

In the temperature range of interest, light impurities are fully-stripped so radiative cooling is considered to be dominated by bremsstrahlung. The bremsstrahlung radiation is expressed as follows with T_e in keV:

$$P_{br} = g\frac{e^6}{6(3/2)^{0.5}\pi^{1.5}\varepsilon_0^3c^3hm_e^{1.5}}Z^2n_en_iT_e^{0.5}\ \mathrm{Wm^{-3}} \qquad (6.2)$$

where g is the gaunt factor which gives a quantum mechanical correction. Under the conditions of interest, g is equal to $2\sqrt{3}/\pi$. Fig. 6-3(c),(d) shows n_e and T_e profile are approximately flat inside ITB with central values of 8.4×10^{19} m^{-3}, 8.6 keV, respectively. We can estimate the bremsstrahlung radiation from each impurity species(carbon, oxygen) to be 0.66 MW which corresponds to 97% of measured core radiation.

The contribution by radiative recombination is small(<10%). The error of radiation inside ITB from Abel inversion is around 10% for bolometer measurement. The spectroscopically estimated total radiation agrees with the bolometric radiation within 10%.

6.4 Carbon density profile in the main plasma

The neutral beam deposition profile is calculated simply assuming Z_{eff} (=3.22 derived from neutron emission assuming carbon and oxygen as the dominant impurity) is constant over the averaged volumetric radius(Fig.6-5(a)). Although the bremsstrahlung profile measurement cannot exclude the change of Z_{eff} in the outer radii($\rho > 0.8$ m), when the Z_{eff} is small, the Z_{eff} dependence of the beam attenuation is small[29] since the beam attenuation depends on n_e, n_z. As a result its effect is small (<5%) on the profile of carbon density estimated from CXRS. The estimated spatial distributions of carbon density at 6.94s are shown in Fig. 6-5(b). The carbon density has a peak in the core region and the carbon density increases steeply in the ITB region. In this experiment, the carbon density in the core region (ρ =0.4 m) is about 6 times larger than in the edge region (ρ =0.8 m). The time evolution of the carbon density is shown in Fig. 6-6(a). The spatial distributions of carbon density normalized by electron density n_c/n_e and their time evolution are shown in Fig.6-6(b). Experimental results indicate that the carbon fractions(n_c/n_e) are almost flat around 3-4% over the volumetric averaged minor radius inside the ITB region and constant, which is in a good agreement with the estimation from VUV measurement(4.0%). The n_c/n_e does not increase inside ITB during density rising. But the carbon density monotonically increases from 6.2s inside ITB.

6.5 Discussion

Next we discuss a quantitative comparison of the experimental results with the neoclassical theory. The particle flux is described as,

$$\Gamma = \Gamma^{\text{class.}} + \Gamma^{\text{P.S.}} + \Gamma^{\text{neo-class.}} \quad (6.3).$$

where the first term is the flux of classical transport, the second term the flux from the Pfirsch-Schluter contribution, and the third one the flux from the neoclassical contribution. There are three collisionality regimes(the banana, plateau, and Pfirsch-Schluter regimes) that can be distinguished with ν^* being the dimensionless collisionality number they pertain to the respective intervals: $\nu^* < 1$, $1 < \nu^* < \varepsilon^{-3/2}$, $\varepsilon^{-3/2} < \nu^*$ where $\varepsilon = r/R$ is the inverse aspect ratio. ν^* is the detrapping frequency normalized by the bounce frequency of the trapped particle and is defined[97] as

$$\nu_a^* = \frac{Rq}{v_{a,th}\varepsilon^{3/2}} \sum_b \nu_{ab}$$

$$= \varepsilon^{-3/2} \frac{4}{3} \sqrt{\pi} \ln\Lambda \frac{Rqe_a^2}{T^2 (4\pi\varepsilon_0)^2} \sum_b \sqrt{\frac{m_b}{m_a + m_b}} e_b^2 n_b \qquad (6.4)$$

where ν_{ab} is collision frequency between particle a and b, and m_a and m_b are the particle mass of a and b, respectively. T is ion temperature, ln Λ is the coulomb logarithm, R is the major radius, q is the safety factor, n_b is the particle density. The collisionality is in the range of $\nu^* < 1$ for carbon and $\nu^* < 1$ for deuteron, so the banana-banana regime is obtained in this experimental condition. The impurity particle flux Γ_I is calculated by the following equation,

$$\Gamma_I = -D_I \nabla_r n_I + D_I Z_I \left(\frac{\nabla_r n_i}{n_i} + H \frac{\nabla_r T_i}{T_i} \right) n_I \qquad (6.5),$$

where D_I is the impurity diffusion coefficient, H is a coefficient shown in table 6-a[98,99], n_I is the impurity density, T_i is the ion temperature, and n_i is the ion density. The Γ_I values derived from theory and experimental results are shown in Fig.6-7(a) and (b). The carbon flux density is negative and its magnitude monotonically increases toward the center. The tendency of the Γ_I profile and its time evolution is similar between experimental results and theoretical results. The calculated Γ_I based on theory is consistent with the Γ_I derived from experimental results within a factor of 2. Therefore the carbon impurity concentration is explained by neoclassical transport theory in the banana-banana collision regime. In the case of this discharge the carbon density is in a transient state(Fig.6-6(a)) and the plasma disrupts at the end of this stage. If the plasma is in a steady state, eq.(6-5) is written as

$$\frac{\nabla_r n_I}{n_I} = Z_I \left(\frac{\nabla_r n_i}{n_i} + H \frac{\nabla_r T_i}{T_i} \right) \qquad (6.6).$$

Solving this equation, we obtain

$$\frac{n_I(r)}{n_I(0)} = \left(\frac{n_D(r)}{n_D(0)} \right)^{Z} \left(\frac{T(r)}{T(0)} \right)^{HZ} \qquad (6.7).$$

This indicates that when the impurity transport follows the neoclassical prediction, the carbon accumulates as shown in Fig.6-7(c). There are three cases of carbon fraction having different H value and it shows that H dependence is small. We estimate a carbon accumulates as shown in Fig.6-7(c). There are cases of carbon fraction having different H value but Fig.6-7(c) shows that the carbon accumulates strongly for all H values. We estimate a characteristic time, τ_{ac}, for the carbon to accumulate in the core region according to the neoclassical theory. If the plasma does not disrupt at 6.94s and reach a steady state, the particle flux is estimated as follows.

$$\frac{dN_c}{dt} = -\int \Gamma_{exp} dS \qquad (6.6)$$

where Γ_{exp} is ~-2×10^{18} $m^{-2}s^{-1}$ and the increase rate of the carbon density, $\dot{N}_c$, within $\rho < 0.5$ m is about 6.1×10^{18} s^{-1}. The carbon density derived from the neoclassical prediction $\rho < 0.5$ m, $N_{c\text{-}ss}$, is about 5.2×10^{19}. Therefore $\tau_{ac} = N_{c-ss}/\dot{N}_c$ is ~0.85 s. This may explain why a selective impurity accumulation is not observed.

These results imply that if the plasma is in a steady state, e.g. over ~1 s, the carbon impurity accumulates to the center selectively. If the carbon density outside ITB is constant during a steady state, n_c/n_e can reach ~0.1, then n_d/n_e becomes ~0.25 in the core region. Therefore it poses a problem of serious fuel dilution.

6.6 Conclusion

We evaluated the core radiation with the spectroscopic method in the reversed shear regime. During high performance discharges with reversed shear, the radiation profile strongly peaks inside the ITB radius and concluded that the 97% of radiation from inside the ITB radius is bremsstrahlung and this estimation is consistent with the bolometric measurement within 10%. The measured radiation is under 15 % of absorption power inside ITB (4.9MW) and the radiation loss from the core plasma is

The increment of carbon density is explained by neoclassical transport of banana-banana collision regime and the carbon particle flux derived from the neoclassical theory is consistent with the experimental results within a factor of two. However, spectroscopy study shows that n_c/n_e is flat inside ITB during the electron density increase. It implies that the carbon does not selectively accumulate inside the ITB. These apparent discrepancies may be explained by the transient nature of the discharge If the reversed shear plasma is sustained ～1s longer, the carbon accumulation may become a problem to the core plasma performance.

7. Summary and conclusions

The impurity behavior in fusion plasma is recognized as an important study for demonstrating the ignition for a long pulse. In this thesis two aspects of impurity transport are investigated.

In the divertor impurity transport study, following results are obtained.(i) The divertor plasma detaches similarly both in the case of pumping on and pumping off. In the case of pumping on, the MARFE does not occur. However, in the case of pumping off, the MARFE occurs after the divertor plasma is detached. It implies that the divertor pumping is effective to make the plasma flow and the friction force strong enough to prevent the MARFE. (ii) The spectral line intensities from highly ionized neon (Ne VII, Ne VIII) increase simultaneously with the formation of the MARFE. After the MARFE forms, the spectral line intensities of Ne VII and Ne VIII increase further. This observation suggests that divertor impurities flow back to the upstream because of thermal force in the case of pumping off and the detached plasma evolves to MARFE. (iii) In the neon gas puff experiment, neon line spectrum identification was made in the divertor plasma between $\lambda = 25$ nm - 130 nm covered with VUV spectrometer. (iv) By using the divertor VUV spectrometer combined with the divertor interference filter spectrometer, we estimate the radiation from the neon line emission measured with VUV spectrometer between $\lambda = 25$ nm - 130 nm. The radiation of the neon line spectra in this region is estimated to be about 10% of the power measured with the bolometer array.

In the core impurity transport study, following results are obtained. (i) During high performance discharges with reversed shear, the radiation profile strongly peaks inside the ITB radius. We evaluated the core radiation with the spectroscopic method in the reversed shear regime and concluded that the 97% of radiation from inside the ITB radius is bremsstrahlung. This estimation is consistent with the bolometric measurement within 10%. (ii) The increment of carbon density is explained by neoclassical transport of banana-banana collision regime and the carbon particle flux is consistent with the experimental results within a factor of two. (iii)However, spectroscopy study shows that n_c/n_e is flat inside ITB during the electron density increase. The carbon fraction estimated from Z_{eff} and VUV spectrometer is consistent with CXRS measurement. It implies that the carbon does not selectively accumulate inside the ITB. This apparent discrepancy between (ii) and (iii) may be explained by the transient nature of the discharge. If a steady state is sustained for ～1s, the carbon accumulation may pose a problem to the core plasma performance.

Acknowledgments

It is a great pleasure to acknowledge the support and guidance of my supervisor, Prof. M.Shimada, who has been encouraging and stimulating throughout the three years that I have been at Naka Fusion Research Establishment of Japan Atomic Energy Research Institute in Japan. My thanks are also due to Prof. T.Tamano and K.Yatsu of University of Tsukuba for their continued support. I also wish to express my thanks to Prof. Y.Miura at JAERI.

I would like to express my gratitude to Drs. H.Kubo and S.Konoshima for many helpful comments and discussion throughout this thesis work. The encouragement by Drs. H.Kishimoto, A.Funahashi, M.Azumi, H.Ninomiya, R.Yoshino, M.Kikuchi at JAERI is gratefully acknowledged.

This thesis has been completely accomplishment with the assistance of a large number of engineers and physicists in the JT-60U project. Although too many to name individually, they are all deserving of my gratitude. In particular, I would like to record my appreciation for the friendship and valuable discussions with Dr.N.Asakura, Dr.N.Hosogane, Dr.T.Sugie, Dr.H.Tamai, Dr.K.Itami, Dr.K.Shimizu, S.Higashijima, Dr.H.Takenaga, Dr.S.Sakurai, T.Nakano, Dr.S.Suzuki, and Dr.A.Kumagai. Members of the GAMMA 10 group at University of Tsukuba is gratefully acknowledged.

Finally, I would like to thank University of Tsukuba and Naka Fusion Research Establishment of JAERI for organizing Cooperative Graduate School System and the Japan Scholarship Foundation.

References

[1] J. WESSON, Oxford Engineering Science Series 48 Tokamaks second edition, Oxford University Press, 1997.

[2] JET Team, Nucl. Fusion **32**(1992)187.

[3] S.Ishida et al., Phys. Rev. Lett. **79**(1997)3917.

[4] R.J. Hawryluk and TFTR Team, in 15th International Conference on Plasma Physics and Controlled Nuclear Fusion Research, IAEA -CN-60/A-1-I-1.

[5] The JET Team, Proc. of 17th Fusion Energy Conf., 1998, Yokohama, (International Atomic Energy Agency, Vienna).

[6] P.C. Efthimion et al., Proc. of 17th Fusion Energy Conf., 1998, Yokohama, (International Atomic Energy Agency, Vienna) <IAEA-CN-69/EXP1/15 >.

[7] H. Takenaga et al., Journal of Plasma and Fusion Research. **75**(1999)952.

[8] H. Chen et al., 25th EPS Conf. on Plasma Physics and Controlled Fusion (Praha) ECA Vol.22C (1998) 1947-1950.

[9] H. Ninomiya et al., Plasma Devices Operat. 143,(1990).

[10] Y. Koide and the JT-60 Team, Phys. Plasma **4** (1997) 1623.

[11] G. Janeschitz et al., Fusion Energy 1996 (Porc.16th Int. Conf. Fusion Energy, Montreal, Canada, 1996) vol.2, 755(1997).

[12] N. Hosogane et al., Proc. 16th Int. Conf. Montreal, vol. 3(IAEA,Vienna,1996), (1996) 555.

[13] T. Fujita et al., Phys. Rev. Lett. **78** (1997) 2377; 4529(errata)

[14] T. Fujita et al., Proc. of 17th Fusion Energy Conf., 1998, Yokohama, (International Atomic Energy Agency, Vienna) < IAEA-CN-69/EX1/2 >.

[15] Y. Kamada et al., Proc. of 17th Fusion Energy Conf., 1998, Yokohama, (International Atomic Energy Agency, Vienna) < IAEA-CN-69/EX9/2 >.

[16] H.Shirai and the JT-60 Team. Phys. Plasmas Vol.5 No.5,1712(1998).

[17] N. Hosogane et al., presented in 13th International Conference on Plasma Surface Interactions in Controlled Fusion Devices San Diego, USA, 18-22 May 1998.

[18] N. Hosogane *et al.*, Nucl. Fusion **34**(1994) 527.

[19] K.F.Mast, et al., Rev.Sci.Instrum.**62**(1991)744.

[20] Physikalisch Techmische Studien GmbH,"Bolometer System for JAERI" Proj.No.2041(1996).

[21] R.Reichle, et al., Proc.EPS Conf.(1995).

[22] S.Konoshima, et al., JAERI-Research **039**(1998) 145.

[23] H. Kubo *et al.*, Rev. Sci. Instr. **59** (1988) 1515.

[24] H. Kubo et al., Nucl. Fusion **33**(1993)1427.

[25] A. Sakasai *et al.*, Kakuyugo Kenkyu Vol 59 supplement,169(1988)

[26] R.C. Isler, et al., Phys. Rev. A (1981) 2701

[27] A.N. Zimovev, Pis'ma Zh. Eksp. Teor. Fiz. **32** (1980) 557 [JETP Lett. **32** (1980) 539]

[28] R.J.Fonck, et al., Phys. Rev. Lett. **49** (1982) 737

[29] S. Suzuki, et al., Plasma. Phys. Control. Fusion **40** (1998) 2097-2111.

[30] Y. Koide et al., Plasma Phys. Control. Fusion **36** (1994) A195.

[31] H. Kubo, et al., J. Nucl. Mater. **71**(1992)196-198.

[32] H. Kubo *et al.*, Plasma Physics Control Fusion **37**(1995)1133-40

[33] H.Tamai et al., JAERI-Research 98-039,p149.

[34] I. LANGMUIR,in Collected Works of Irving Langmuir,edited by G.SUITS,volume 4 and 5,Pergamon Press,New York,1961.

[35] Y.Kawano et al., Rev. Sci. Instrum. **67**(1996)1520.

[36] S.I. Braginsky, in: Reviews of Plasma Physics, Vol. 1, Ed. M.A. Leontovich (Consultants Bureau, New York, 1965) p.205.

[37] S. Chapman, Proc. Phys. Soc. **72** (1958) 353.

[38] J. Neuhauser et al, J.Nucl.Mater. **121** (1984) 194-195.

[39] Roth. J. et al., Nucl. Fusion **32** (1992) 1835.

[40] Stangeby P C and Elder J D, Nucl. Fusion **35**(1995)1391.

[41] S.A. Selfand N.H. Ewald., Phys. of Fluids **9** (1966) 2486.

[42] B. Lipschultz, J.Nucl.Mater. **145-147** (1987) 15-25.

[43] N. Hosogane *et al.*, Journal of Nucl. Mater. **196-198** (1992) 751.

[44] J. Wesson et al., Nucl. Fusion **29** (1989) 641.

[45] Janeschitz G et al., J. Nucl. Mater. **220-222**(1995)73.

[46] Roth J et al., Supplement to Nuclear Fusion **1** (1991) 63.

[47] Roth J et al., Nuclear Fusion **32** (1992)1835.

[48] Janeschitz G et al., Nuclear Fusion **26**(1986)1725.

[49] Janeschitz G et al., 17th EPS Conf. on Plasma Physics and Controlled Fusion(Amsterdam,1990) 14B, Part III,1365.

[50] Janeschitz G et al., 18th EPS Conf. on Plasma Physics and Controlled Fusion(Berlin,1991) Part III,97.

[51] McCracken G M et al., J. Nucl. Mater. **220-222**(1995)264.

[52] Kallenbach A et al., Nucl. Fusion **35**(1995)1231.

[53] Belanger C et al., Nuclear Fusion **31**(1991)561.

[54] Decoste R et al., Plasma Physics and Controlled Nuclear Fusion Research IAEA-

CN-56/A-6-4(1992).
[55] Decoste R et al., Phys Plasmas **1**(1994)1497.
[56] Terreault B et al., Nucl. Fusion **34**(1994)777.
[57] K. Shimizu et al., J. Nucl. Mater. **241-243**(1997)167.
[58] P.C.Stangeby and J.D.Elder, J. Nucl. Mater. 196-198(1992)258.
[59] K.Shimizu et al., J. Nucl. Mater. **220-222**(1995)410.
[60] A.M.Mahdavi et al., J. Nucl. Mater. **220-222**(1995)13.
[61] R.D. Petrasso et al., Phys. Lev. Lett. **57** (1986) 707.
[62] E.J. Synakowski et al., Nucl. Fusion **29** (1989) 311.
[63] G. Fussmann et al., J. Nucl. Mater. **162-164** (1989) 14.
[64] T. Hirayama, in Transport Simulataion in Large Tokamaks (Proc. 2nd US/Japan Workshop, Princeton, NJ, 1985); T. Hirayama et al., Rep. JAERI-M-82-204, Japan Atomic Energy Research Instuitute (1982).
[65] T. Hirayama et al., J. Nucl. Mater. **145&147** (1987) 854.
[66] Hulse R., Nuclear Technology/Fusion **3**(1983)259.
[67] Post D.E., Jensen R.V., Tarter C.B., et al., Atomic Data and Nuclear Data Tables **20** (November) (1977)397-439.
[68] CLARK R., ABDALLEH J., Post D.E., J. Nucl. Mater. **220-222** (1995) 1016-1120.
[69] Post D.E., J. Nucl. Materials **220-222** (1995) 143.
[70] K. Itami *et al.*, Plasma Phys. Contl. Nucl. Fusion Research (Proc. of 16th IAEA Fusion Energy Conf., Montreal, 1996). IAEA-CN-64/GP-11., vol 1, p.385.
[71] M. J. Schaffer *et al.*, J. Nucl. Mater., **241-243** (1997) 585.
[72] H. S. Bosch *et al.*, J. Nucl. Mater., **241-243** (1997) 82.
[73] H. S. Bosch *et al.*, Phys. Rev. Lett. **76** (1996) 2501.
[74] G, Fussmann *et al.*, J. Nucl. Mater. **121**(1984) 168.
[75] S. I. Braginskii, in: Reviews of Plasma Physics, Vol. 1, Ed. M.A. Leontovich (Consultants Bureau, New York, 1965) 222-224.
[76] F.L. Hinton et al., Rev. Mod. Phys. **42** (1976) 239.
[77] R.V. Jensen et al., Nucl. Fusion **17** (1977) 1187.
[78] M. Shimada, Fusion Engineering and Design **15**(1992)325.
[79] T. Ozeki et al., in Plasma Physics and Controlled Nuclear Fusion Research 1992 (Proc. 14th Int. Conf. Wurzburg, 1992), Vol. 2, IAEA, Vienna (1993) 187.
[80] C. Kessel et al., Phys. Rev. Lett. **72** (1994) 1212.
[81] A. D. Turnbull et al., Phys. Rev. Lett. **74** (1995) 718.
[82] F. M. Levinton et al., Phys. Rev. Lett. **75** (1995) 4417.

[83] E. J. Strait et al., Phys. Rev. Lett. **75** (1995) 4421.

[84] X. Litaudon et al., Plasma Phys. Control. Fusion **38** (1996) 1603.

[85] G.M.D. Hogeweij et al., Phys. Rev. Lett. **76** (1996) 632.

[86] M. Hugon et al., Nucl. Fusion **32** (1992) 33.

[87] JET TEAM (presented by C. Gormezano), in Fusion Energy 1996 (Proc. 16th Int. Conf. Montreal, 1996), Vol.1, IAEA, Vienna (1997) 487

[88] Y. Takase et al., Phys. Plasmas **4** (1997) 487.

[89] N. Fujisawa et al., Japan Atomic Energy Research Institute Report No. JAERI-M 9181 (1980).

[90] Doublet III Groups, J. Nucl. Mat. **93** & **94** (1980) 259.

[91] W. Engelhardt et al., in Plasma Physics and Controlled Nuclear Fusion Research (Proc. 7th Int. Conf. Innsbruck, 1978) IAEA, Vienna (1979) Vol. 1,123.

[92] S. Ishida et al., Proc. of 17th Fusion Energy Conf., 1998, Yokohama, (International Atomic Energy Agency, Vienna) < IAEA-CN-69/OV1/1 >.

[93] Y. Yamashita, JAERI-M 87-206 (1988).

[94] K.Tani et al., J. Phys. Soc. Jpn. **50** (1981) 1726.

[95] X. Bonnin, R. Marchand, R.K. Janev, Nuclear Fusion (1992) Atomic and Plasma-Material Interaction Data For Fusion,Vol 2,117.

[96] H. Kubo et al., Nuclear Fusion **29** (1989) 571.

[97] G. Fussmann et al., Plasma Phys. Control. Fusion **33** (1991) 1681.

[98] A. Samain, Workshop on Magnetic Confinement, Proc. Vol. I, p. 440, Santander, Spain, (1991)

[99] G. Fussmann, MAX-PLANCK-INSTITUT FUR PLASMAPHYSIK, IPP 1/273 (1992).

Table 2-a Main parameters of JT-60U

Toroidal magnetic Field B_ϕ : 4.2 T
Plasma major radius R_0 : 3.0～3.4 m
Plasma minor radius a : horizontal : 0.6～1.1 m
b : vertical : 1.0～1.7 m
Elongation b/a : 1.4～1.7
Plasma Current I_p : 2.5 MA
Positve Neutral Beam Injection P_{NB} : Perpendicular : 10units ～10MW
Tangential : Co- : 2 units ～ 5MW
Counter- : 2 units ～ 5MW
Negative Neutral Beam Injection N_{NB} : ～10 MW
ICRF (Ion Cyclotron Radio Frequency) P_{RF} : ～ 5.5MW
LHCD (Lower Hybrid Current Drive) P_{LH} : ～ 7 MW
Plasma Volume V_p : ～85 m^3
Gas puff port : 6 (4:main, 2:divertor)
Divertor pumping : 3ports, 35 m^3/s each
Helium pumping : Argon frosting possible

Table 2-b Summary of JT-60U diagnostics systems

Main plasma

Plasma parameter	*Diagnostics*
Ion Temperature, Ion Density	Charge Exchange Recombination Spectroscopy
Electron Density	Thomson Scattering for Ruby Laser, Thomson Scattering for YAG Laser, CO_2 Laser Interferometer, FIR Laser Interferometer U1, U2 port
Electron Temperature	Thomson Scattering for Ruby Laser, Thomson Scattering for YAG Laser, Electron Cyclotorn Emission Diagnostic System
Plasma Current Profile	Motional Stark Effect (MSE)
Radiation	Bolometer
Impurity	VUV spectrometer for main plasma, Grazing Incidence Monochromator, X-ray Crystral Spectrometer
Zeff (Effectove Charge)	Zeff (vertical Bremsstrahlung), Tangential Fiber Array for Zeff
Magnetic Fluctuations	Saddle Coil, Tangential Probes for MHD analysis

Divertor plasma and Scrape-off layer (SOL)

Plasma parameter	*Diagnostics*
Ion Temperature	VUV Doppler Broadening
Electron Density	Reciprocating Probe at Midplane and Divertor Region, Target Langmuir Probe Array
Electron Temperature	Reciprocating Probe at Divertor Region, Target Langmuir Probe Array
Impurity	VUV spectrometer for Divertor Plasma, 60ch Fiber Optics for Divertor, High Resolution Visible Spectrometer for Divertor, Visible Spectrometer for Divertor
Radiation	Bolometer
Neutral Gas Pressure	Neutral Gas Pressure Gauge, Fast Ionization Gauge
Heat Load On Divertor Plate	Infrared TV for Divertor Plate

ionization state	wave-length(nm)	configurations	terms	ionization potential	$\frac{P_{line}\ rad\,(neon)}{P_{total}\ rad\,(neon)}$
Ne IV	47.0	$2s^22p^3$-$2s2p^4$	$^2D^0$ - ^2D	97eV	0.052
	54.4	$2s^22p^3$-$2s2p^4$	g$^4S^0$ - ^4P		0.026
Ne V	36.6	$2s^22p^2$-$2s2p^3$	^1D - $^1P^0$	126eV	0.028
	41.6	$2s^22p^2$-$2s2p^3$	^1D - $^1D^0$		0.064
	57.2	$2s^22p^2$-$2s2p^3$	g$^3P^0$ - $^3D^0$		0.037
Ne VI	40.1	$2s^22p$-$2s2p^2$	g$^2P^0$ - ^2P	158eV	0.082
	45.4	$2s2p^2$-$2p^3$	^4P - $^4S^0$		0.020
Ne VII	46.5	$2s^2$-$2s2p$	g^1S - $^1P^0$	207eV	0.13
	55.9	$2s2p$-$2p^2$	$^3P^0$ - ^3P		0.051
Ne VIII	77.0	$1s^22s$-$1s^22p$	g^2S - $^2P^0$	239eV	0.026

Table 5-(a). The lines from neon ion, transition, ionization potential and the contribution of the line radiation power to the total neon radiation power.

	Banana (proton)	Plateau (proton)	Pfirsch-Schluter (proton)
Banana (impurity)	$D_I=D_I^{BB}$ $-0.5<H<-0.2$	——	——
Plateau (impurity)	$D_I=D_I^{BP}$ $0<H<+1.5$	$DI=D_I^{BP}$ $H=+1.5$	——
Pfirsh-Schluter (impurity)	$D_I=D_I^{PS+class}$ $H=-0.5$	$D_I=D_I^{PS+class}$ $H=-0.5$	$D_I=D_I^{PS+class}$ $-0.5<H\leqq 0$

Table 6-a: D_I is the diffusion coefficient and H is a coefficient given in ref. [98,99].

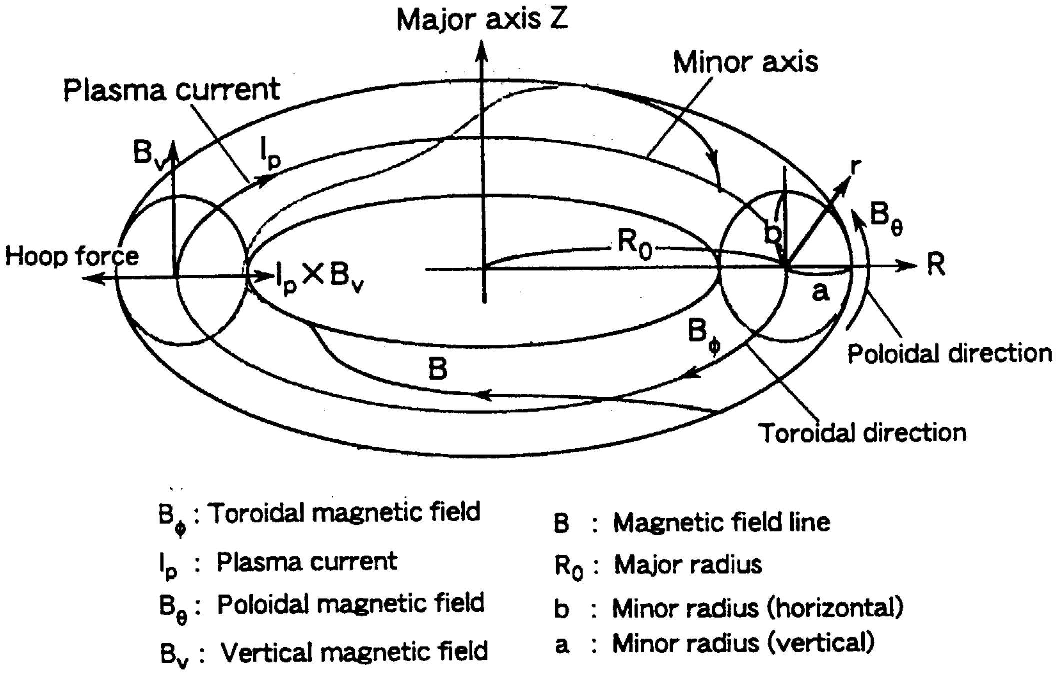

Figure 2-1: Toroidal geometry of the tokamak and coordinate system

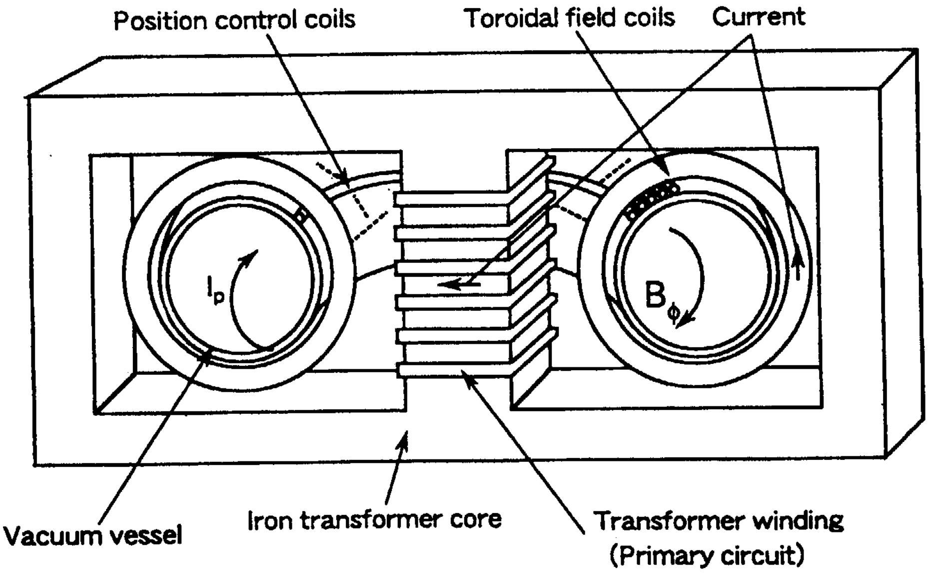

Figure 2-2: Schematic of the tokamak configuration

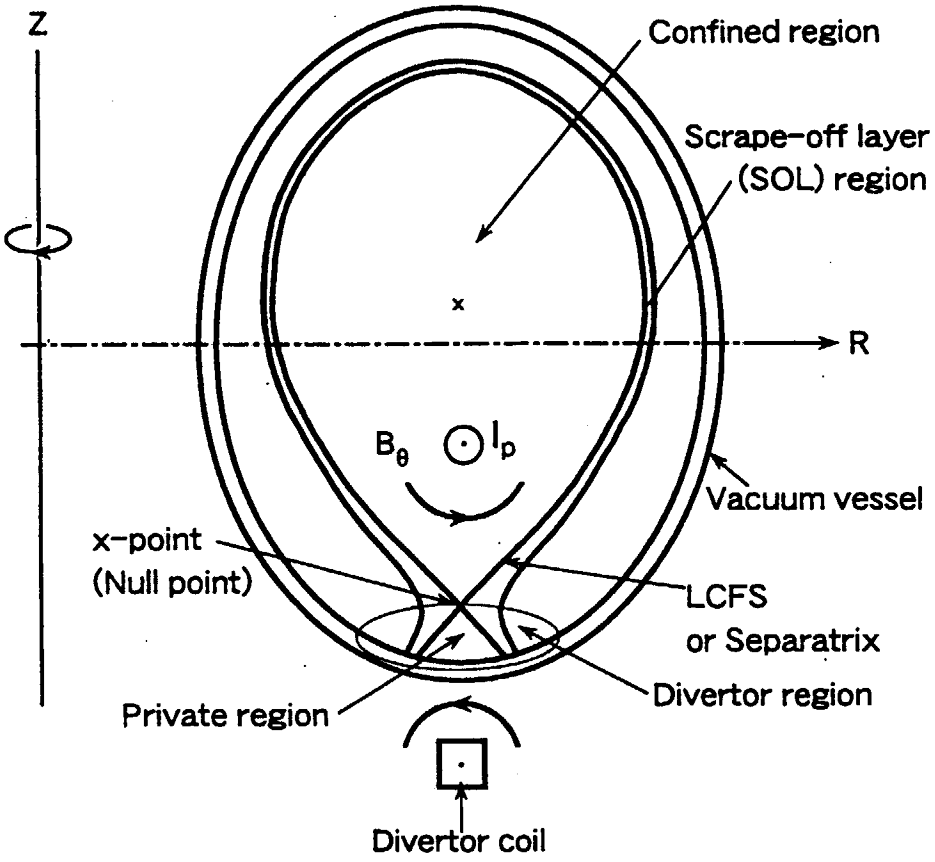

Figure 2-3: Tokamak configuration with the divertor. The divertor configuration is produced by the divertor coil with the current flowing to the same direction in the plasma current.

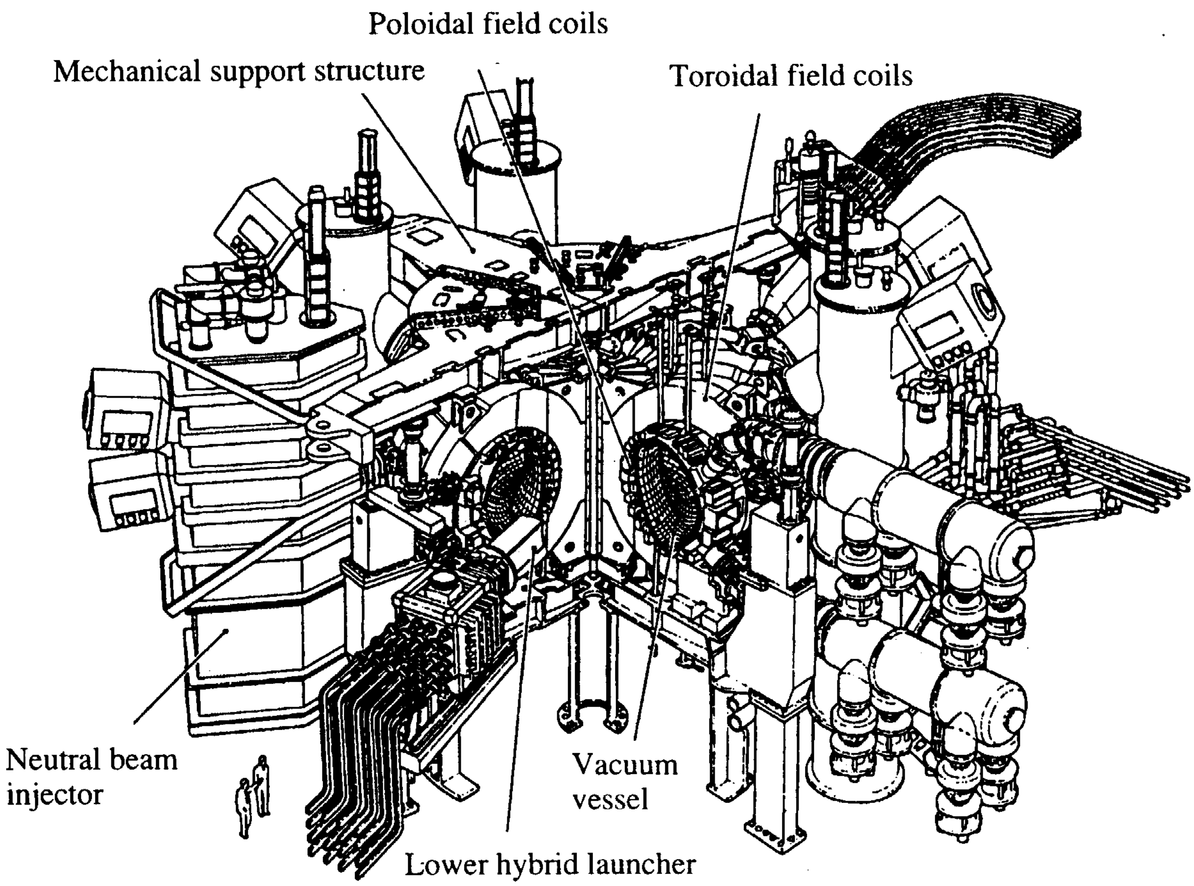

Figure 2-4: An overall schematic of the JT-60U

(a) Open Divertor

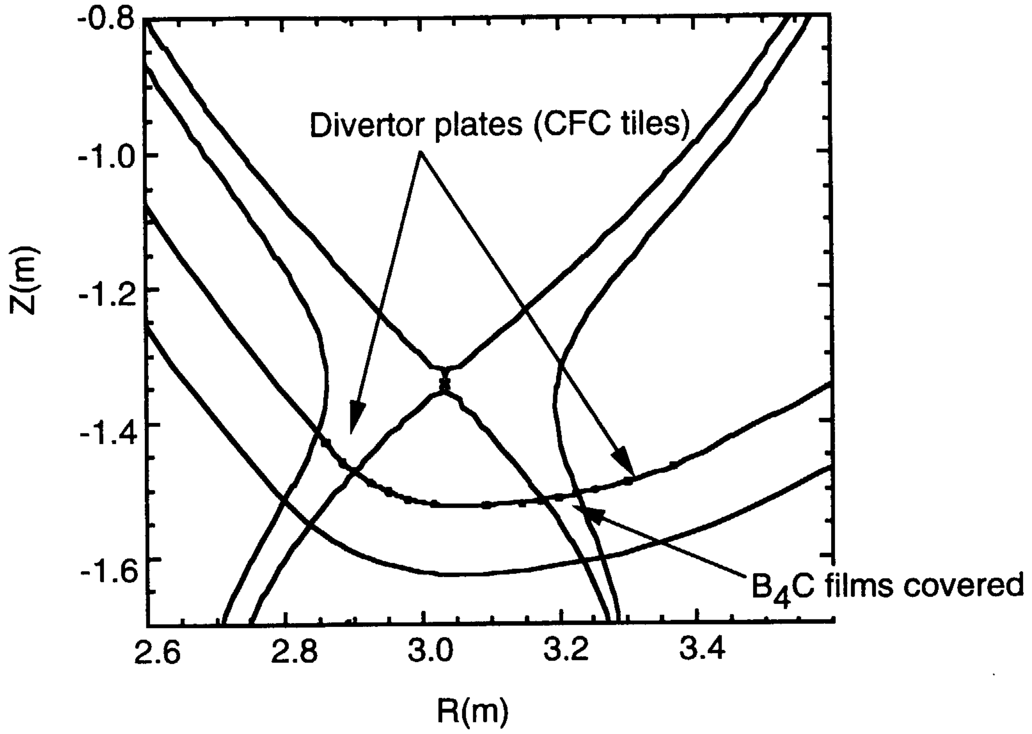

(b) W-shaped Divertor

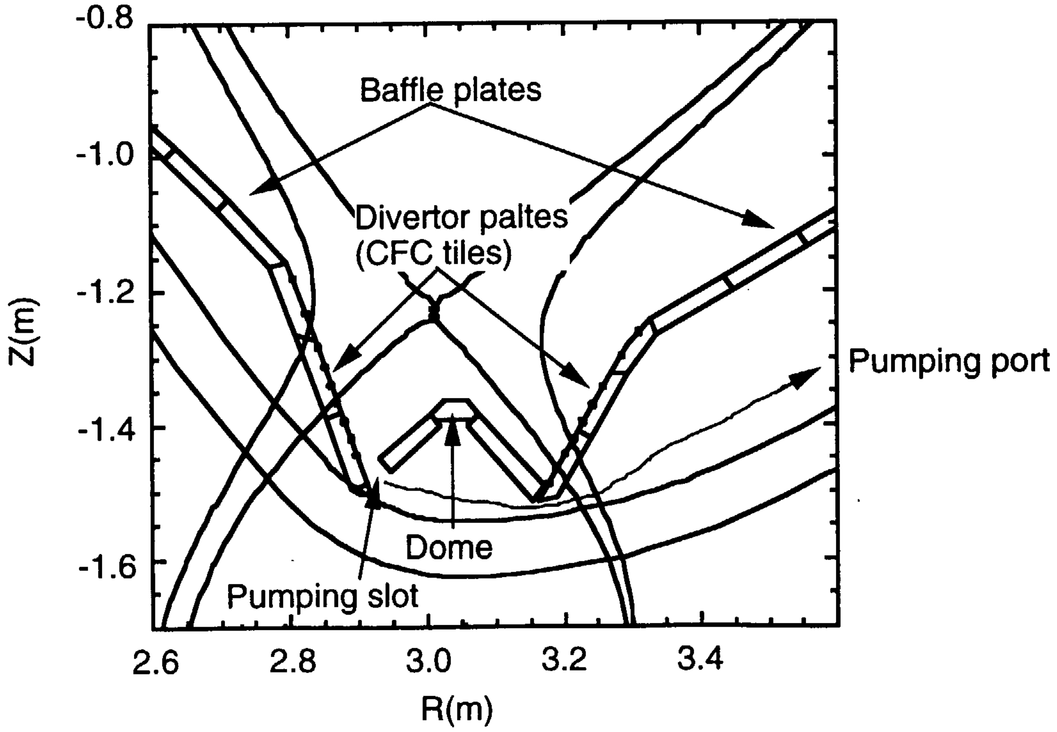

Figure 2-5: The poloidal cross-section of (a) the open divertor and (b) the W-shaped divertor

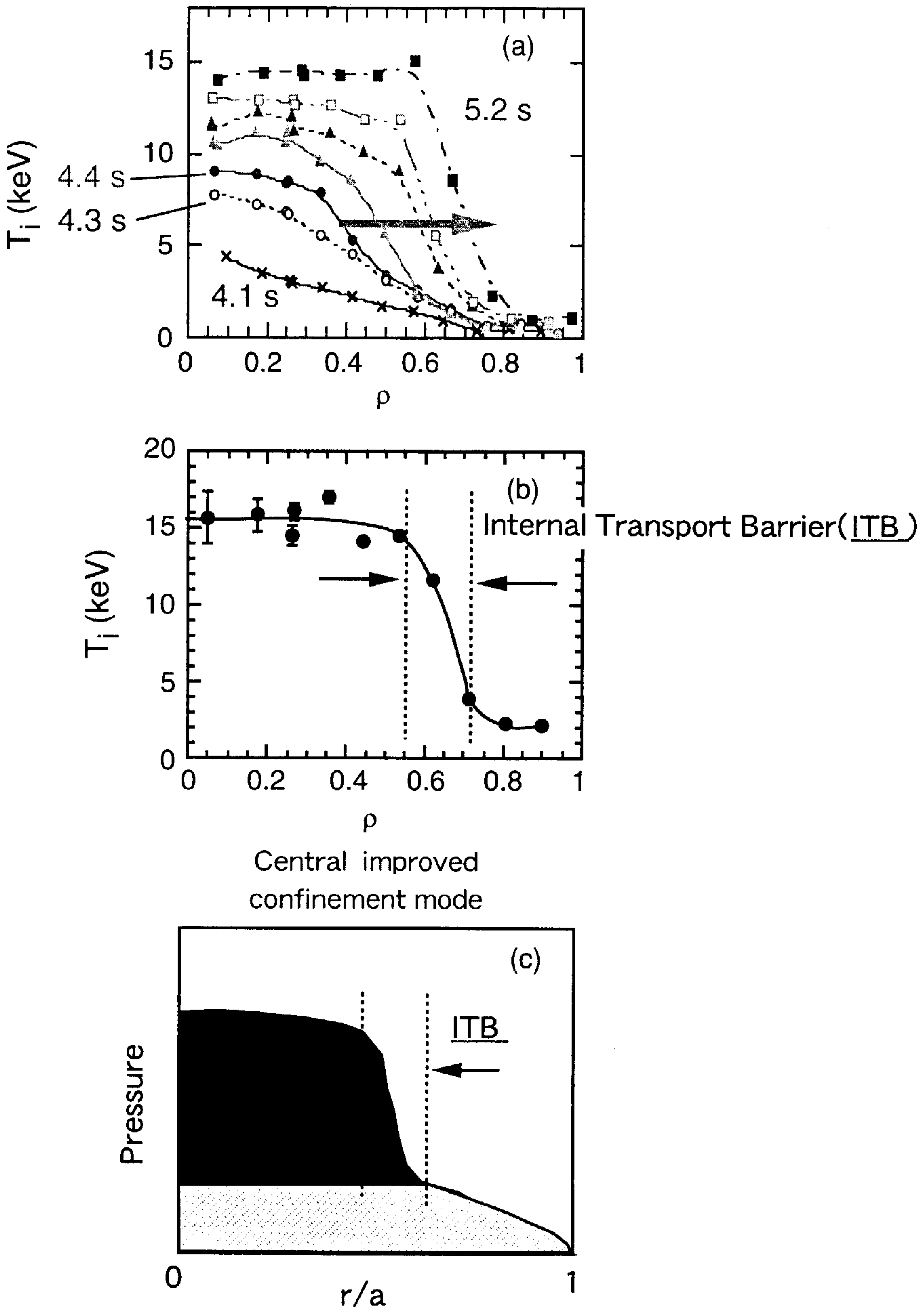

Figure 2-6 (a) Time evolution of ITB

(b) A steepen gradient of ion temperature is shown around ρ ~0.65(m)

(c) Pressure distribution with ITB in central improved confinement mode

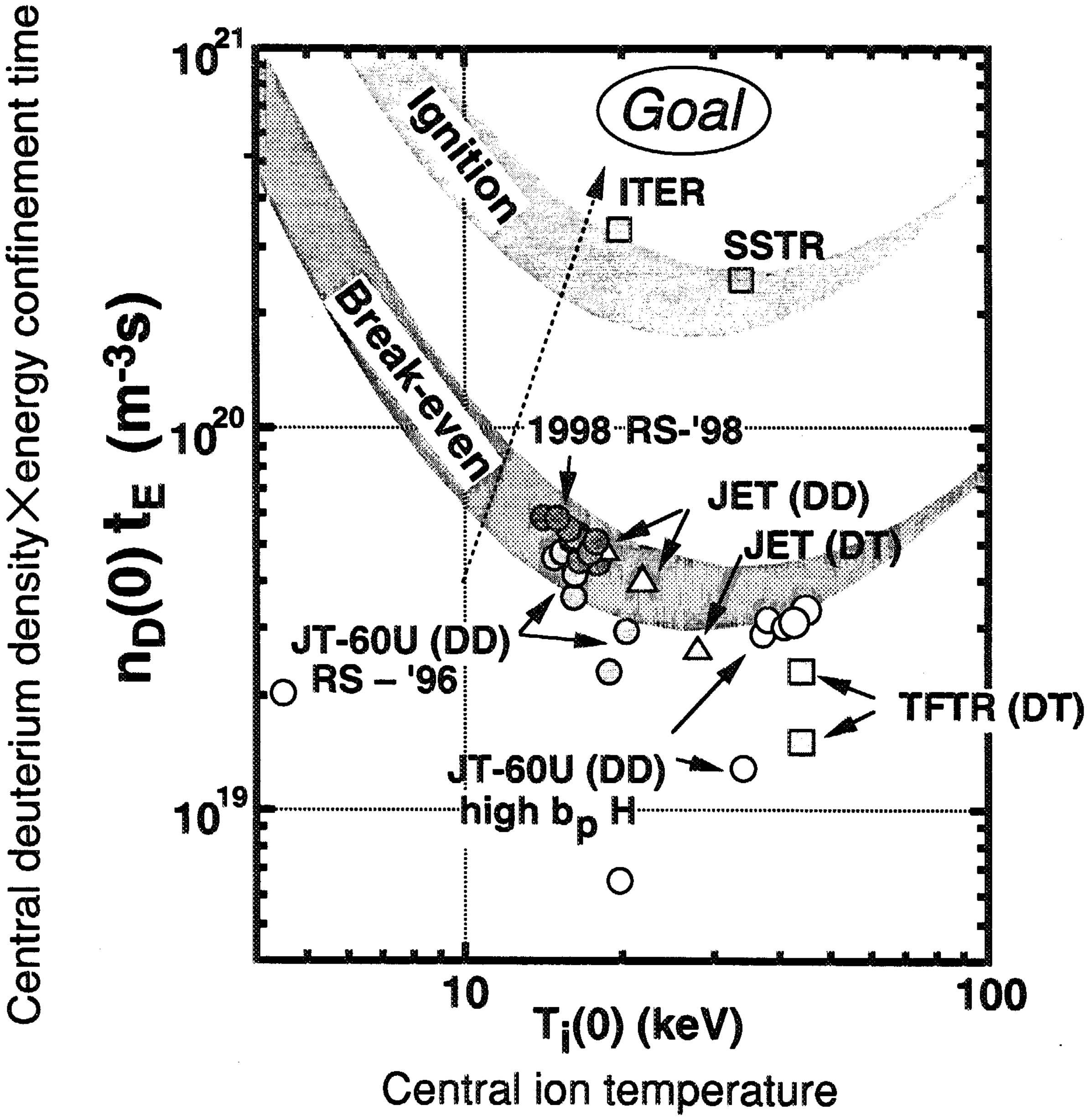

Fig. 2-7 Lawson diagram of JT-60U and other machine experiments. $Q_{DT}^{eq} = 1.25$ was achieved in JT-60U reversed shear plasma in 1998.

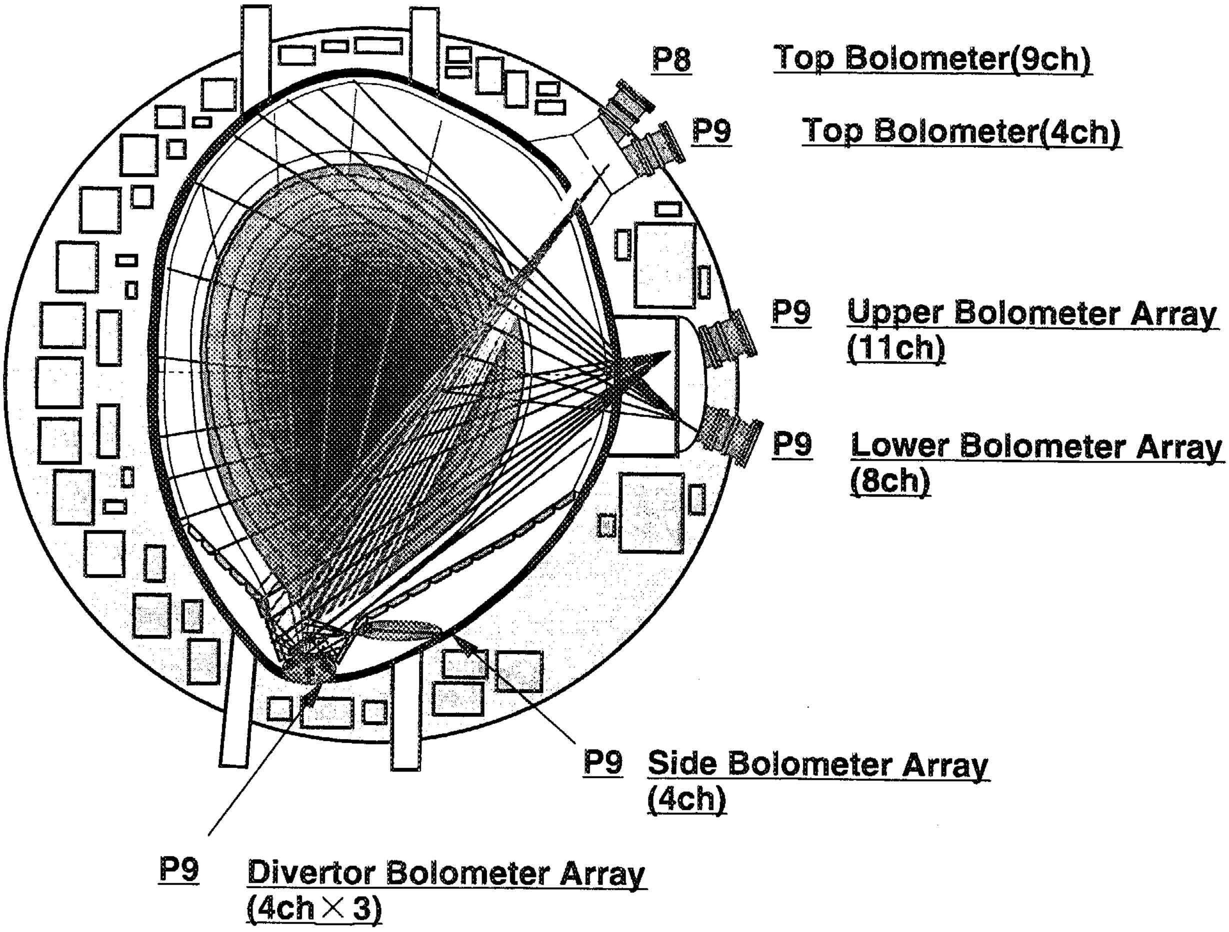

Figure 2-8: Viewing chords of bolometer array

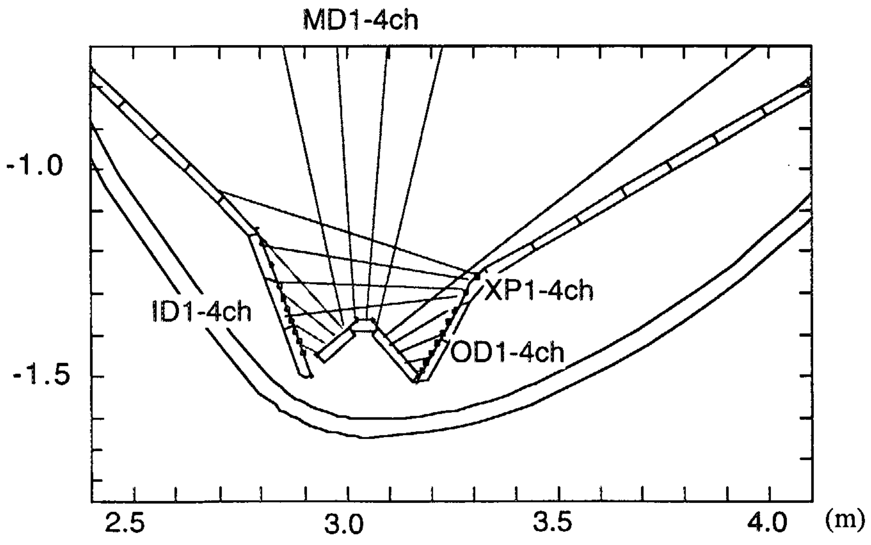

Figure 2-9: Viewing chords of PTS bolometer in the divertor region

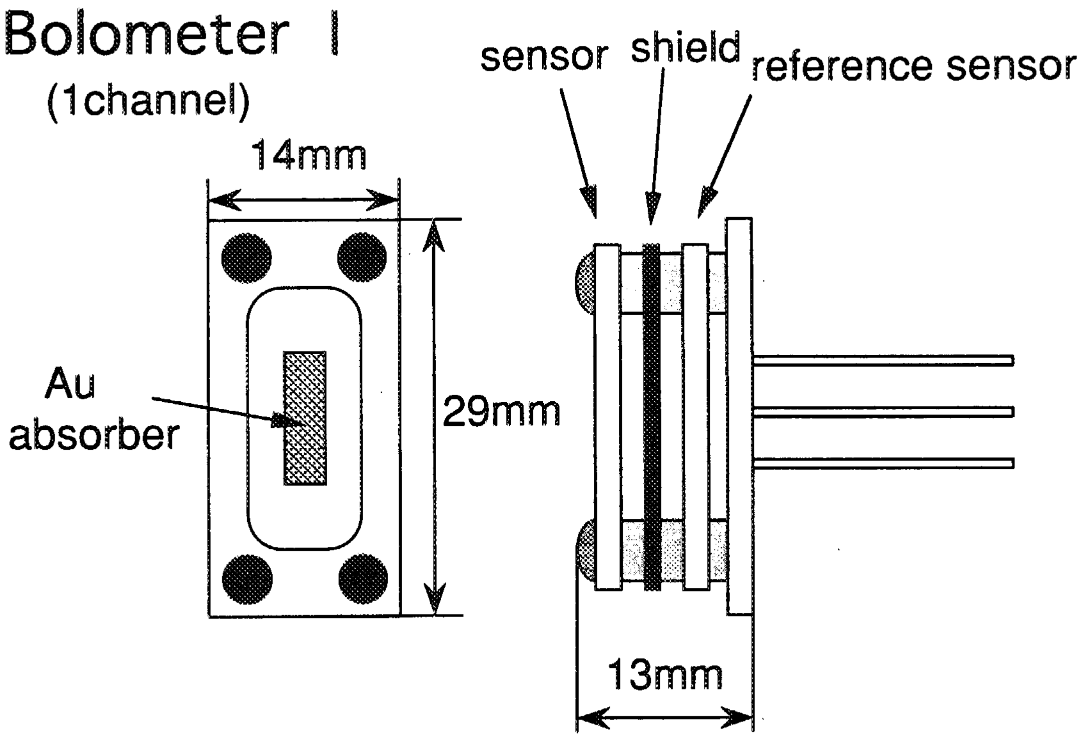

Bolometer Ⅰ
(1channel)

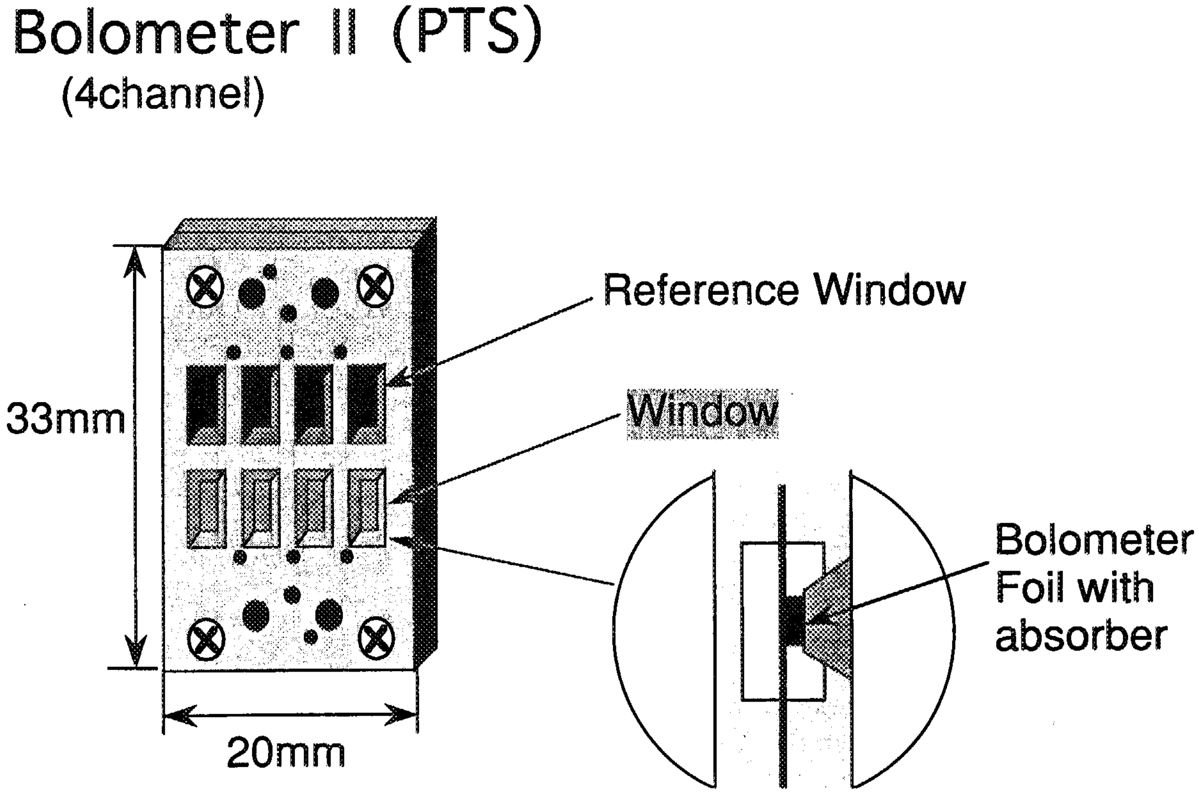

Bolometer Ⅱ (PTS)
(4channel)

Figure 2-10 Detailed view of bolometer head

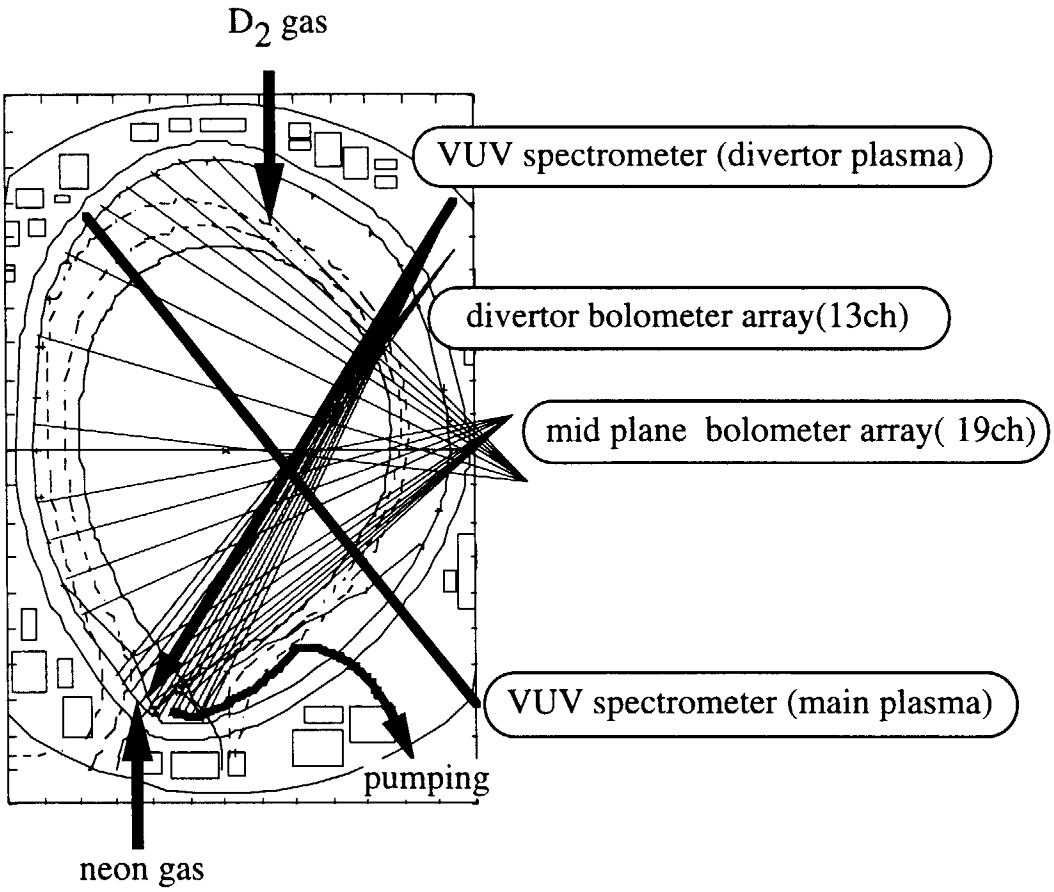

Fig.2-11A schematic diagram of the viewing chords of the diagnostics for the radiation investigation.

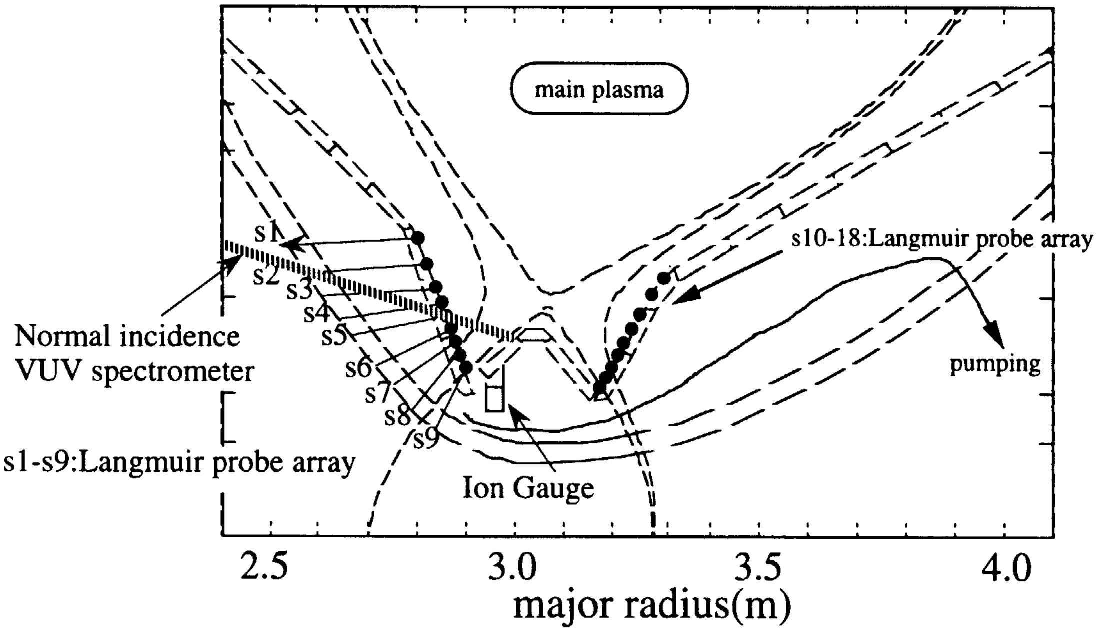

Fig.2-12 An expanded view of the divertor measurements.

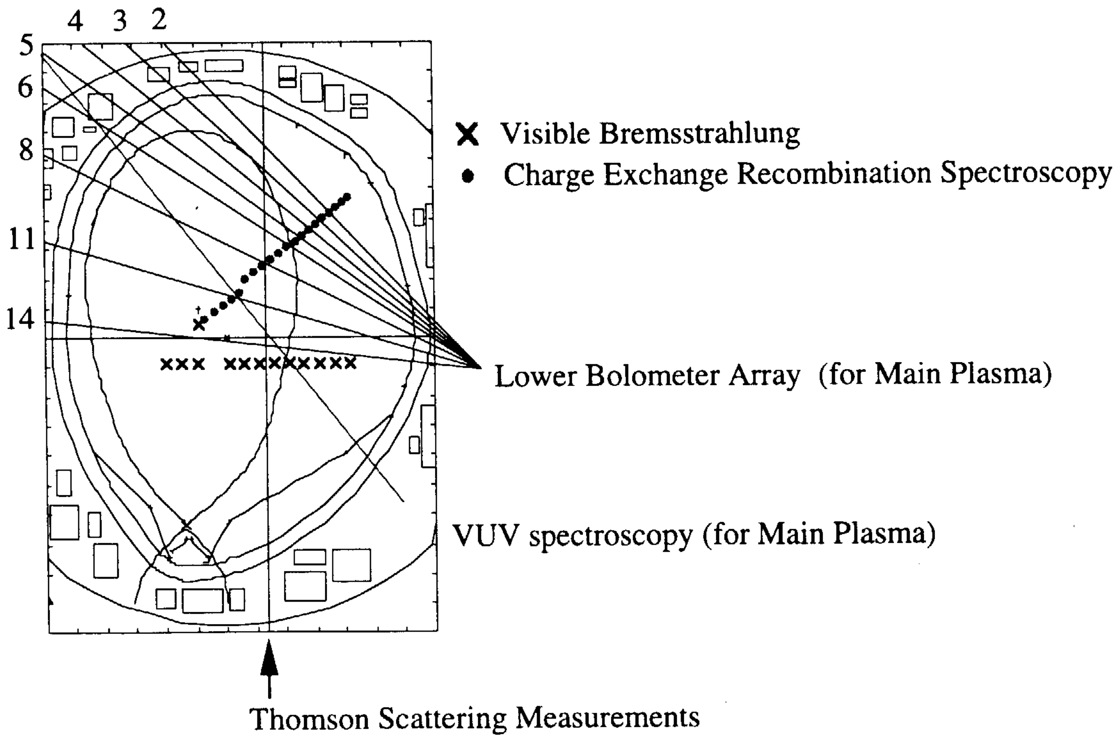

Fig. 2-13 Schematic view of the diagnostic viewing chords and measurement points of JT-60U. Closed circle shows measured points of charge exchange recombination spectroscopy on the projected poloidal plane. Crossed symbol shows measurement points of visible bremsstrahlung on the projected poloidal plane.

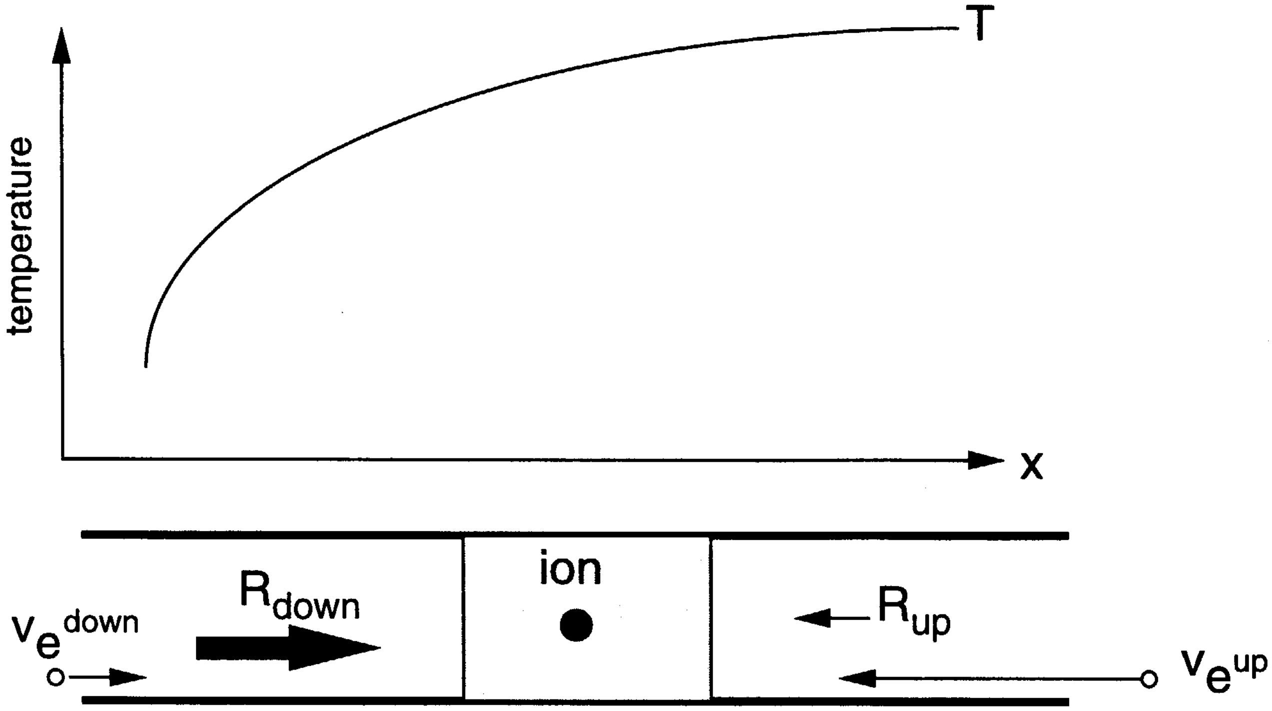

$$v_e^{down} < v_e^{up}$$

$$\tau \propto v^3$$

$$\text{Force} \propto \frac{mnv}{\tau} \propto \frac{mn}{T}$$

$$\therefore R_{down} > R_{up}$$

Fig. 3-1 Figure for simple explanation of thermal force. The force from downstream electrons is stronger than the force from upstream electrons.

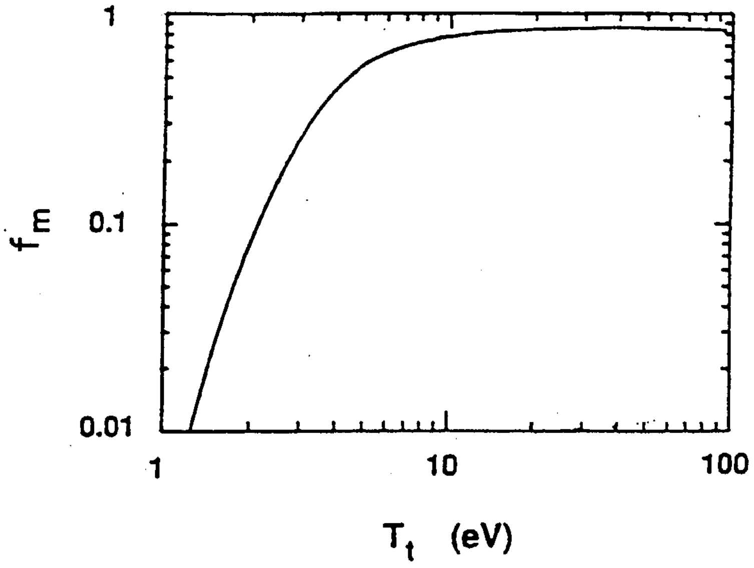

Figure 3-2: Momentum loss factor f_m to the temperature on the target

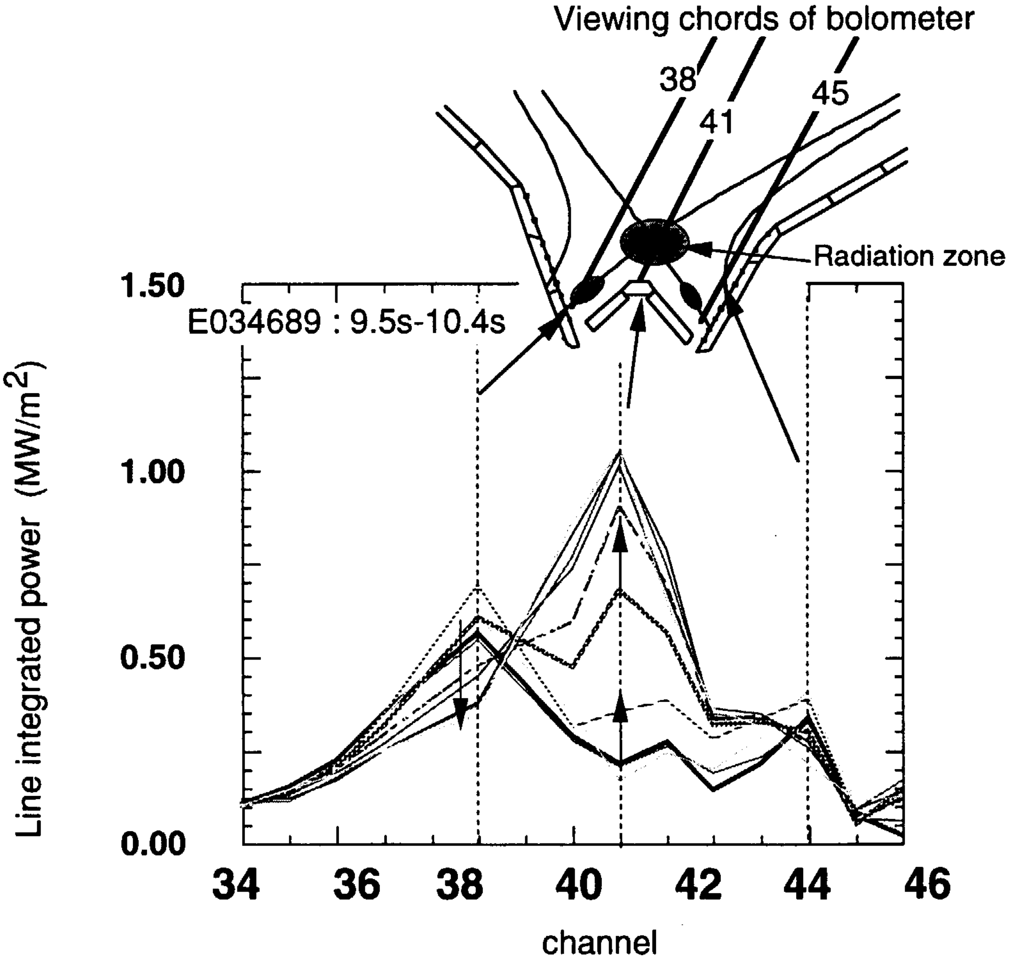

Figure 3-3: Time evolution of the MARFE (radiation zone) in the case of the ion ∇B drift toward the x-point. Each profile is drawn every 0.1s interval.

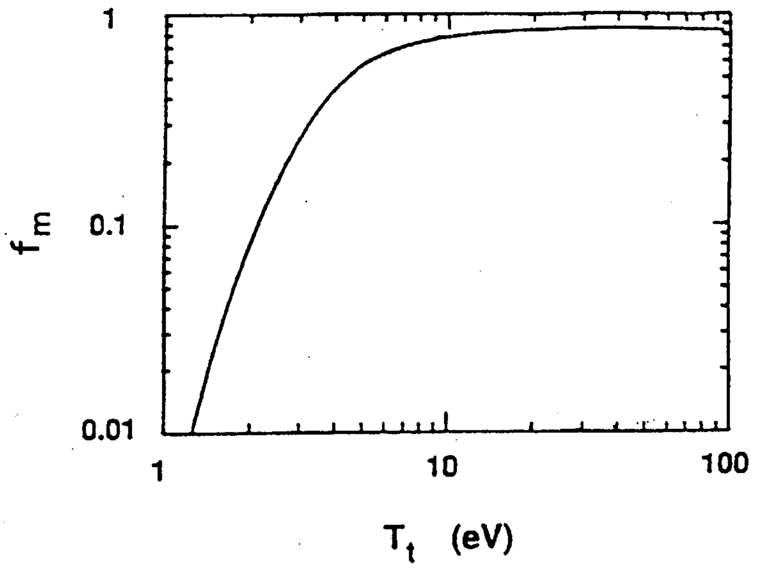

Figure 3-2: Momentum loss factor f_m to the temperature on the target

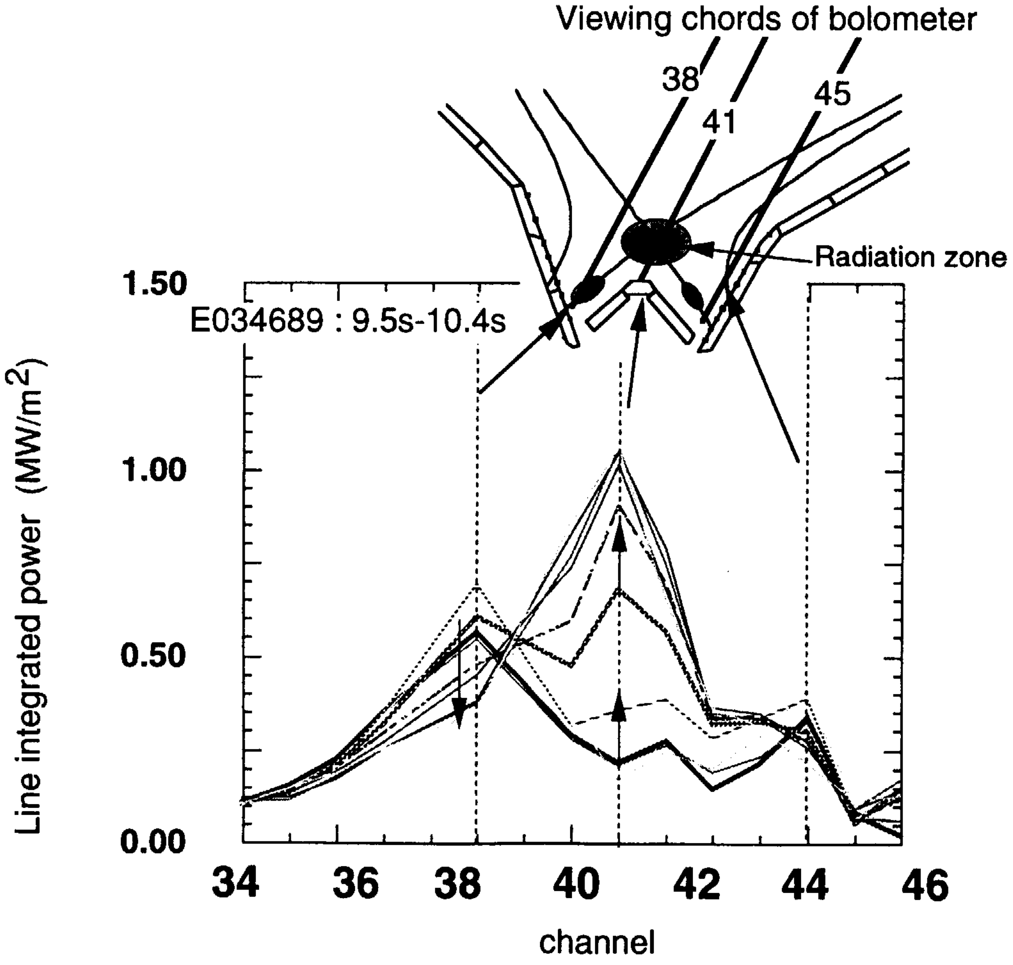

Figure 3-3: Time evolution of the MARFE (radiation zone) in the case of the ion ∇B drift toward the x-point. Each profile is drawn every 0.1s interval.

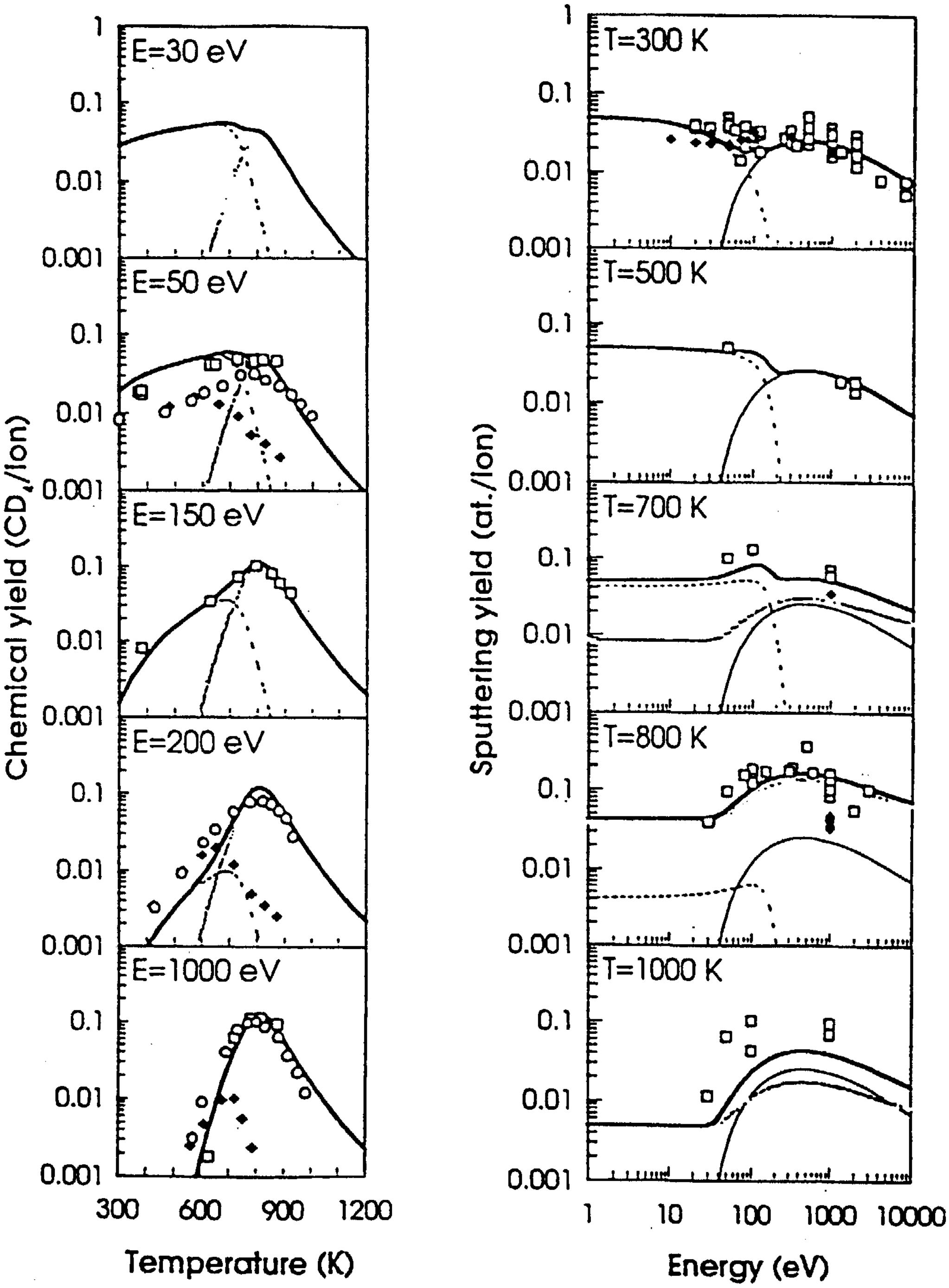

Temperature dependence of the chemical sputtering yield at different ion energies. □,O: exp. data for C; ♦: exp. data for C+15%B. ······ $Y_{ch,th}$; ---- $Y_{ch,ath}$; ━━ $Y_{ch,th}+Y_{ch,ath}$.

Energy dependence of the total sputtering yield at different target temperatures. □,O: exp. data for C; ♦: exp. data for C+15%B. — Y_{phys}; ······ $Y_{ch,th}$; ---- $Y_{ch,ath}$; ━━ $Y_{phys}+Y_{ch,th}+Y_{ch,ath}$.

Figure 4-1: Energy and temperature dependence of the sputtering yield for normal incidence.

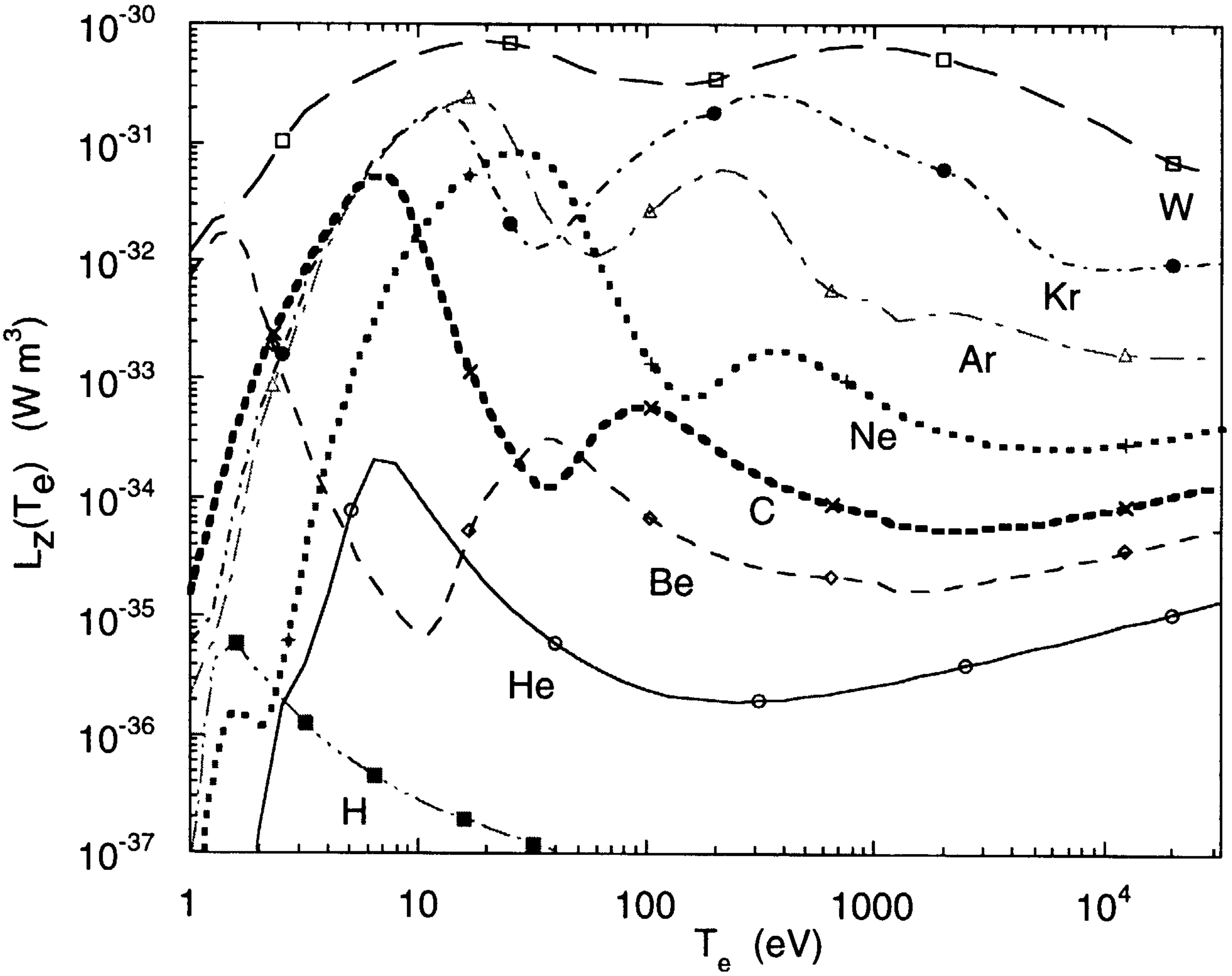

Figure 4-2: Impurity radiation loss rate coefficients for common edge impurities together with the hydrogen rate. Rates from ADPAK[56] and LANL / ADPAK [5 7. Low-Te range calculated with detailed code [58], high-Te portion (>1000eV) calculated with ADPAK; see [57].

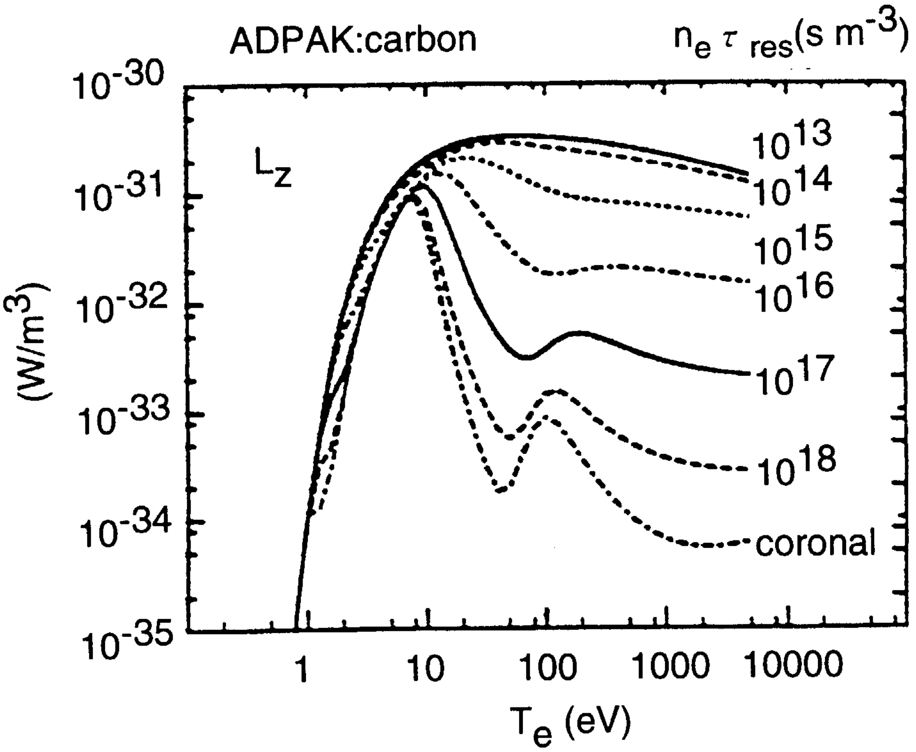

Figure 4-3: Radiated power coefficient L_Z for carbon as a function of electron temperature T_e for different values of residence parameter $n_e \tau_{res}$.

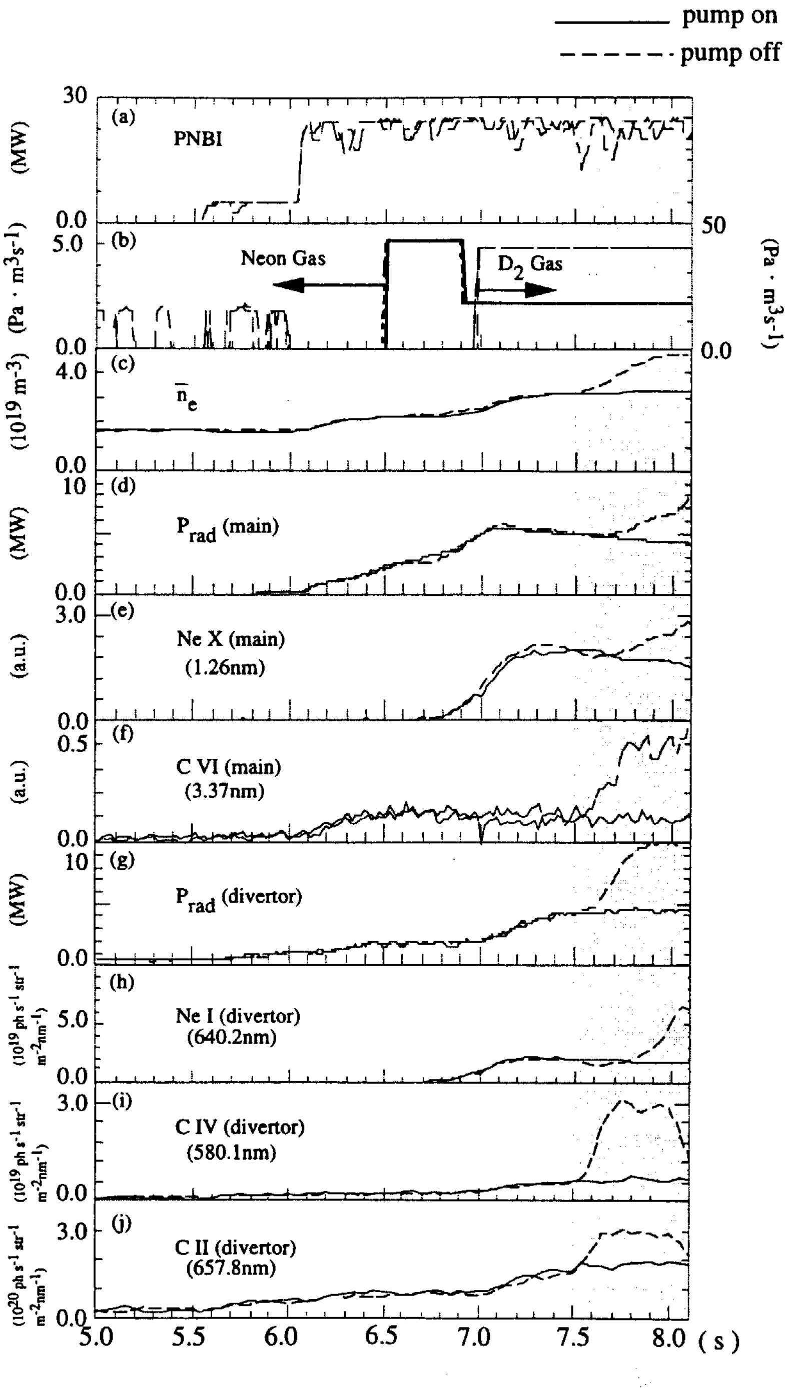

MARFE
(in the case of pumping-off)

Fig.5-1 Time evolution of plasma discharge parameters for the neon gas puff experiment; (a) total neutral beam power (b) neon gas puff to the divertor and D_2 gas puff to the main plasma (c) line averaged electron density (d) radiation in the main plasma (e) Ne X (f) C VI intensity in the main plasma (g) radiation in the whole divertor region (h) Ne I (i) C II (j) C IV intensity in the divertor plasma with pump on (solid lines) and pump off (dotted lines). MARFE occurs at 7.5s in the case of pump off (shadow region).

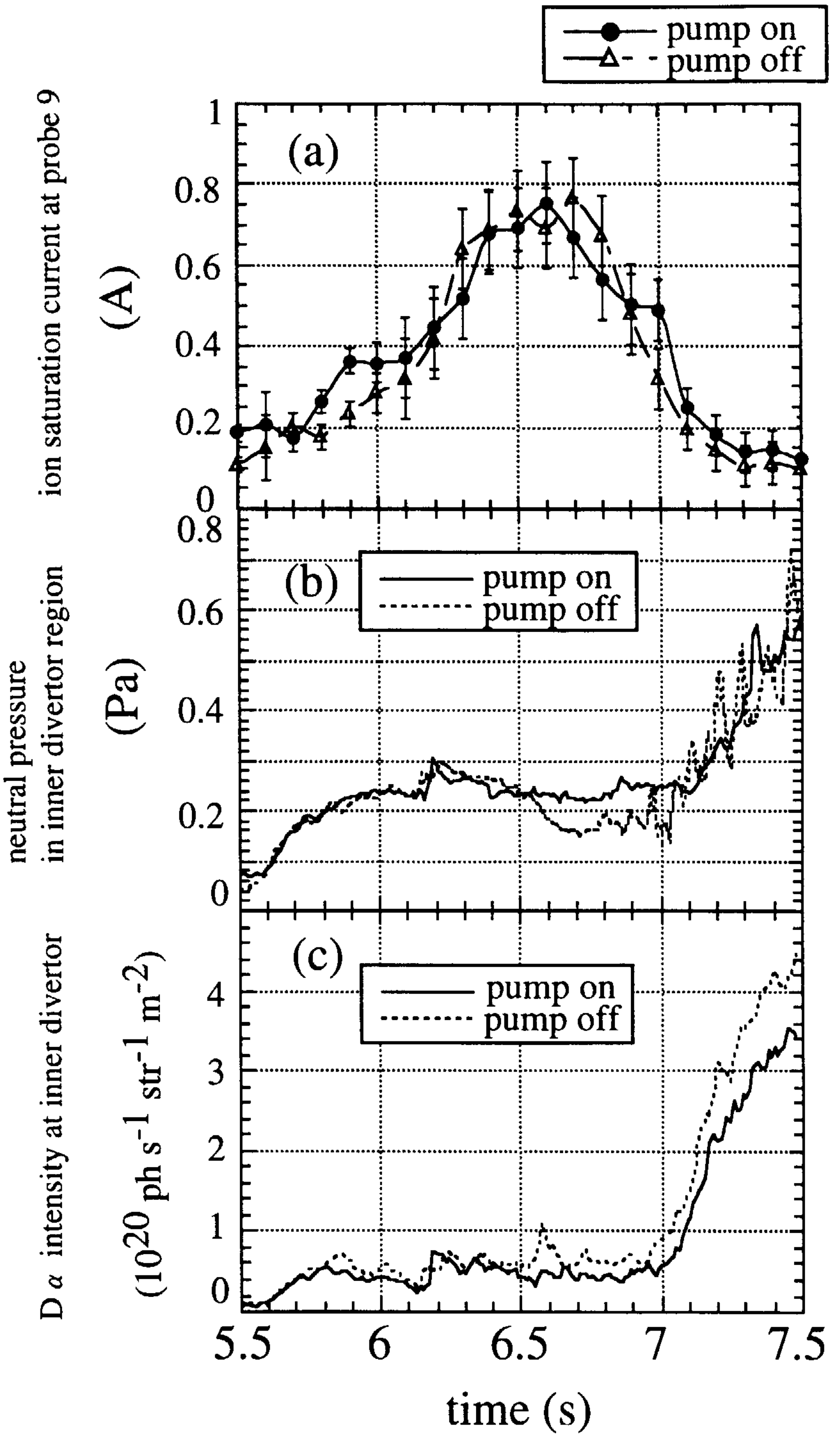

Fig.5-2 Time evolution of (a)ion saturation current(probe: s9), (b)inside divertor pressure, (c) D α intensity at inner strike point.; with pump on(solid lines) and pump off (dotted lines).

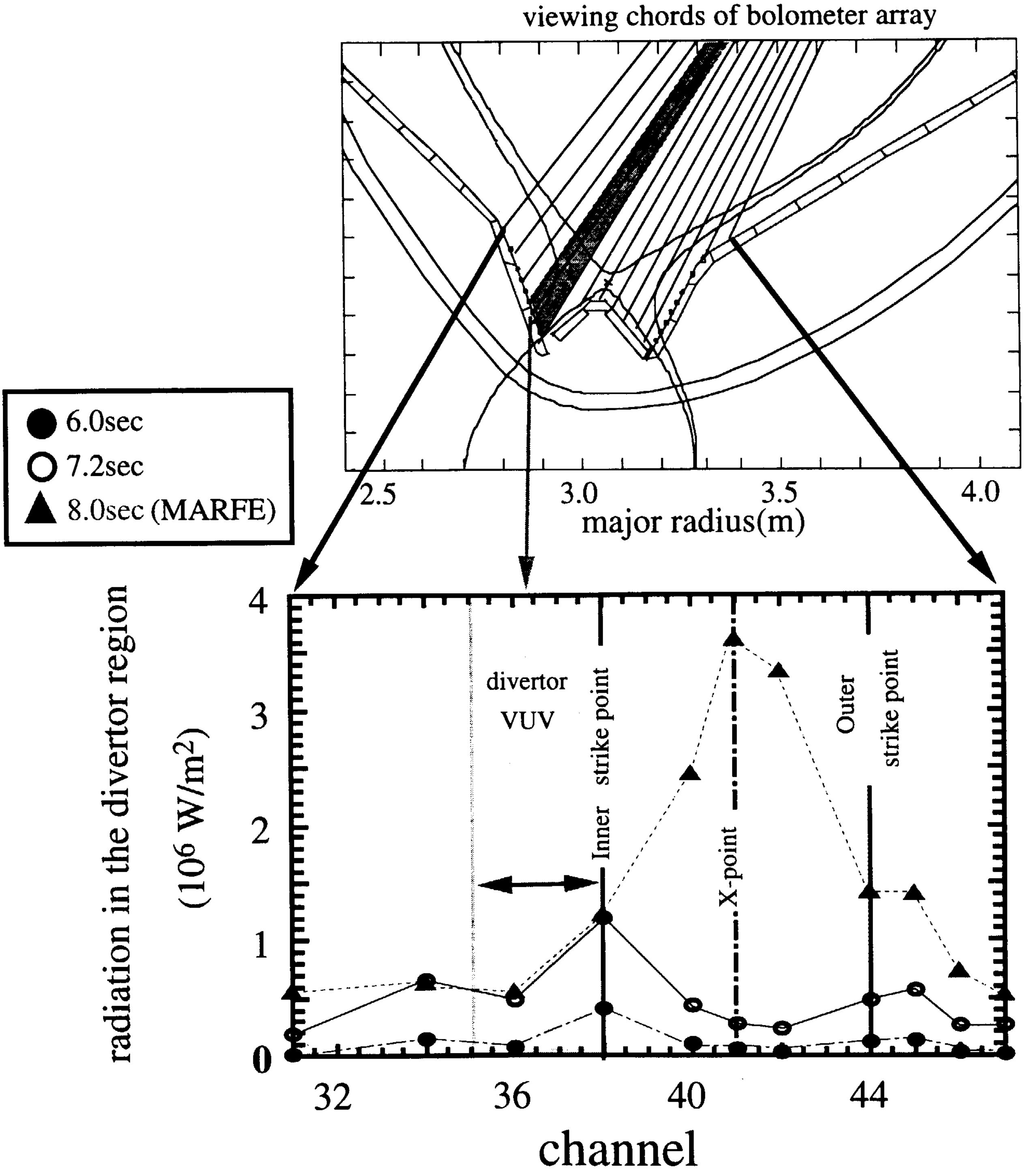

Fig.5-3 The radiation profile in the divertor plasma; 6.0 s (closed circles), 7.2s (open circles), 8.0 s(closed triangle/ MARFE).

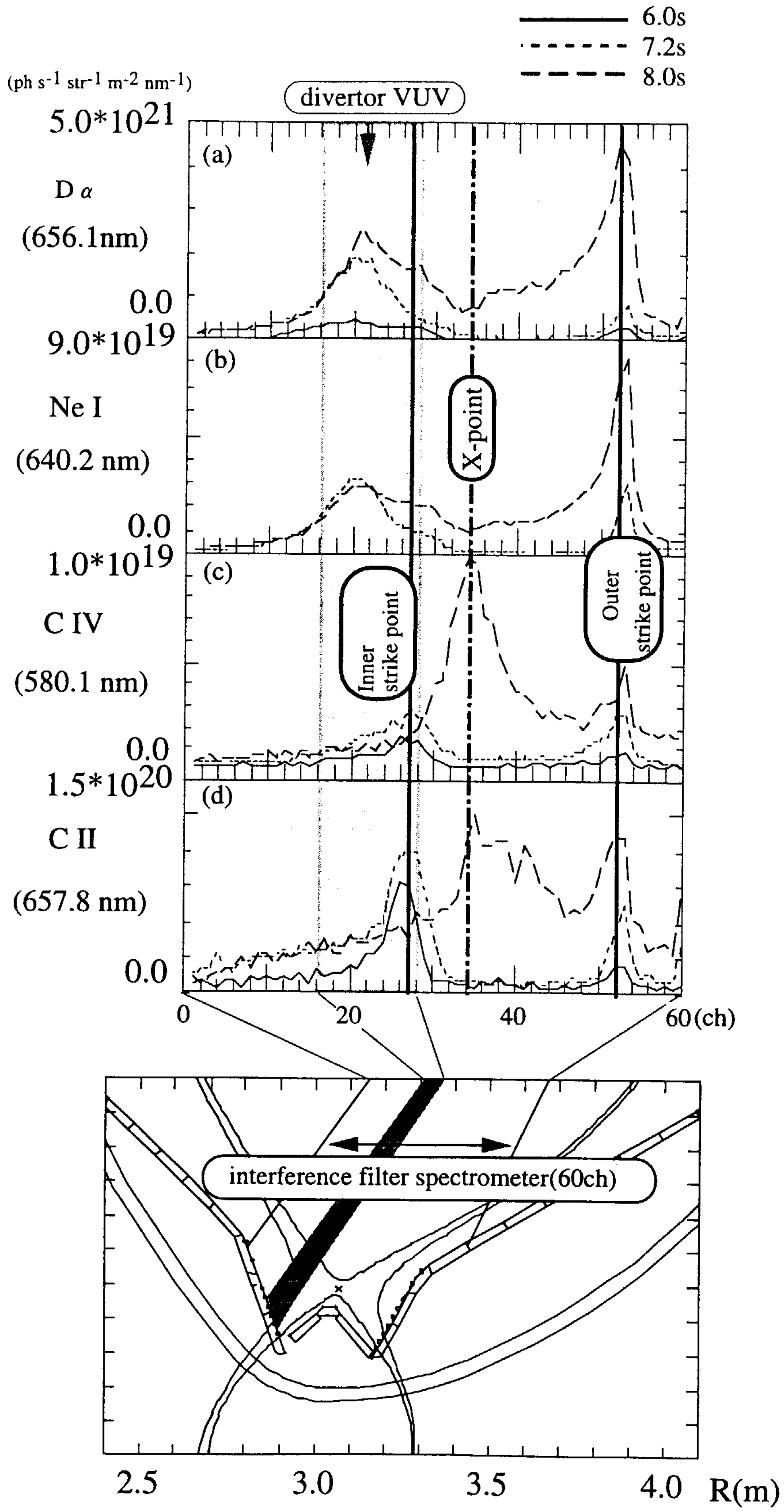

Fig.5-4 The spatial distribution of line intensity profiles in the divertor plasma at 6.0 s, 7.2 s, 8.0 s (MARFE); (a) D I (656.1 nm) (b) Ne I (640.2 nm) (c) C IV (580.1 nm) (d) C II (657.8 nm).

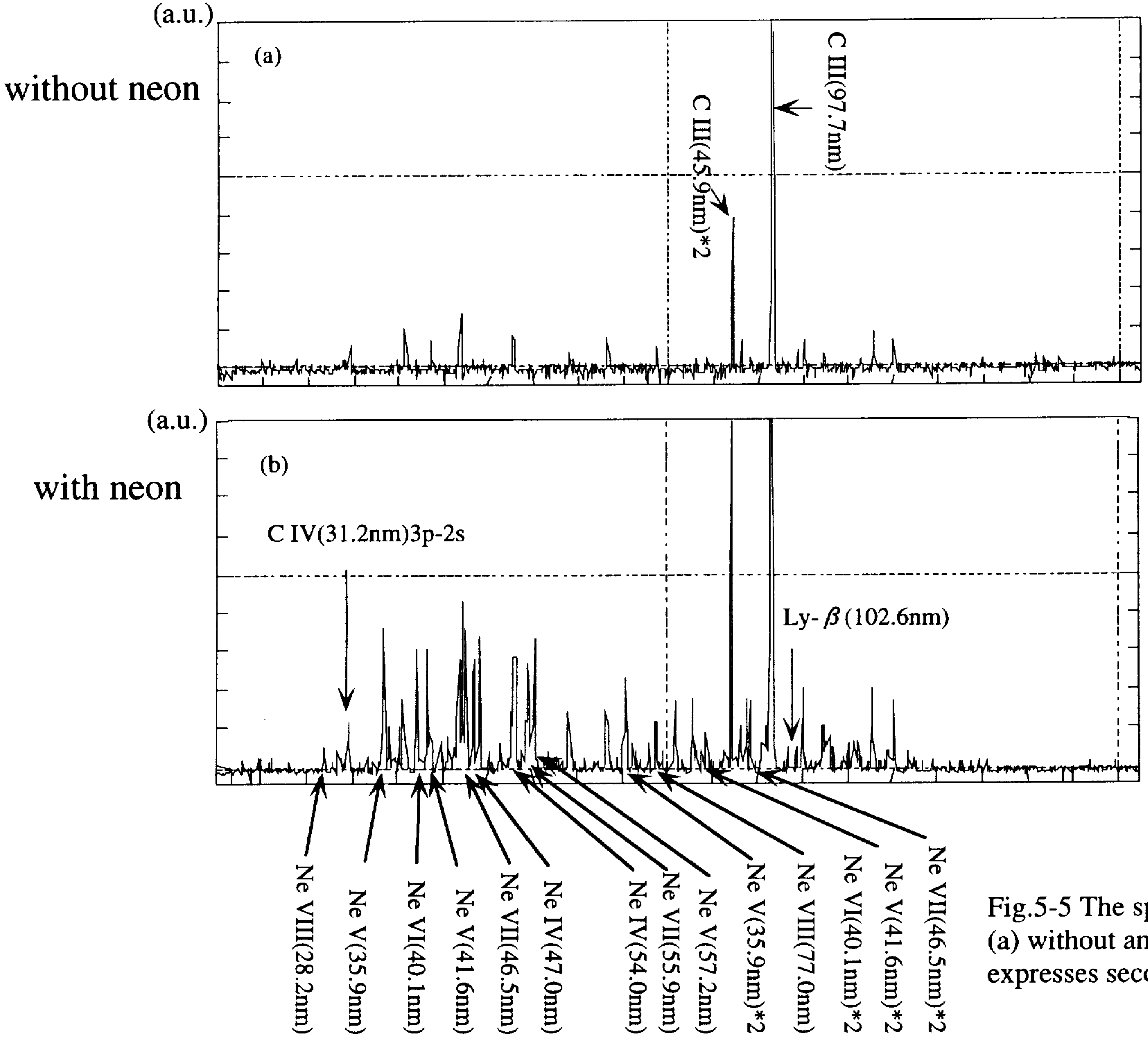

Fig.5-5 The spectral lines in the VUV range (a) without and (b) with neon gas. The "*2" expresses second order neon ion spectrum.

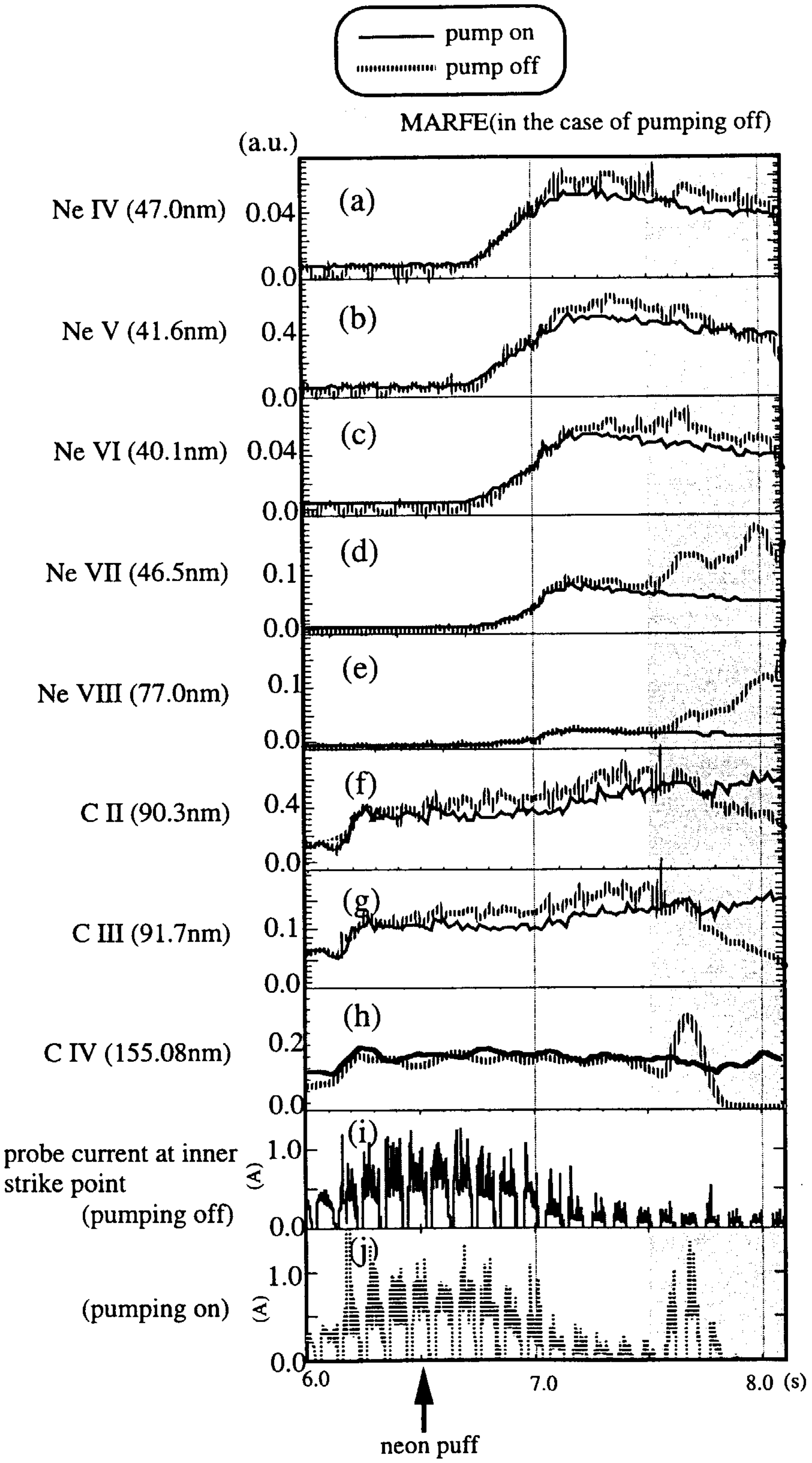

Fig.5-6 The time evolution of line intensities in the inner divertor; (a)Ne IV (47.0 nm), (b)Ne V (41.6 nm), (c)Ne VI (40.1 nm), (d)Ne VII (46.5 nm), (e) Ne VIII (77.0 nm), (f) C II (90.3 nm), (g) C III (91.7 nm), measured with divertor VUV spectrometer; C IV (155.08 nm) measured with normal incidence VUV spectrometer; (i)(j) show the probe current near the inner strike point(probe: s9).; with pump on(solid lines) and pump off(dotted lines). A shadow region shows the MARFE in the case of pumping off.

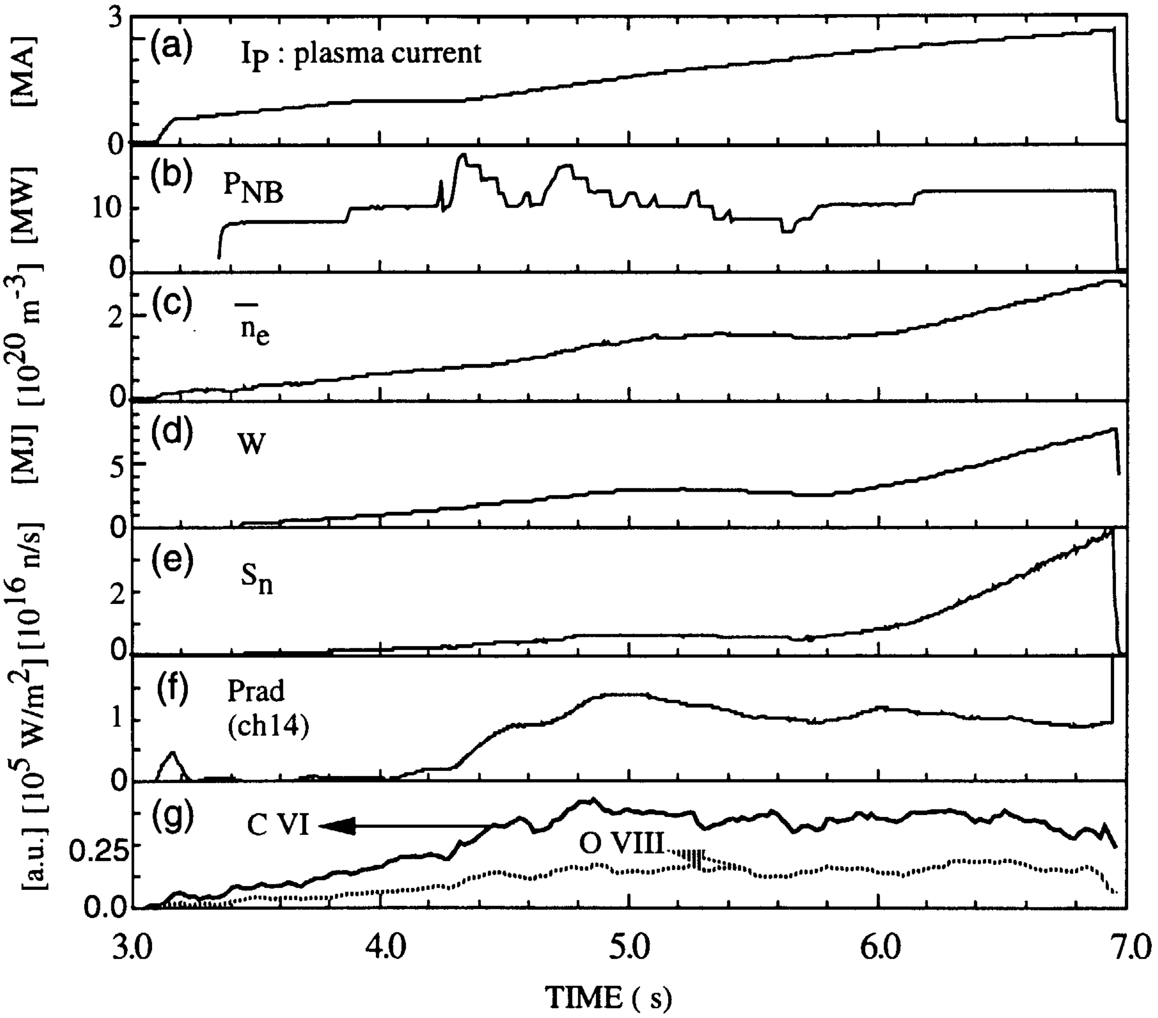

Fig. 6-1 time evolution of a reversed shear discharge
(a) plasma current
(b) total neutral beam power
(c) tangential line averaged electron density
(d) stored energy
(e) neutron counts
(f) main plasma radiation along the central chord(ch14)
(g)solid line is C VI(3.37nm) line intensity and dotted line is O VIII (1.9nm) line intensity

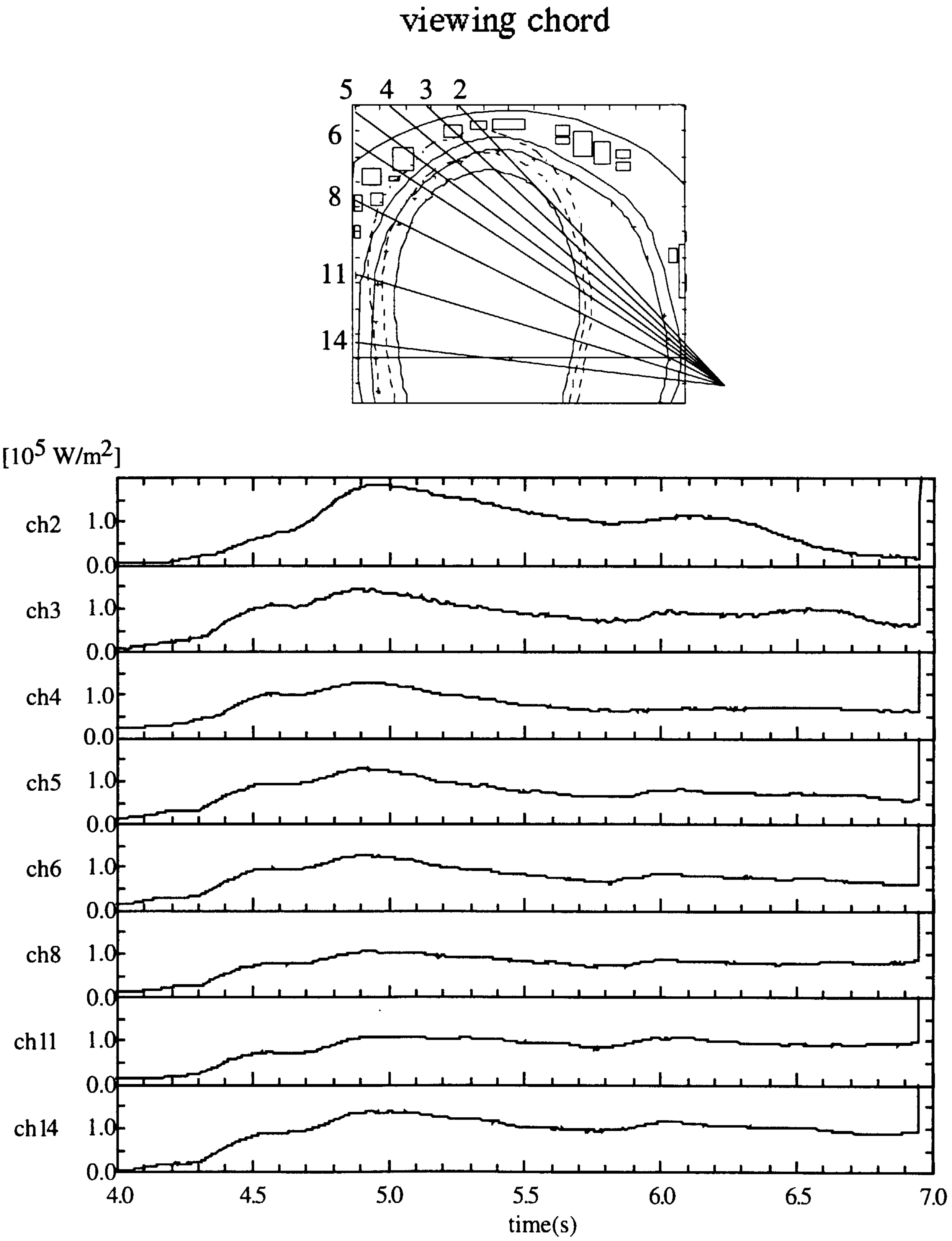

Fig. 6-2 Time evolution of each bolometer radiation and corresponded viewing chords

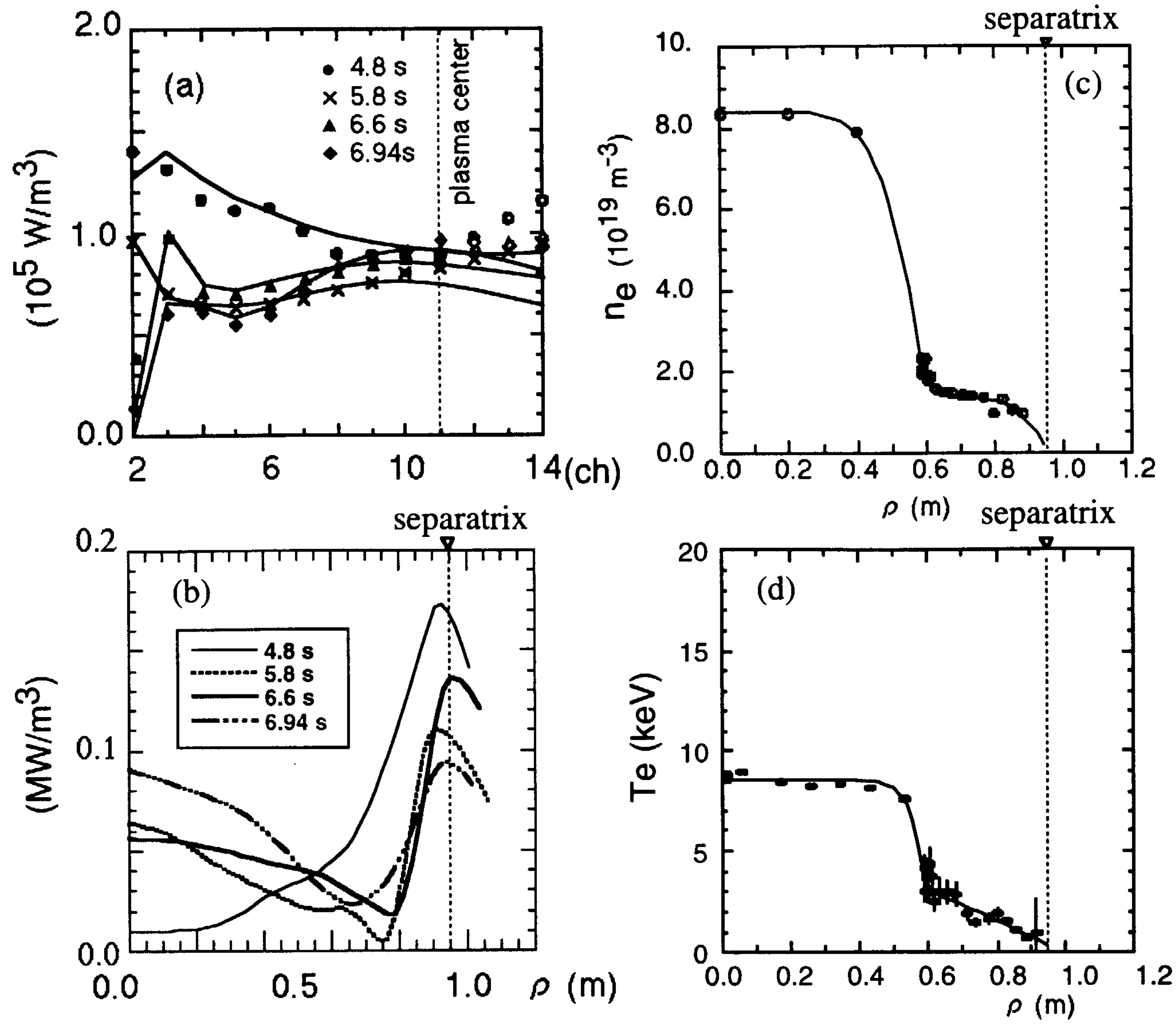

Fig. 6-3

(a) Circles are the line integral radiation of bolometer arrays. Closed circles indicate using by Able inversion and open circles indicates excluded data which are opposite side of plasma center. Solid lines are line integrations of Abel inverted radiation density. (b) volumetric radiation loss density obtained by Abel inversion (c) electron density (d) electron temperature.

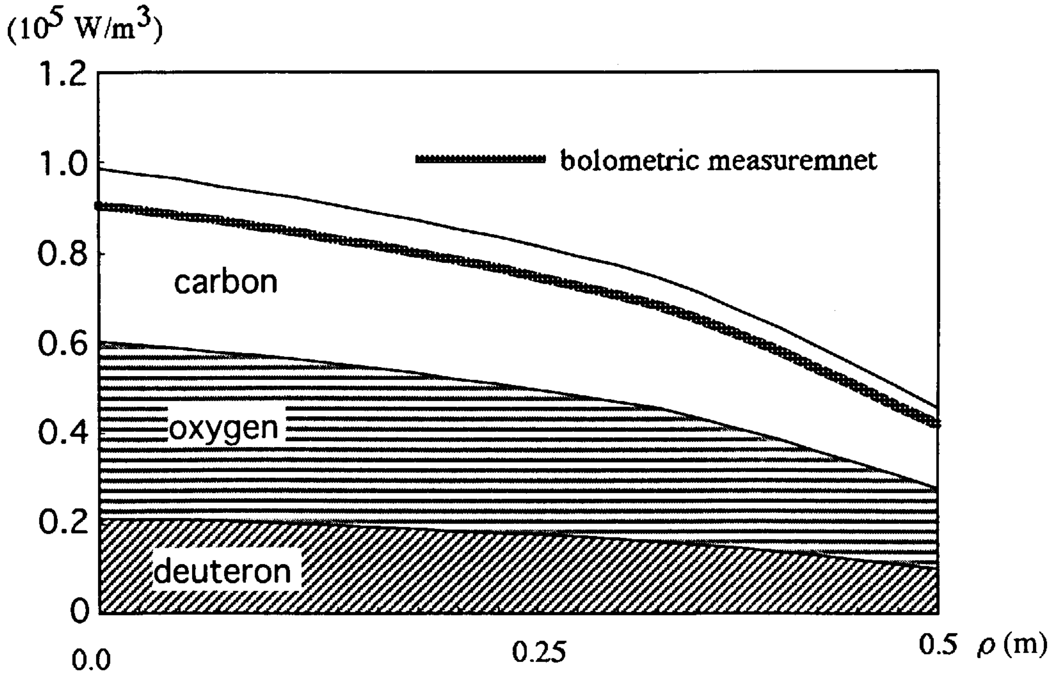

Fig.6-4
Contributions from impurity radiation in the core plasma ($\rho < 0.5$m). Each radiation power are estimated using cooling rates and thick solid line shows bolemetric measurement. The measured core radiation is 0.68 MW.

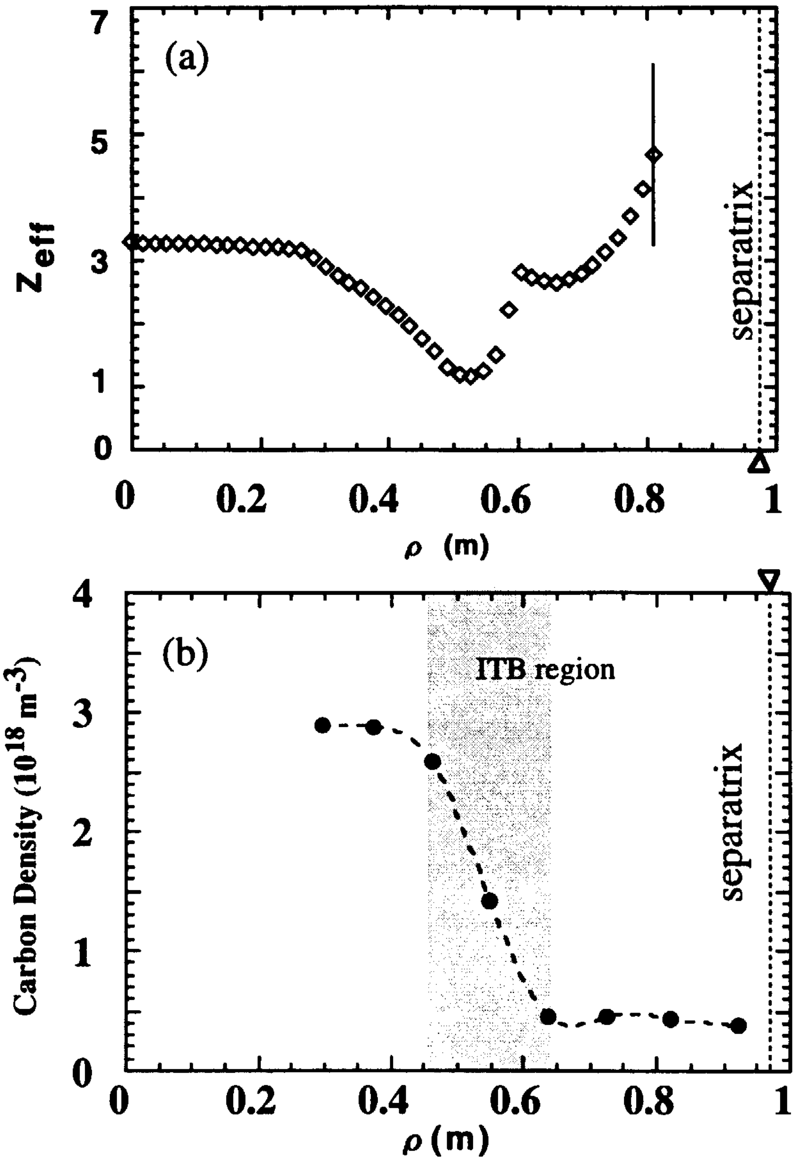

Fig.6-5
(a) Zeff profile from bremsstrahlung by abel inversion (b) Carbon density profile estimated from CXRS measurements.

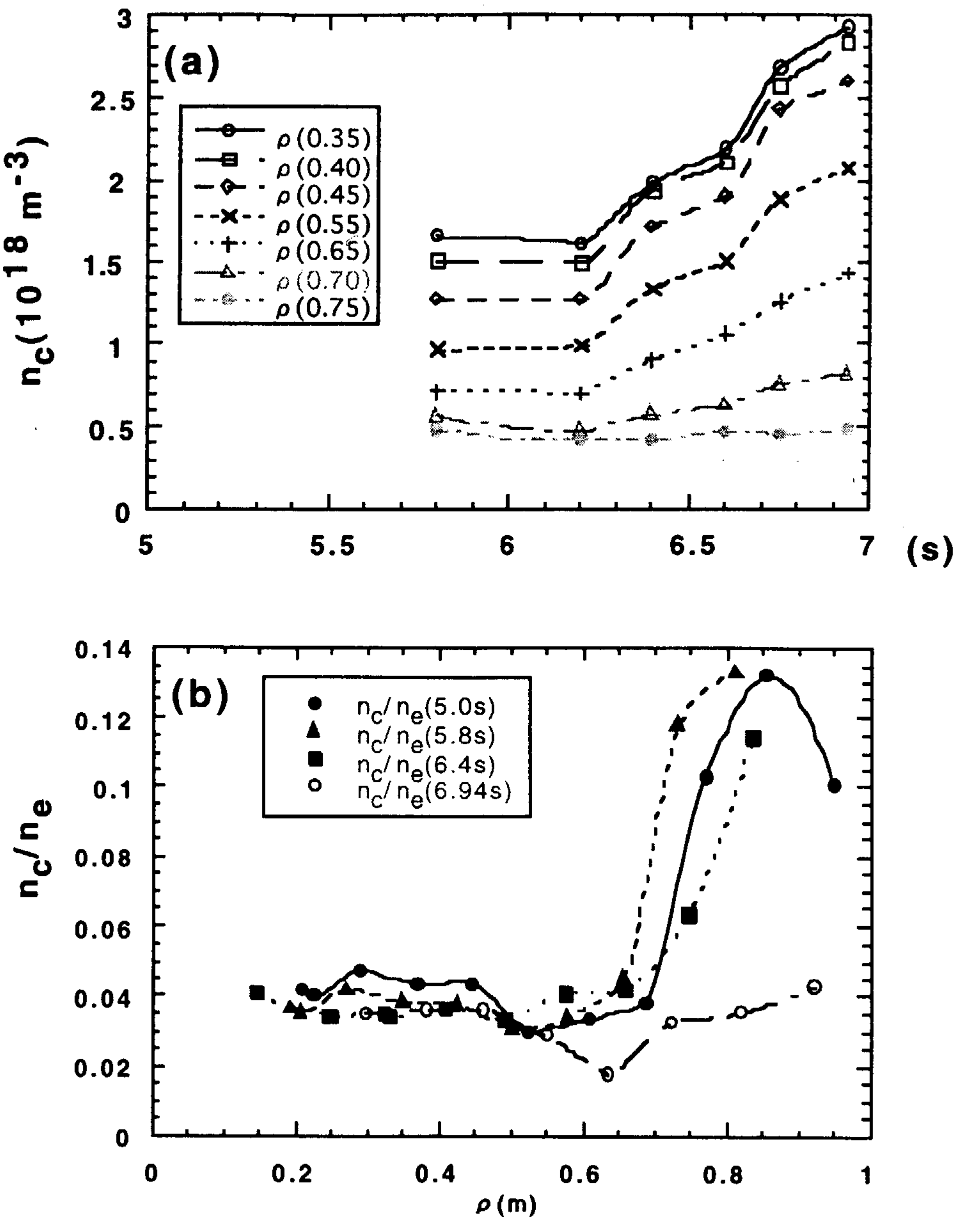

Figure 6-6: (a) Time evolution of carbon density (b)time evolution of n_C/n_e .

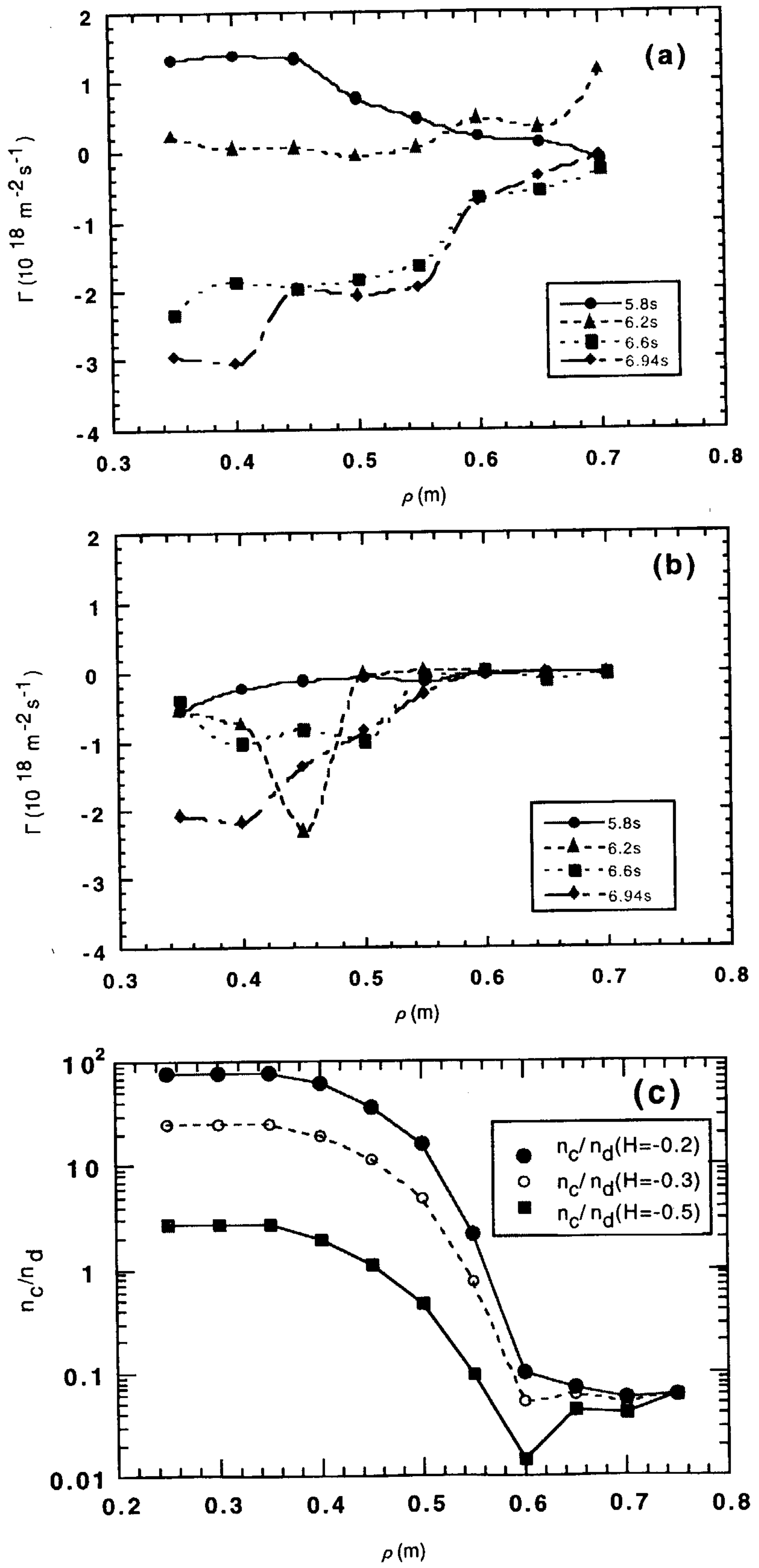

Figure 6-7:(a) Γ(carbon particle flux density) profile derived from the experimental results (b) time evolution of Γ profile derived from neoclassical theory (c) n_c/n_d carbon concentration based on neoclassical transport theory in the case of steady state.

国際単位系(SI)と換算表

表1　SI基本単位および補助単位

量	名　称	記　号
長さ	メートル	m
質量	キログラム	kg
時間	秒	s
電流	アンペア	A
熱力学温度	ケルビン	K
物質量	モル	mol
光度	カンデラ	cd
平面角	ラジアン	rad
立体角	ステラジアン	sr

表3　固有の名称をもつSI組立単位

量	名　称	記号	他のSI単位による表現
周波数	ヘルツ	Hz	$\mathrm{s^{-1}}$
力	ニュートン	N	$\mathrm{m{\cdot}kg/s^2}$
圧力，応力	パスカル	Pa	$\mathrm{N/m^2}$
エネルギー，仕事，熱量	ジュール	J	N·m
工率，放射束	ワット	W	J/s
電気量，電荷	クーロン	C	A·s
電位，電圧，起電力	ボルト	V	W/A
静電容量	ファラド	F	C/V
電気抵抗	オーム	Ω	V/A
コンダクタンス	ジーメンス	S	A/V
磁束	ウェーバ	Wb	V·s
磁束密度	テスラ	T	$\mathrm{Wb/m^2}$
インダクタンス	ヘンリー	H	Wb/A
セルシウス温度	セルシウス度	℃	
光束	ルーメン	lm	cd·sr
照度	ルクス	lx	$\mathrm{lm/m^2}$
放射能	ベクレル	Bq	$\mathrm{s^{-1}}$
吸収線量	グレイ	Gy	J/kg
線量当量	シーベルト	Sv	J/kg

表2　SIと併用される単位

名　称	記　号
分，時，日	min，h，d
度，分，秒	°，′，″
リットル	l，L
トン	t
電子ボルト	eV
原子質量単位	u

$1\ \mathrm{eV} = 1.60218 \times 10^{-19}\ \mathrm{J}$

$1\ \mathrm{u} = 1.66054 \times 10^{-27}\ \mathrm{kg}$

表4　SIと共に暫定的に維持される単位

名　称	記　号
オングストローム	Å
バーン	b
バール	bar
ガル	Gal
キュリー	Ci
レントゲン	R
ラド	rad
レム	rem

$1\ \text{Å} = 0.1\ \mathrm{nm} = 10^{-10}\ \mathrm{m}$

$1\ \mathrm{b} = 100\ \mathrm{fm^2} = 10^{-28}\ \mathrm{m^2}$

$1\ \mathrm{bar} = 0.1\ \mathrm{MPa} = 10^5\ \mathrm{Pa}$

$1\ \mathrm{Gal} = 1\ \mathrm{cm/s^2} = 10^{-2}\ \mathrm{m/s^2}$

$1\ \mathrm{Ci} = 3.7 \times 10^{10}\ \mathrm{Bq}$

$1\ \mathrm{R} = 2.58 \times 10^{-4}\ \mathrm{C/kg}$

$1\ \mathrm{rad} = 1\ \mathrm{cGy} = 10^{-2}\ \mathrm{Gy}$

$1\ \mathrm{rem} = 1\ \mathrm{cSv} = 10^{-2}\ \mathrm{Sv}$

表5　SI接頭語

倍数	接頭語	記　号
10^{18}	エクサ	E
10^{15}	ペタ	P
10^{12}	テラ	T
10^{9}	ギガ	G
10^{6}	メガ	M
10^{3}	キロ	k
10^{2}	ヘクト	h
10^{1}	デカ	da
10^{-1}	デシ	d
10^{-2}	センチ	c
10^{-3}	ミリ	m
10^{-6}	マイクロ	μ
10^{-9}	ナノ	n
10^{-12}	ピコ	p
10^{-15}	フェムト	f
10^{-18}	アト	a

（注）

1. 表1－5は「国際単位系」第5版，国際度量衡局 1985年刊行による。ただし，1 eVおよび1 uの値はCODATAの1986年推奨値によった。
2. 表4には海里，ノット，アール，ヘクタールも含まれているが日常の単位なのでここでは省略した。
3. barは，JISでは流体の圧力を表わす場合に限り表2のカテゴリーに分類されている。
4. EC閣僚理事会指令ではbar，barnおよび「血圧の単位」mmHgを表2のカテゴリーに入れている。

換　算　表

力	N(=10^5dyn)	kgf	lbf
	1	0.101972	0.224809
	9.80665	1	2.20462
	4.44822	0.453592	1

粘　度　$1\ \mathrm{Pa{\cdot}s(N{\cdot}s/m^2)} = 10\ \mathrm{P}$(ポアズ)$(\mathrm{g/(cm{\cdot}s)})$

動粘度　$1\ \mathrm{m^2/s} = 10^4\ \mathrm{St}$(ストークス)$(\mathrm{cm^2/s})$

圧力	MPa(=10 bar)	kgf/cm²	atm	mmHg(Torr)	lbf/in²(psi)
	1	10.1972	9.86923	7.50062×10^3	145.038
	0.0980665	1	0.967841	735.559	14.2233
	0.101325	1.03323	1	760	14.6959
	1.33322×10^{-4}	1.35951×10^{-3}	1.31579×10^{-3}	1	1.93368×10^{-2}
	6.89476×10^{-3}	7.03070×10^{-2}	6.80460×10^{-2}	51.7149	1

エネルギー・仕事・熱量	J(=10^7 erg)	kgf·m	kW·h	cal(計量法)	Btu	ft·lbf	eV
	1	0.101972	2.77778×10^{-7}	0.238889	9.47813×10^{-4}	0.737562	6.24150×10^{18}
	9.80665	1	2.72407×10^{-6}	2.34270	9.29487×10^{-3}	7.23301	6.12082×10^{19}
	3.6×10^6	3.67098×10^5	1	8.59999×10^5	3412.13	2.65522×10^6	2.24694×10^{25}
	4.18605	0.426858	1.16279×10^{-6}	1	3.96759×10^{-3}	3.08747	2.61272×10^{19}
	1055.06	107.586	2.93072×10^{-4}	252.042	1	778.172	6.58515×10^{21}
	1.35582	0.138255	3.76616×10^{-7}	0.323890	1.28506×10^{-3}	1	8.46233×10^{18}
	1.60218×10^{-19}	1.63377×10^{-20}	4.45050×10^{-26}	3.82743×10^{-20}	1.51857×10^{-22}	1.18171×10^{-19}	1

1 cal = 4.18605 J（計量法）

　= 4.184 J　（熱化学）

　= 4.1855 J　(15 ℃)

　= 4.1868 J（国際蒸気表）

仕事率　1 PS（仏馬力）

　= 75 kgf·m/s

　= 735.499 W

放射能	Bq	Ci
	1	2.70270×10^{-11}
	3.7×10^{10}	1

吸収線量	Gy	rad
	1	100
	0.01	1

照射線量	C/kg	R
	1	3876
	2.58×10^{-4}	1

線量当量	Sv	rem
	1	100
	0.01	1

（86年12月26日現在）

STUDY ON IMPURITY RADIATION AND TRANSPORT OF JT-60U PLASMAS